EFFECT OF MONOTONIC AND CYCLIC LOADING ON THE FRACTURE BEHAVIOUR OF SA 333 STEEL

PRABHA PRASAD

EFFECT OF MONOTONIC AND CYCLIC LOADING ON THE FRACTURE BEHAVIOUR OF SA 333 STEEL

Thesis Submitted in Partial Fulfilment
of the Requirements for the Degree of

Doctor of Philosophy
in
ENGINEERING

by
PRABHA PRASAD

at the

DEPARTMENT OF METALLURGICAL AND MATERIALS ENGINEERING
INDIAN INSTITUTE OF TECHNOLOGY
KHARAGPUR-721 302, INDIA
2002

CERTIFICATE

This is to certify that the thesis entitled **"EFFECT OF MONOTONIC AND CYCLIC LOADING ON THE FRACTURE BEHAVIOUR OF SA 333 STEEL"** being submitted by ***Mrs. PRABHA PRASAD*** to the Indian Institute of Technology, Kharagpur, for the award of the degree of **DOCTOR OF PHILOSOPHY** in **ENGINEERING** is a record of bonafide research work carried out under our supervision. The results presented in this thesis have not been submitted elsewhere for the award of any other degree.

This work, in our opinion, has reached the standard fulfilling the requirements for the award of the degree of **DOCTOR OF PHILOSOPHY** in accordance with the regulations of the institute.

Professor
Department of Metallurgical
and Materials Engineering,
Indian Institute of Technology,
Kharagpur-721302.

(Prof. K.K.Ray)

Sr. Dy Director, Head
Materials Evaluation Division,
National Metallurgical Laboratory,
Jamshedpur - 831007.

(Dr. R. Singh)

ACKNOWLEDGMENT

I express my deep sense of gratitude to Prof. K. K. Ray, Department of Metallurgical and Materials Engineering, Indian Institute of Technology, Kharagpur, for his invaluable guidance, constant encouragement and critical discussions throughout this research program and during the preparation of this manuscript. His inspiration at every stage of this work is duly appreciated. It is my proud privilege to be associated with him and worked under his guidance.

I take this opportunity to acknowledge with sincere gratefulness Dr. R. Singh, Sr.Dy.Director, Head, Materials Testing and Evaluation Division, National Metallurgical Laboratory, Jamshedpur for his initiative and inspiration and guidance to pursue this work.

I extend my gratitude and thanks to Dr. V. R. Ranganath, and Dr. S. Tarafder Asst.Director, Fatigue and Fracture Group, Materials Testing and Evaluation Division, National Metallurgical Laboratory, Jamshedpur, in carrying out round the cloak experiments, data analysis and their invaluable suggestions during technical discussions, sustained interest, moral support and encouragement without which it was impossible to carry out this investigation.

I thank Mr.H.S.Kushwaha Head Reactor Safety Division and Mr.P.K.Singh Scientific officer BARC for providing material for the investigation.

I am grateful to Prof. P. Ramachandra Rao, former Director and Dr.S.P. Mehrotra present Director National Metallurgical Laboratory, Jamshedpur, for their advice and support in providing the necessary facilities to carry out this work successfully.

The encouragements and advices received from Prof. M.Chakraborty, Prof. U.K.Chatterjee, Prof. A.K.Chakraborty, Prof.S.K.Ray Prof. B. Pradhan and other faculty members and the contemporary research scholars of the Metallurgical and Materials Engineering Department of Indian Institute of Technology, Kharagpur during the entire period of this research work is gratefully acknowledged. Thanks are also due to the other staffs of the department for all their help and cooperation. The friendly assistance rendered by Mr. Narsiesh and Mr. Sashidhar Kudari during the preparation of the thesis will be cherished forever.

It is my privilege to thank Dr. R. N. Ghosh, Head, Computer Application Division and Dr.D.K.Bhattacharya Head, Materials Characterization Division of the National Metallurgical Laboratory, for his relevant suggestions during discussion, for providing necessary facilities and personal support in various ways.

A special word of thanks is due to Mr. Swapan Das of National Metallurgical Laboratory for his constant help in electron microscopic facilities. Much of the fractographic (SEM) work would have been incomplete without his personal help. His timely suggestions and help are highly appreciated. I am thankful to Mrs. Mita Tarafder, Scientist, National Metallurgical Laboratory for her help during this work.

My sincere thanks are due to my friends and fellow colleagues of Materials Evaluation Division of the laboratory, Mr. A. Seshukumar, Dr.S.Shivaprasad, Dr. J.Swaminathan and many others who assisted me at all moments of need. My thanks are also due to Mr. B. Goswami, ex-project assistant, for helping me in metallographic studies, staff of NML workshop.

I express my profound gratitude to my father, who inspired me of doing this work in my childhood by becoming my role model. This work is a tribute to my mother Mrs. (Late) Usha Prasad, who made all sacrifices to make my dream reality. I thank my brothers and sisters and my mother-in-law for their constant support, understanding and the encouragement extended during this work.

Finally, I express my heartfelt deep gratitude to my husband Mr. Karunesh Johri, for his love, patience, sacrifices, encouragements and moral support without which this my childhood dream would not have become true.

Kharagpur
December 2002 (**PRABHA PRASAD**)

Preface

This dissertation is submitted for the degree of Doctor of Philosophy at the Indian Institute of Technology, Kharagpur, India. This investigation has been carried out in the Department of Metallurgical and Materials Engineering, Indian Institute of Technology, Kharagpur and at the Materials Evaluation Division (MTE), of National Metallurgical Laboratory, Jamshedpur, from January 1995 to Sept 2002. Except where acknowledgment to previous work is made, this dissertation is my own work assisted and guided by my supervisors at all stages, and no part of this work belongs to any other collaborative project.

This dissertation is divided into six chapters. Chapter-1. addresses the significance of the study of monotonic and cyclic fracture resistance of SA333 Gr 6 steel, which is used in the fabrication of the primary heat transfer pipes in nuclear power plants. Some fundamental principles of fracture mechanics and its application in structural integrity assessment of the critical components, with emphasis on concepts related to cyclic *J–R* curves, and the scope of the investigation has been appraised in Chapter-2. The characteristics of the selected steel and its related mechanical properties including its dynamic strain ageing behavior at elevated temperatures have been described in Chapter-3. Chapter-4 examines the monotonic fracture toughness behaviour of the material at ambient and elevated temperatures. The effect of cyclic loading on the fracture resistance behaviour of the steel is discussed in Chapter-5. Each of the Chapters 3-5 includes the objective at the outset, followed by details of the experimental work, the results obtained and their pertinent discussion prior to the conclusions drawn. Chapter-6 gives an overall view of the major conclusions drawn from this investigation and suggests the future work in this field.

Prabha Prasad

RÉSUMÉ

The author was born on 1st Sept., 1960 at village Gaddopur, in Samastipur district of Bihar. She acquired first class in M.Sc. (Chemistry) from Ranchi University, Ranchi, Jharkhand, in the year 1991. She later joined Regional Institute of Technology, Jamshedpur and obtained her Master of Technology degree in Corrosion and Science of Surface Coating in the year 1993 on GATE fellowship. In Dec 1993, she was awarded Senior Research Fellowship and joined the Materials Evaluation Division of National Metallurgical Laboratory, Jamshedpur. In Sept. 1998, she joined as Scientist in the Materials Evaluation Division of the same laboratory and is still continuing the same position. She has participated in several sponsored projects related to remaining life assessment and failure analysis of industrial components This has given her an opportunity to acquire experience in the field of creep, fatigue and fracture of behaviour of materials. The curiosity of the author for research made her to join the Department of Metallurgical and Materials Engineering, Indian Institute of Technology, Kharagpur in 1995 as a sponsored research scholar to pursue her doctoral degree.

Present Address

C/o Dr.D. Prasad
H.No. 53 Gandhi road
Old Sonari
Jamshedpur,
Jharkhand – 831 011
Ph.No-0657-2222079

Permanent Address

C/o Mr.K.Johri
A 310-A Surya Nagar,
Ghaziabad
U.P- 201 011
Ph.No-0120-2622231

List of Symbols

Symbol	Description
a_N	Crack length up to machine notch
a	Crack length,
a_O	Crack length after pre-cracking
B	Specimen thickness
B_{net}	Net Specimen thickness
B_{eff}	Effective specimen thickness
b	Remaining ligament after cracking
C	Paris Constant
C_1, C_2	Constant in *J*-crack extension relation
E, E'	Youngs modulus, effective Young's modulus
e_u	Percentage uniform elongation
e_t	Percentage total elongation
J	*J*-integral
J_{Ic}, J_c	Critical *J*-integral strain energy release rate
J_e, J_{pl}	Elastic and Plastic components of *J*
J_{cyc}	Cyclic *J*-integral
ΔJ_D	Dowling's operational *J*
J_i.	Fracture initiation toughness
$J_{0.2}$	Vertical intercept fracture toughness at 0.2mm crack extension
ΔJ,	Instantaneous, initial, effective values of stress intensity factor ranges in terms of *J*
k_ε	Hall-Petch slope
K, K_C, K_{Ic}	Stress intensity factor (SIF), Critical value of *K*, Plane strain fracture toughness
K_{max}	Maximum value of stress intensity factor
m	Exponent of the Paris equation
m	Constant in *J*-crack extension relation
N	Number of cycles in fatigue test
n	Strain hardening exponent
P	Load
P_{max}	Maximum load
r_p	Plastic zone size
R	Load ratio in fatigue test.

T_J, T_δ	J and CTOD tearing modulus
W	Strain energy
V	Load line displacement
V_p	Plastic component of clip gauge displacement
W	Specimen width
γ_S	Surface energy
γ	Strain rate sensitivity
γ_{eff}	Effective surface energy for cleavage crack propagation
J_R, δ_R	Resistance curves represented by J vs $\Delta\alpha$ or CTOD vs $\Delta\alpha$
δ	Crack opening displacement
$\partial G/\partial a$	Rate of change of elastic energy release rate
ΔK, ΔK_o, ΔK_{eff}	Instantaneous, initial, effective values of stress intensity factor ranges
Δa	Crack extension
ν	Poisson's ratio
σ_o	Flow stress
σ_{ys}	Yield strength
σ_{UTS}	Ultimate tensile strength
da/dN	Fatigue crack growth rate per cycle

List of Abbreviations

Abbreviation	Description
ASM	American society of metals
ASME	American society for mechanical engineers
ASTM	American society for testing materials
CCL	Compliance crack length
CL	Transverse - longitudinal direction
CMOD	Crack mouth opening displacement
COD	Crack opening displacement
CT	Compact tension specimen
CTOD	Crack tip opening displacement
CVN	Charpy V-notched impact energy
DCPD	Direct current potential difference
DSA	Dynamic strain aging
FCGR	Fatigue crack growth rate
FT	Fracture toughness
HCF	High cycle fatigue
JIS	Japanese Industrial Standard
LBB	Leak before break
LC	Longitudinal-transverse direction
LCF	Low cycle fatigue
LEFM	Linear elastic fracture mechanics
LLD	Load line displacement
MVC	Micro-void coalescence
PHT	Primary Heat Transport pipings
PHWR	Pressurized Heavy Water Reactors
RA	Percentage reduction in area
SEM	Scanning electron microscope
SAE	Society of Automotive Engineers
SZW	Stretch zone width
UTS	Ultimate tensile strength
YS	Yield strength

Abstract

The fracture resistance behaviour of SA 333 Gr 6 steel has been studied, as a part of the assessment of the structural integrity of the primary heat transfer piping of nuclear power plants. The microstructure of the steel and its relevant mechanical properties such as hardness, tensile and impact properties have been characterized. A series of tensile tests and a few strain rate change tests have been carried in the temperature range of 28^{o} to 300^{o}C. Monotonic *J-R* curves of the material have been determined in the temperature range of 28-300^{o}C, whereas cyclic crack growth resistance curves have been determined at the stress ratios of R = 0, -0.5, -0.8, -1.0 and –1.2, and for three plastic displacement levels 0.5, 0.3 and 0.15mm at the ambient temperature. Fractographic studies and examinations of crack tip profiles of specimens interrupted during monotonic and cyclic *J* tests have been carried out

Microstructural characterization of the steel revealed banded ferrite-pearlite structure along both the longitudinal and transverse directions with high degree of cleanliness. The material exhibited dynamic strain ageing behaviour in the strain rate range 1.2×10^{-3} to $1.2 \times 10^{-5} s^{-1}$ and in the temperature range 200^{o} to 300^{o}C. The occurrence of dynamic strain ageing in the material between 200-300^{o}C has been confirmed by strain rate change test. The results of fracture studies under monotonic loading infer: (a) the material exhibits high fracture resistance at room temperature; this has been attributed to its high degree of cleanliness, (b) the fracture resistance of the steel deteriorates in the temperature range 200-250^{o}C; the deterioration in the fracture properties has been attributed to dynamic strain ageing behaviour operative in this temperature range, (c) the fracture initiation toughness and the crack propagation resistance are inferior along CL plane in comparison to LC plane; this has been attributed to the presence of elongated inclusions in CL crack plane and (d) the stretch zone in the investigated steel is of unconventional type and is intermixed with ductile tearing.

The results and their analysis of the cyclic fracture behaviour of the steel lead to the following conclusions (a) cyclic *J-R* curves are similar for positive stress ratio, (b) The cyclic *J-R* curves, the fracture initiation toughness and the resistance to crack propagation of the steel were found to degrade with (i) decrease in stress ratio from 0 to -1.0 and /or (ii) decrease in plastic displacement associated with these tests. The degradation in the fracture initiation toughness and the resistance to crack propagation of the steel for $R < 0$ occurs due to re-sharpening of the crack tip during compressive loading. The fractographic studies and examination of crack tip profiles have revealed that the crack propagation mechanism in monotonic and cyclic loading is different. An empirical relation has been proposed to estimate cyclic fracture toughness from its monotonic fracture toughness.

CONTENTS

Subject		Page No.

Subject	Page No.

1.0 INTRODUCTION

The SA 333 Grade 6 steel of current interest is used in primary heat transport (PHT) piping systems of pressurized heavy water reactors (PHWR). The operating temperature range of this structural component is 28-300^{o}C. The primary heat transport piping and pressure vessels of nuclear power plants are designed and operated on the basis of leak before break (LBB) concept. In order to implement this LBB concept in the design of PHT piping, it is important to understand the fracture toughness behaviour of the material in its operating conditions.

The SA 333 Gr 6 is plain carbon steel having carbon content of up to 0.3 wt%. It is well documented in the literature that plain carbon steels exhibit dynamic strain aging (DSA) behaviour in the temperature range of 150-450^{o}C [1-3]. Since the service temperature of PHT piping is 28-300^{o}C, it is important to understand dynamic strain aging behaviour in the steel in this temperature range. The occurrence of DSA degrades ductility and fracture resistance behaviour of steels [2-7]. Based on some observed degradation of fracture resistance of SA 333 variety steel at elevated temperature, an earlier report indicated the presence of DSA in this steel without any detailed investigation [5]. One of the major objectives in this investigation thus is to understand DSA in this steel prior to studies related to fracture behaviour of the material.

The pipes used in PHT system possess an outer diameter of the order of 406mm with a wall thickness of 32mm. So any attempt to probe fracture toughness of the material from specimens cut from this component is limited by curved sections of 32mm thickness. This specimen thickness limitation permits one to carry out only assessment of elastic-plastic fracture toughness of the steel. The *J*-integral fracture toughness of a few steels having similar composition are reported in the literature [3-7] but such toughness indices of the selected steel at ambient and at elevated temperature are not available. Hence an investigation on the *J*-integral fracture behaviour of the steel was directed to understand the effect of DSA on the crack growth resistance behaviour of the steel.

One of the current design considerations in nuclear power plants, is to safe-guard all structural components against seismic (cyclic) loading. Some recent reports

have shown that fracture toughness of structural materials is inferior in cyclic loading condition in comparison to monotonic loading [8-11]. Since seismic loading may induce cyclic loading in a component, it is necessary to understand the fracture behaviour of the selected steel under cyclic loading condition also.

In summary, the objectives of this investigation encompass studies on microstructural aspects, related mechanical properties, dynamic strain aging characteristics, monotonic and cyclic fracture behaviour of SA 333 Gr 6 steel.

2.0 OBJECTIVES

The major objectives and the pertinent work-plan to fulfil these are categorized into three broad modules. These are:

(I) To characterise the microstructure and to determine the related mechanical properties of the selected steel with an emphasis to examine dynamic strain ageing behaviour at elevated temperatures.

Module I: This module consists of (a) characterisation of the inclusions in SA 333 steel, (b) determination of the amount and distribution of the various phases in the microstructure, (c) measurement of ferrite grain size, (d) determination of hardness and Charpy impact energy, (e) evaluation of tensile properties of the steel at ambient and at elevated temperatures at various strain rates and (f) examination of the tensile behaviour of the material during strain rate changes.

(II) To study the monotonic fracture behaviour of the steel at ambient and at elevated temperatures.

Module II: This module comprises of (a) generation of monotonic *J-R* curves of the steel at ambient and at temperatures in the range of 200 to 300^{o}C, and (b) examination of the effect of crack plane orientation, test temperature and DSA on the fracture toughness behaviour of the material.

(III) To study the cyclic fracture behaviour of the steel at ambient temperature.

Module III: This module consists of (a) generation of a series of cyclic *J-R* curves of the steel at different test conditions, (b) investigation of the effect of stress ratio and plastic displacement on the *J-R* curve, (c) attempts to correlate the cyclic and

monotonic fracture initiation toughness of the material, and (d) examination of the micro mechanisms of crack propagation in the steel during various types of loading.

In attempting to meet the above objectives, where ever possible standard test were carried out. But neither any standard nor any recommended practice is available for cyclic *J*-test. These tests have been designed and performed following a few earlier investigations. Attempts have been made to assign reasons and explanations for the observed results and to illustrate the practical utility of the generated data. The thesis has been structured into chapters, one for each of the major objectives listed above. A literature background related to the current investigation has been presented as a chapter prior to the obtained results and their discussion. An overview of the conclusions derived from this work has been summarized as a brief chapter together with some proposed future work related to this area. All references quoted throughout the dissertation have been compiled at the end.

2.0 LITERATURE REVIEW

2.1. INTRODUCTION

This chapter deals with the terminologies of linear elastic and elastic-plastic fracture mechanics in section 2.2. Various fracture mechanics parameters such as stress intensity factor (K), crack tip opening displacement ($CTOD$), J integral, R resistance curve and tearing modulus T_J have been defined and explained in brief. The engineering need and the concepts behind development of cyclic J-R curves are discussed in section 2.3. This section incorporates a review of available reports on cyclic J-R curves under various types of loading. Some information related to the phenomenon of dynamic strain aging with reference to steels used in pipings and pressure vessels are incorporated in section 2.4 illustrating the effect of dynamic strain aging on tensile and fracture toughness properties of steels. The significance of low carbon steels used in nuclear power plants is discussed in section 2.5. Finally a basis for the present investigation is provided in section 2.6.

2.2. FRACTURE MECHANICS AND ITS TERMINOLOGIES

Fracture mechanics encompasses stress analysis ahead of cracks, experiments and observations to suggest useful representation of forces that cause the development and extension of cracks. The crack extension behaviour is governed by the stress field distribution ahead of a crack tip as suggested by Irwin [12]. The material, in which crack propagation is accompanied by very small or insignificant deformation, predominantly behaves in linear elastic manner. Such materials come under the purview of Linear Elastic Fracture Mechanics (LEFM). On the other hand, if the crack propagation is accompanied by large plastic deformation, Elastic Plastic Fracture Mechanics (EPFM) approach is adopted to describe the crack driving forces ahead of a crack tip in the material.

2.2.1. LEFM *vis*-à-*vis* EPFM

The principle of linear elastic fracture mechanics (LEFM) is based on the unique distribution of stress ahead of a crack in a body under load. The amplitude of such a distribution is characterized by the stress intensity factor K, a critical value of

which provides the driving force for existing cracks to propagate. The solution of the stress field ahead of a crack using linear elasticity can be given as:

$$\sigma_{ij} = \frac{K}{(\sqrt{2\pi r})} f_{ij}(\theta) \tag{2.1}$$

where, (r,θ) represent polar co-ordinates around the crack tip and $f_{ij}(\theta)$ are characteristic functions. The elastic stress field solution indicates the presence of a stress singularity at the tip of a crack. However in practice, most materials exhibit a yield stress above which they deform plastically. As a result there exists a region around the crack tip, which is plastically yielded. This region is called the plastic zone (PZ). The plastic zone size for a material with yield strength σ_{ys} is given as:

$$r_\rho = \frac{1}{n\pi}\left(\frac{K_I}{\sigma_{ys}}\right)^2 \tag{2.2}$$

where the magnitude of n depends on the state of stress.

The employment of LEFM remains valid as long as the size of PZ is insignificantly small in comparison to significant dimensions of the cracked geometry. In materials where the size of the PZ is large, fracture conditions are controlled by elastic-plastic fracture mechanics (EPFM). EPFM often uses the concept of non-linear elasticity to obtain solutions for equivalent plastic problems. Unlike LEFM, EPFM demands a careful understanding of the crack tip plasticity and currently this discipline provides a few established procedures for obtaining fracture criteria. These are: (i)crack tip opening displacement (*CTOD*), (ii) *J*-integral, (iii) *R* curve and (iv)Tearing Modulus T_J

2.2.2. *CTOD* Parameter

Wells [13,14] proposed that the failure of a cracked component can be characterised by the opening of the crack faces in the vicinity of a sharp crack tip known as crack opening displacement (*COD*). He showed that the concept of crack opening displacement was analogous to concept of critical crack extension force and thus the *COD* values could be related to the plane-strain fracture toughness, K_{IC}. Because *COD* measurements can be made even when there is considerable plastic flow ahead of a crack, such as would be expected for elastic-plastic or fully plastic behaviour, the technique may be used to establish critical design stresses or crack sizes in a quantitative manner similar to that of linear-elastic fracture mechanics.

Dugdale's strip yield model analysis [15] relates *COD* to the applied stress and the crack length as given below

$$\delta = \frac{8\sigma_{ys}a}{\pi E}\left[\ln\left(\sec\frac{\pi a}{2\sigma_{ys}}\right)\right] \tag{2.3}$$

where,

δ = crack tip opening displacement

σ_{ys} = yield stress, a = crack length,

σ = the applied stress and E = the elastic modulus

At $\sigma/\sigma_{ys} \ll 1$, at the crack instability the above expression can reduce to

$$\delta_{IC} = \frac{K^2_{IC}(1-\nu^2)}{\lambda E \sigma_{ys}} \tag{2.4}$$

2.2.3. *J* Integral Parameter

The path independent *J*-integral proposed by Rice [16] can be used to characterize the stress-strain fields at the tip of a crack and to analyse the fracture process in elastic-plastic materials. *J* can be computed by an integration path taken sufficiently far from the crack tip to be substituted for a path close to the crack tip region. Thus, even though considerable yielding occurs in the vicinity of a crack tip, the behaviour of the crack can be inferred by considering a region away from the crack tip for the analysis. This technique can be used to estimate the fracture characteristics of materials exhibiting elastic-plastic behaviour. For linear elastic behaviour, the *J* integral is identical to *G*, the energy release rate per unit crack extension. Therefore *J* failure criterion for the linear-elastic case is identical to the K_{IC} failure criterion. For linear elastic plain-strain conditions,

$$J_{Ic} = G_{Ic} = \frac{(1-\nu^2)}{E} K_{Ic}^{\ 2} \tag{2.5}$$

The energy line integral, *J* is defined for either elastic or elastic-plastic behaviour as follows

$$J = \int_{\Gamma}\left(Wdy - T_i\frac{\partial u_i}{\partial x}ds\right) \tag{2.6}$$

where, $W = \int_0^{\varepsilon} \sigma_{ij} d\varepsilon_{ij}$ = strain energy density, (2.7)

$T_i = \sigma_{ij} n_j$ = vector of surface tractions,

u_i = displacement vector,

s = element of arc length along contour Γ.

For any linear elastic or elastic plastic material treated by deformation theory of plasticity, Rice [16] had shown path independence of the J integral parameter. The J integral can be interpreted as the potential energy difference between two identically loaded specimens having slightly different crack lengths i.e., a and a+da. The energy parameter J is given as,

$$J = -\frac{1}{B}\frac{\partial u}{\partial a} \tag{2.8}$$

This definition is shown schematically in Fig.2.1 where the shaded area is $\partial u = JB\partial a$. Begley and Landes [17] developed compliance technique for evaluating J-integral, which made this fracture mechanics parameter more popular in comparison to other fracture mechanics parameters. Standard test procedure for determining the fracture toughness of the ductile materials in terms of J integral has been developed and incorporated in ASTM standard E-1820 [18]. Generally three point bend or compact tension specimens are used for J integral testing of the materials.

2.2.4. Crack Growth Resistance Curve (*R* curve)

For thin sheets resistance to crack growth R increases as the crack grows from its initial length as shown in the Fig.2.2. In this case instability occurs when a line of G_1 at constant load becomes tangent to the R-curve, i.e.

$$G_1 = R$$

and

$$\frac{\partial G_1}{\partial a} = \frac{\partial R}{\partial a} \tag{2.9}$$

The idea of a crack growth resistance or R-curve was first suggested by Krafft et al. [19]. These investigators postulated that the crack resistance curve should have a unique shape for each material independent of initial crack length, specimen geometry and boundary loading conditions. This concept is expressed in terms of stress intensity factor, K_C and K_R as given in Fig.2.3. The critical stress intensity factor, K_C, is that at which tangency between K_R and K_C occurs. In making the estimate of K_C, R curves are regarded as though they are independent of the initial crack length a_i and the specimen

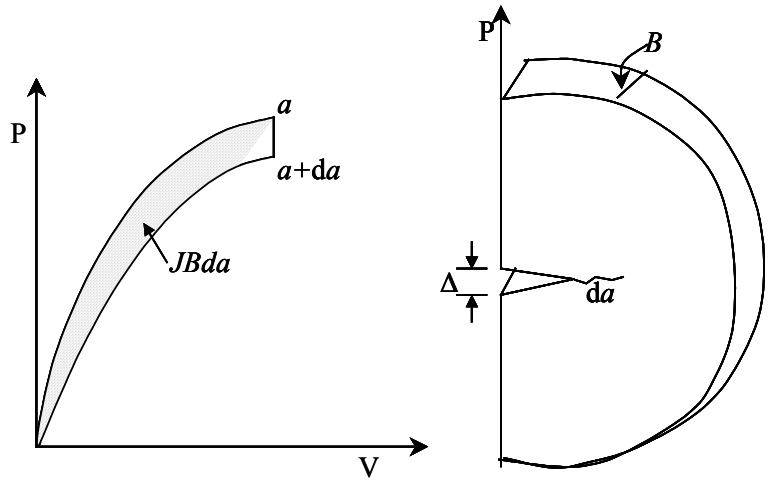

Fig.2.1. Interpretation of *J*-integral.

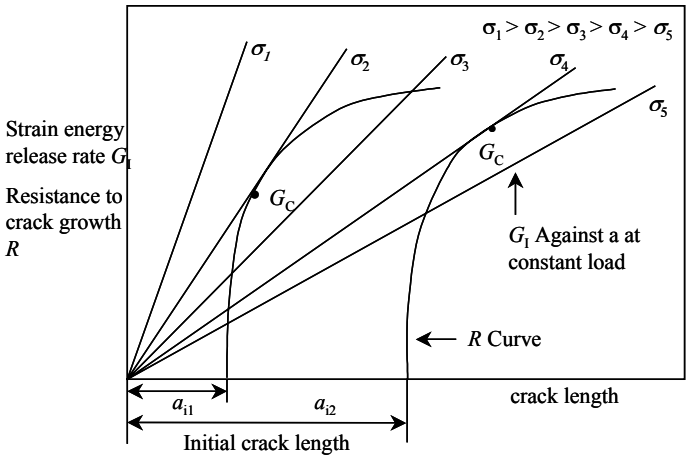

Fig.2.2 *R*-curves in terms of *G* for a specimen containing initial crack a_{i1} and a_{i2}

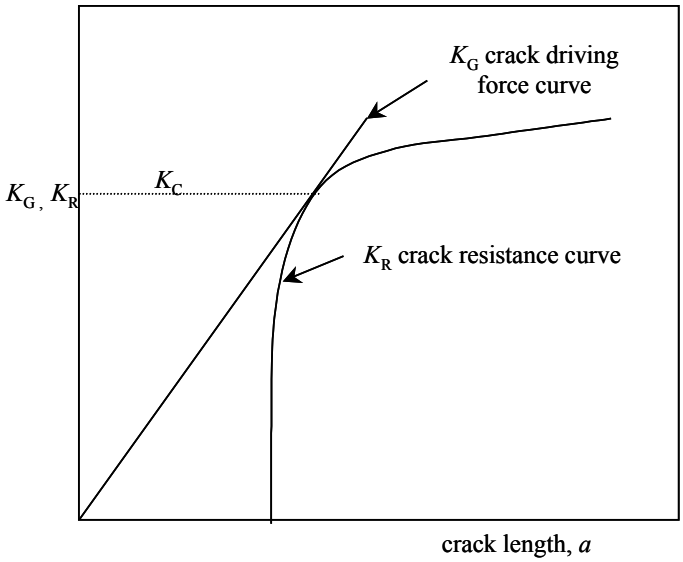

Fig.2.3 *R*-curve in terms of stress intensity factor.

geometry. The concept of the resistance curve is now well accepted. The standard methods of determining *R*-curves have been documented in ASTM standard E-561 [20].

2.2.5. Tearing Modulus

Materials having good ductility show appreciable plasticity at fracture and usually undergo slow and stable crack growth before fracturing. Thus the crack will start growing at a critical value, J_{IC}/J_C, and hence it is useful in quantifying the onset of fracture. But further increase of stress is required to sustain the crack growth. Apparently the crack resistance increases with crack growth, which is reflected in a higher value of *J* integral. The crack resistance curve is called as *R* curve, J_R curve or *J-R* curve. Thus the criteria for stable crack growth can be written as

$$J = J_{\mathrm{R}} \tag{2.10}$$

fracture instability will occur when

$$J \geq J_R \tag{2.11}$$

on differentiation

$$\frac{\mathrm{d}J}{\mathrm{d}a} \geq \frac{\mathrm{d}J_{\mathrm{R}}}{\mathrm{d}a} \tag{2.12}$$

In high toughness materials crack initiation is not the only relevance but propagation stage is also important, and it will have considerable lifetime left after the crack initiation. Therefore greater attention is now being focused on the investigation of both crack initiation and propagation behaviour of the materials. This has prompted several investigators to study the stability of crack growth based on the concept of *J* integral resistance curves.

Paris et al. [21] have proposed a dimensionless form for the crack growth resistance parameter. It has been denoted by T_{J} and is called as tearing modulus.

$$T_{\mathrm{J}} = \frac{E}{\sigma_{\mathrm{o}}{}^2} \frac{\mathrm{d}J}{\mathrm{d}a} \tag{2.13}$$

where,

E = elastic modulus of the material

σ_{o} = flow stress of the material

This parameter offers a convenient definition for crack growth toughness based on the *J* integral approach. Here d*J*/d*a* is the slope of *J*-Δ*a* resistance curve in the stable crack growth region.

Thus the applied instability criterion is:

$$T_{\text{applied}} > T_{\text{Jmaterial}}$$

Hutchinsion and Paris [22] suggested that the assumption of *J* controlled crack growth is valid when the following conditions are fulfilled

$$\omega = \frac{b}{J}\cdot\frac{\mathrm{d}J}{\mathrm{d}a} >> 1 \qquad (2.14)$$

and $a < 0.06b$

for CT specimens, the value of ω may not be less than 10 [22]. In the case of ductile materials, the fracture may be characterized by a critical crack opening displacement δ_c [23] Analogous to *J-R* curves, δ-R curves may also be constructed. The CTOD resistance is often expressed as crack tip opening angles CTOA [23].

2.3. CYCLIC *J-R* CURVE

Engineering components can be subjected to a wide variety of service loads and should be designed to operate safely under all such variations. The safety assessment for monotonic loading can be achieved using the concepts of K_{Ic}, J_{Ic}, or δ_c; under fatigue loading it can be achieved using Paris law [24]. This law is expressed as

$$\frac{\mathrm{d}a}{\mathrm{d}N} = \mathrm{C}(\Delta K)^m \qquad (2.15)$$

where,

$\frac{\mathrm{d}a}{\mathrm{d}N}$ = crack growth rate of material per cycle,

ΔK = applied elastic stress intensity range

C and *m* are material constants.

When an engineering component is subjected to monotonic loading with intermittent cycling neither the conventional monotonic fracture toughness values nor the Paris law constants are sufficient to predict its safe operating margins with reliability. This situation is not a mere hypothesis, but is documented by a Japanese group who recorded severe extent of load reversals on engineering components during a seismic

event [25]. This aspect has been of serious concern for several critical engineering components like that in nuclear power plants. As a consequence attempts are being made over the last two decades to understand cyclic *J-R* curves.

2.3.1 Cyclic *J-R* curves for $R \geq 0$

Reports on the determination of cyclic *J-R* curves of engineering materials may be divided broadly into two categories viz., tests conducted with a load ratio, $R \geq 0$ and $R < 0$. Important observations and conclusions from various reports are summarized in Table 2.1. Clark et al. [26] in their attempts to establish a single specimen partial unloading technique for fracture toughness determination, imposed partial unloadings upto 10% of maximum load on CT specimens. These partial elastic unloadings were used for calculating (intermittently) crack lengths and *J-R* curves, developed for CT specimens of thickness ranging from 0.5 to 5 inches. The *J-R* curves were observed to be identical for small crack extensions in all the specimen sizes. The slopes of *J-R* curves change for different specimen sizes at large crack extensions. It was concluded by these authors that the partial unloadings do not alter the *J-R*-curves of the material as long as the process zone to plastic zone size ratio remains within a limit. Similar findings were also reported by Joyce [27]. He confirmed that unloading up to 50% of P_{max} during *J-R* tests on specimens of 3% Ni structural steel has no effect on fracture initiation toughness of the material. However, unloading upto 100% of P_{max} lowers the fracture toughness of the same material. Several other investigators [28-31] support the observations that the difference between *J-R* curves obtained at $R = 0.5$ and $R = 0$ (unloading of 50 and 100% of P_{max} respectively) is insignificant.

Kaiser [28] investigated two steels, one pressure vessel steel and the other a quenched and tempered structural steel, of yield strength 375 and 750MPa respectively. The tests for crack growth resistance were carried out by Kaiser, in displacement control with constant increase in total displacement during each cycle. It was observed by the author that as the incremental displacement decreases, the slope of the *J-R* curve also decreases, and for the smallest displacement, the slope is minimum. For the large plastic displacements there were only 20 unloadings, whereas for smaller displacements there were more than 100 unloading cycles. The effect of cycling was very pronounced for small incremental displacement (0.74μm) and the slope of *J-R* curve was only 5% of that of the monotonic *J-R* curve. This implies that

Table 2.1 Summary of literature on the effect of cyclic loading on fracture resistance of materials.

Author	Material	Material Properties σ_{ys} σ_{uts} %El	Test parameters	Observations
Clarke [26]	3.6% Nickel Steel	607 -N.A.-	Displacement control, UL only upto 90% of P_{max}	No change in *J-R* curves for 30 cycles.
Joyce [29]	3% Nickel structural Steel	607 724 26%	Strain control UL of 50 and 100% ΔV 0.005 and 0.05	No change in J_{Ic} and *J-R* curve for ΔV 0.005mm and 50% unloading J_{Ic} changes and *J-R* curve reduces for 100% unloading *J*-R curve falls slightly above monotonic scatter band.
Kaiser [28]	High strength quenched & tempered structural steel	750 860 N.A	Displacement control R 0 With increase in ΔV in each cycle (frequency of loading 0.1-0.025 Hz ΔV $7.4\text{x}10^{-4}$ mm to 0.5 mm/cycle	Cyclic *J*-R curve falls within the monotonic *J-R* curve scatter band for large ΔV. As ΔV on decreases and no of UL increased, the slope of *J*-Δa line decreased and it is least in the case of ΔV 0.74 μm. The linear summation of Δa_{cyclic} and $\Delta a_{tearing}$ leads to Δa_{total} measured from expt. Thus when the calculated Δa_{cyclic} component is subtracted from the Δa_{total} the cyclic *J-R* curves fall within the scatter band of monotonic *J-R* curve

UL: unloading; ΔV: incremental plastic displacement, σ_{ys}, σ_{uts} in MPa N.A. not available

Table 2.1 continued

Author	Material	Material Properties σ_{ys} σ_{uts} %El	Test parameters	Observations
Kobayashi [29]	2.5Cr-1Mo Steel quenched and tempered	510, 659, 28.8%	0.5, 0, -0.5, -1.5, increment of constant displacement	The cyclic *P-Δ* curve deviates to the lower side of monotonic *P-Δ* curve. They concluded that there exists no cyclic *J-R* curve to be contrasted with the monotonic *J-R* curve. In case of ductile tearing, the cyclic *J-R* curve is gradually changed to the monotonic *J-R* curve.
Mogami [30]	Reactor Pressure Vessel Steel A508 class 3 STS 42 carbon steel for piping	420, 545, 21.8% 279, 442, 35.6%	Stroke control *R* ratio 0 ΔV_{max},0.25mm 0.5 1.0 Load control *R* ratio 0.1, -1.0 P_{max} 27.5 kN 34.3 31.4 34.3 kN	Cyclic J_{max}-R curve coincides with the monotonic *J*-R curve. It has been observed that d*a*/dN cannot be extrapolated by Δ*J* if the value of d*a*/dN is about 3 to $1x10^{-5}$ mm/cycle. However they have suggested an equation in which J_{max} is used for extrapolating d*a*/dN. The value of *J* at instability for R= 0.1 and –1.0 were same as monotonic condition.

UL: unloading; Δ*V*: incremental plastic displacement, σ_{ys}, σ_{uts} in MPa N.A. not available

Table 2.1 continued

Author	Material	Material Properties σ_y, σ_{uts}, %El	Type of testing & R ratio	Observations
Dowling [34]	A533 B Pressure Vessel Steel	70 Ksi	Load control tests to sloping line	Crack growth rates in between $4x10^{-5}$ and 10^{-2} in/cycle shows excellent correlation with ΔJ using Rice et. al. approximation. At higher crack growth rates da/dN vs ΔJ data is agreement with the straight-line extrapolation on a log- log plot of the linear elastic fracture mechanics data. Macroscopic crack closure during gross plasticity is an important effect and significantly influences the fatigue crack growth rate. Growth rates during incremental plastic deflection cannot be predicted by a ΔJ criterion alone, a more general criterion that includes the effect of the mean J-level in needed.
Landes and McCabe [8]	HY130, A508 Cl 2	Not available	Displacement control ratcheting cracking	The two different steels showed different responses to the cyclic loading. HY-130 steel has no influence of cyclic loading. Cyclic J-R curve falls within the scatter band of monotonic J-R curve. Strong cyclic growth was observed for A508 Cl 2 steel crack growth increments for cyclic loaded cases are much higher than that for the monotonic case. The linear summation model suggested for determining the influence of the cyclic loading on the crack growth increments could not be conclusively evaluated.

UL: unloading; ΔV: incremental plastic displacement, σ_{ys}, σ_{uts} in MPa, N.A. not available

Table 2.1 continued

Author	Material	Material Properties σ_{ys}	σ_{uts}	%El	Test parameter	Observations
Landes et al. [9]	Modified 4340 steel	1041	1121	16%	Ratcheting crack (RC) Elastic Dominance	Cyclic loading has been found to alter the toughness behavior of this steel. For ductile fracture, *R* curves developed during cyclic loading appear to combine a monotonic and cyclic component of crack growth. A model using a linear combination of monotonic and cyclic crack growth could not predict the crack growth accurately. Additional component of crack growth to make up the short fall is termed as crack growth, model predicts results much better, although no mechanistic rational for this term was given.
Soek et al. [10]	SA 516 Gr70	NA			0.5, 0, -0.3, -0.6, -0.8 and –1.0	The crack growth resistance was found to decrease with decrease in stress ratio.
Rudland et al. [11]	304 SS, A106 GrB	NA			0, -0.3, -0.6, -0.8 and –1.0	The crack growth resistance was found to decrease with decrease in stress ratio. The effect of cycling saturates at *R* value of –8.0 and –1.0 for A106 steel for 304 SS respectively.

UL: unloading; ΔV: incremental plastic displacement, σ_{ys}, σ_{uts} in MPa N.A. not available

certain amount of crack growth takes place in each cycle that can be estimated by Paris law given by eqn (2.15). Assuming the total crack extension to be linear summation of "crack growth due to fatigue" and "monotonic crack extension", it follows that:

$$\frac{da}{dN_{total}} = \frac{(da_{fatigue} + da_{tearing})}{dN} \tag{2.16}$$

$$= \frac{da_{fatigue}}{dN} + \frac{da_{tearing}}{dN} \tag{2.17}$$

we know that

$$\frac{dJ}{da} = \frac{T_J \sigma_{ys}^2}{E} \tag{2.18}$$

where, T_J is the tearing modulus,

Equation (2.18) can be written as,

$$da_{plastic} = \frac{E dJ}{T_J \sigma_{ys}^2} \tag{2.19}$$

and $da_{fatigue}$ can be written as

$$\frac{da}{dN} = C_1(\Delta J_{fatigue})^{m_1} \tag{2.20}$$

where, C_1 and m_1 are constants derived from Paris law;

Substituting these in equation (2.17) one can get,

$$\frac{da}{dN_{total}} = C_1(\Delta J_{fatigue})^{m_1} + \frac{E dJ_{pl}}{T_J \sigma_{ys}^2} \tag{2.21}$$

A comparison of values obtained from experimental data of *a* vs *N* curve and those calculated from eqn.(2.21) showed a good agreement. When the number of cycles imposed is of the order of 20, the unloadings up to 90 to 100% do not result in any apparent cyclic crack extension and the *J-R* curves remain unaltered. An exception to this observation was reported by Joyce et al. [32] for ASTM designation A710 grade A class 3 steel having σ_{ys} and σ_{uts} of 643 and 732.3 MPa, respectively. They concluded that if *R* ratio is small, the cycling appeared to have little effect on the subsequent tearing resistance, but if *R* ratio was decreased the subsequent tearing resistance was also decreased.

2.3.2 Cyclic *J*-R curves for *R*<0

The summary of cyclic *J* investigations as listed in Table 2.1 suggests that number of reports on cyclic *J-R* curves for $R < 0$ is scanty. Among the few available

reports, the work of Landes and MaCabe [29] was the first to investigate the *J-R* curve behaviour under compressive cyclic loading. The investigations by Landes and MaCabe are on HY130 and A 508 steel using 1CT specimens. A schematic representation of different load histories applied to the specimens by these workers is shown in Fig.2.4 and the test conditions are shown in Table 2.2.

Table 2.2 Cyclic *J-R*-curve test conditions [8]

Material	Displacement at first unload, in.	Cyclic range, in.	Cyclic spacing in.	Total displacement in.	Number of Cycles
HY-130	0.035	0.035	0.005	0.100	13
HY-130	0.035	0.035	0.001	0.100	~70
A508 Cl 2	0.060	0.060	0.010	0.200	13
A508 Cl 2	0.100	0.060	0.002	0.250	~75

The study employed two methods of estimating *J*-integral. Landes and MaCabe [8] determined *J* from the positive area under the load displacement curves and compared with the scatter band of the monotonic *J-R* curves of the material. In the case of HY-130 steel, the developed *J-R* curve remained well within the scatter band of the monotonic *J-R* curve for both the displacement levels as given in Fig.2.5. However, A508 steel exhibited different nature in comparison to HY-130 steel. The *J-R* curves of A508 steel is reported to lie well within the monotonic *J-R* curve scatter band for the case of larger incremental displacement. For smaller displacements, where the specimen is subjected to five times more number of cycles, *J-R* curve was reported to fall much below the monotonic *J-R* curve scatter band as shown in Fig.2.6. The initiation toughness J_{IC} was reported lower for the specimen that experienced more number of cycles for A508 steel. An attempt has been made to model the extent of crack growth by linear summation. No convincing explanation has been provided for the above observations by the investigators [8].

In another report by Landes and Liaw [9], the effect of cyclic loading under negative *R* ratio on fracture toughness of modified 4340 steel has been discussed. The material was quenched and tempered to yield strength of 1041MPa (151Ksi). Standard 1CT specimens were tested by these investigators for both ratcheting loads and elastic dominance loads (as shown in Fig.2.4). In elastic dominance loading a progressively increasing maximum displacement is provided during each cycle and unloaded to zero

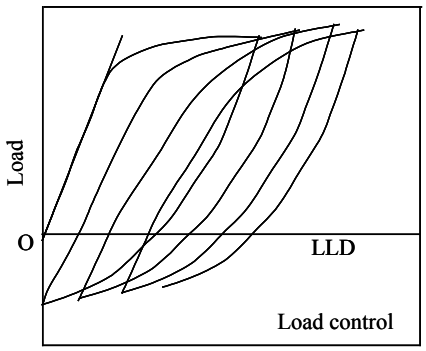

(a) Ratcheting Cracking

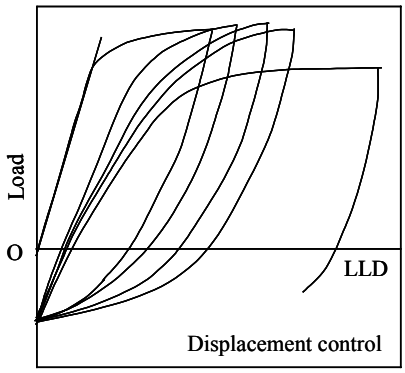

(b) Elastic Dominance

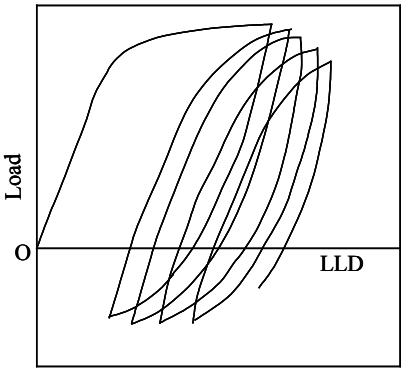

(c) First Unload beyond J_{Ic}

Fig.2.4 Type of load histories used for developing cyclic *R*- curves by Landes et al. [8]

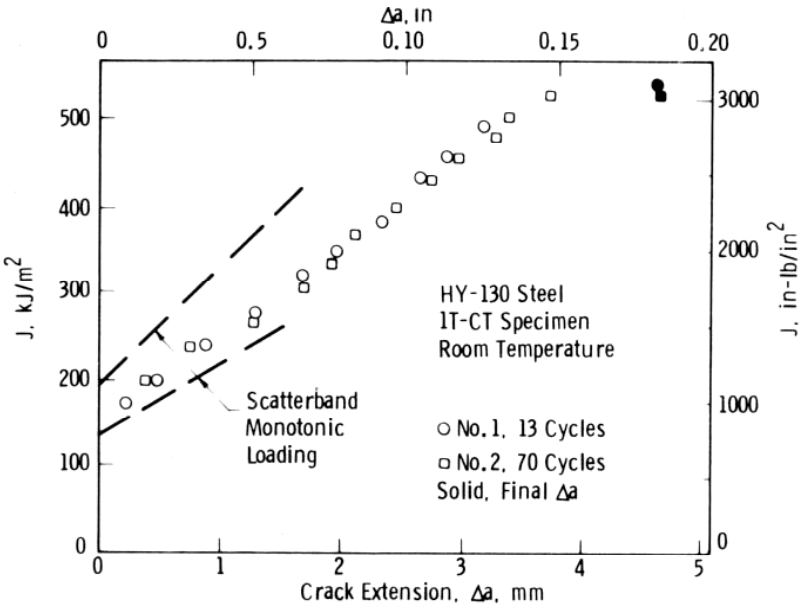

Fig.2.5 Cyclic *J–R* data for HY-130 steel [8]

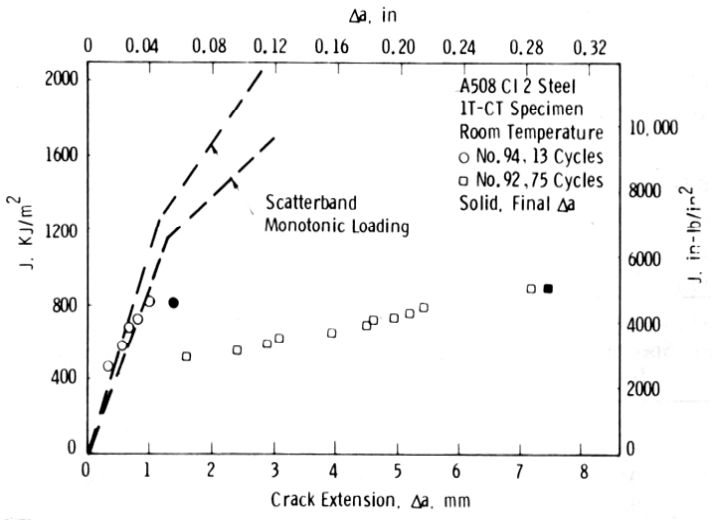

Fig.2.6 Cyclic *J–R* data for A508 Class 2 steel [8]

displacement levels. This type of tests simulated the case where the elastic boundary had such a large effect that the material always returns to starting strain level upon unloading. It has been observed by the authors [9] that the resistance to crack propagation is inferior in the case of cyclic loading in comparison to monotonic loading. The linear summation model of cyclic crack growth did not hold good for compressive cyclic loading in the case of modified 4340 steel.

Mogami et al. [30] also investigated the effect of complete cyclic reversal load on ASTM A508 class 2 and STS 42 steels. The authors have commented that cyclic J_{max}-R curve is lower than monotonic J-R curve but falls back on monotonic J-R curve for large crack extensions. They observed that cyclic J-R curve for a cyclic load of a high level, in which fatigue crack growth rate was about or above 0.1mm/cycle, nearly coincided with monotonic J-R curve. But cyclic J-R curve is reported to be placed lower than the monotonic J-R curve if unloading is started at lower J level, when fatigue crack growth rate was less than 0.1mm/cycle. To characterise fatigue crack growth aspects, the authors proposed an equation as given below

$$\frac{da}{dN} = C\left(\frac{\sqrt{\Delta J}}{(B\text{-}\sqrt{J_{max}})}\right)^{m} \tag{2.22}$$

Joyce [32] concluded that the cyclic J-R curve tests under COD control do not show significant effect on the ductile tearing toughness for A710 gradeA class 3 steel. It was also shown [32] that increasing the ductile tearing step in each cycle improves the resistance but this is always lower than the base line monotonic J-R curve for the steel investigated. Kobayashi et al. [29] have observed in the case of a 2.5Cr-Mo steel, that the J-R curve for R ratio of -1.5 falls below monotonic J-R curve and exhibits increased crack extensions. Rudland et al. [11] have reported, for 304 SS and A106 GrB plain carbon steel, that the fracture initiation toughness and the resistance to crack propagation decrease with decrease in stress ratio as well as decrease in plastic displacement. The effect of cycling on J-R curve saturates at a stress ratio of –0.8 and –1.0 for A106 steel and SS 304, respectively. Soek et al. [10,33] investigated the effect of reversed cyclic loading on the fracture resistance of SA 516 Gr 70 steel. They also reported that cyclic J-R curves fall below the monotonic J-R curve. Pronounced effect of decreasing R and decreasing incremental plastic displacement on lowering J-R curve are similar to the conclusions drawn by Joyce et al. [31]. On the basis of stress analysis, it was reasoned by these investigators that considerable amount of residual

tensile stress remains ahead of the crack tip when the load becomes zero at position 4, as in Fig.2.7 at the end of each cycle. Thus in the next cycle when the specimen is being loaded, crack tip opens up at a lower load level due to the additional residual tensile stress resulting in lower *J-R* curves. It was also shown that the stresses at the end of loading (position 3 in Fig.2.7) are compressive in nature and at position 4 only tensile residual stresses prevail. So there must be some point in between positions 3 and 4 where residual stress is zero. It is reasoned that the particular load level at which the residual stresses are zero should be taken for calculating operational *J*.

2.3.3 Dowling's Low Cyclic Fatigue Analysis

Dowling et al. [34] were the first to employ the *J* integral parameter in place of linear–elastic stress intensity factor, ΔK for cyclic crack growth. The cyclic *J* is evaluated by integrating the load-displacement data for each individual cycle. However, the integration is applied to the area DBCD as in Fig.2.8, against the conventional understanding of *J* (area EBFE). The point 'D' in the schematic diagram is derived from the analysis of crack closure. Owing to the reversed plasticity during the part of a cycle having compressive load, the crack tip does neither experience any tensile load, nor opens fully, till a significant magnitude of the load is acquired during reload part of the cycle. The Dowling's ΔJ is referred to as an operational *J* value and it is a modification of the classical *J* integral parameter. The Dowling's ΔJ methodology enables one to handle reverse loading, but the data analysis is complicated. This method needs the complete load-displacement data and information about crack closure during each cycle.

The Dowling's operational *J* has been denoted as ΔJ by the authors and was followed by several other researchers. The ΔK in LEFM regime of FCG is usually converted to ΔJ through the relation $\Delta J = (\Delta K)^2/E$, to obtain d*a*/d*N* data in terms of ΔJ. The ΔJ as discussed by Dowling will henceforth be denoted as ΔJ_D in further discussion to avoid any confusion.

Landes and McCabe [8] have also analysed the load-displacement data using Dowling's method. The results reported by these authors showed that d*a*/d*N* *vs.* ΔJ_D data for HY130 steel do not fall on the extrapolated line of d*a*/d*N* *vs* ΔJ data converted from ΔK, as shown in Fig.2.9. Crack growth is 5 to 15 times higher than the values of extrapolated fatigue data. The behaviour of HY130 steel was labelled as *R*-curve

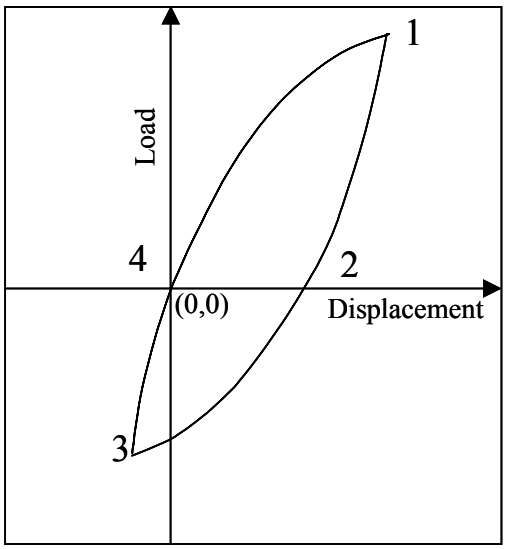

Fig 2.7 Hysteresis loop during cyclic loading [10]

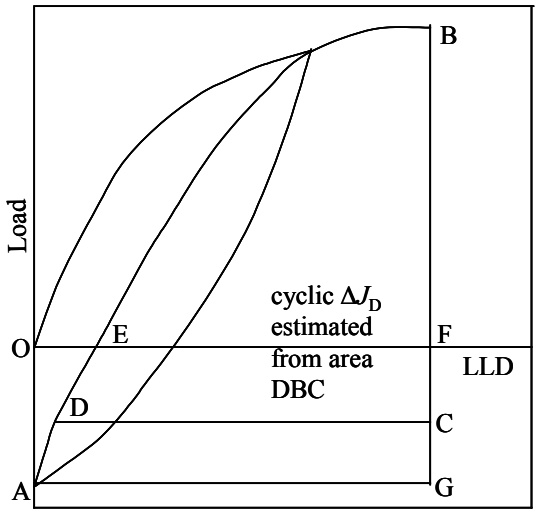

Fig.2.8 Dowling's operational definition of cyclic *J* [34]

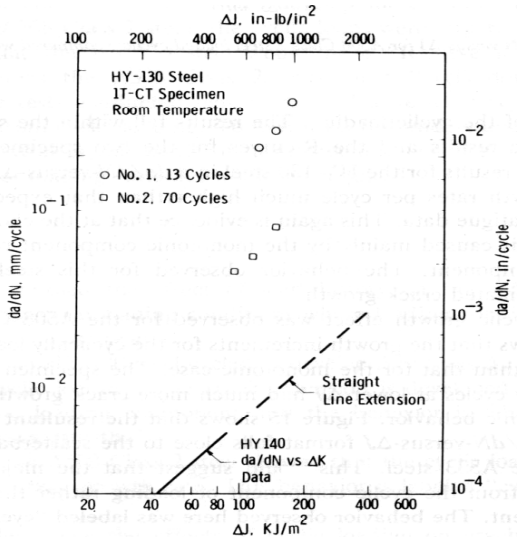

Fig.2.9 d*a*/d*N* vs Δ*J* for HY-130 steel loaded cyclically and compared with d*a*/d*N* data on HY-140 [8]

dominated crack growth. A strong cyclic crack growth effect was observed for A508 class2 steel by Mugami et al.[30]. The da/dN *vs* ΔJ_D plot for this steel falls within and near the da/dN *vs.* ΔJ data converted from ΔK as given in Fig.2.10. This suggests that a majority of crack growth occurred due to cyclic component of loading rather than monotonic component, labelled as cyclic dominated crack growth. The difference in cyclic *J-R* curves of these two steels has been attributed [30] to the differences in contribution of cyclic and monotonic components to the resultant crack growth.

The Dowling's ΔJ_D analysis when applied to 4340 steel, Landes and Liaw [9] have observed da/dN data to fall above the upper boundary of the extrapolated FCGR data obtained in LEFM regime. The crack growth rate is higher than what can be predicted from da/dN vs. ΔK plot. These investigators [9] made an attempt to develop a model through a linear combination of monotonic and cyclic components of crack extension. It was observed that the summation rule works well in both the loading conditions for a few initial cycles. After that, the Δa obtained experimentally was reported to be larger than the Δa evaluated from linear summation of monotonic and cyclic components.

The cyclic crack growth resistance of a material depends significantly on the *R* ratio. The compatibility of cyclic and monotonic crack resistance is sensitive to test conditions. Attempts to obtain cyclic crack extension in terms of monotonic crack growth plus fatigue crack growth are shrouded with controversy.

2.4 DYNAMIC STRAIN AGING

One of the major reasons for the discontinuous tensile flow behaviour of the materials is well known to be due to dynamic strain ageing. In this phenomenon the solute atoms are able to diffuse in a specimen at a rate faster than the speed of the dislocations so as to catch and lock them [35, 36] with resultant increase in load. But when the dislocations are torn away from the solute atoms there is a load drop. This process occurs many times, causing the serration in a stress-strain curve, which is the manifestation of DSA.

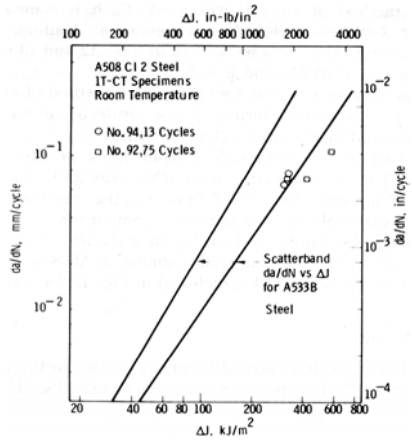

Fig.2.10 d*a*/d*N* vs Δ*J* for A508 Class 2 steel loaded cyclically and compared with d*a*/d*N* data on A533B [8]

2.4.1 Effect of DSA on Tensile Behaviour

Low carbon steels employed in power plant components are subjected to moderate temperature (28-350^{o}C) in service, and hence their tensile behaviour under varying temperatures has been investigated by several researchers [1-3,5-7,37]. In general engineering structural steels show decrease in yield strength (σ_{ys}) and ultimate tensile strength (σ_{uts}) with attendant increase in total percentage elongation (e_t) and percentage reduction in area (RA) with increase in temperature. However, some low carbon steels show fairly opposite trend i.e., hardening effect in the temperature ranges 100^{o}-370^{o}C [38]. Kim and Kim et al. [3,37] have observed an increase in the ultimate tensile strength with increase in temperature for SA 106 Gr C steel along with a corresponding decrease in percentage total elongation. Marschall et al. [6] have also observed similar trends for A106 steel in the strain rate range of $4x10^{-5}$ to $4x10^{-4}s^{-1}$. These observations are believed to reflect the occurrence of dynamic strain aging behaviour of the materials in the temperature range 200-350^{o}C [6]. The signatures of dynamic strain aging phenomenon can be observed in low carbon steels with the rise in test temperatures [39] as changes in the following properties

- An increasing trend of ultimate tensile strength with temperature
- A decreasing trend of ductility properties with increasing temperature
- Peak in the variation of work hardening exponent 'n' with temperature
- A minimum in the strain rate sensitivity (γ) with γ going negative in the temperature region of serrated flow.
- A peak in the variation of the Hall-Petch slope k_ε with temperature.

Dynamic strain aging is a time and temperature dependent phenomenon. Alteration in the rate of straining can shift the occurrence of DSA phenomenon from one temperature range to another temperature range. Singh et al. [5] have observed continuous increase in ultimate tensile strength when temperature was increased from 200 to 300^{o}C for SA333 Gr 6 steel and its weld metal. With increasing temperature, decrease in total elongation for both the materials at a strain rate of $1.2x10^{-4}s^{-1}$ has also been reported by these authors. These observations have been attributed to the possible occurrence of dynamic strain aging in SA 333 steel, But no detail account of DSA in SA333 steel is available.

2.4.2 Effect of DSA on Fracture behaviour

The reports available in literature on the influence of DSA on the fracture behaviour of steels are summarized in Table 2.3. In general it has been observed by several group of investigators [3,4,6,40-47] that DSA has detrimental effect on fracture toughness behaviour of a material. Both the fracture initiation toughness and the resistance to crack propagation are found to decrease in the DSA operative range with only one exception reported by Srinivas et al [48] who observed that in the DSA regime the value of fracture initiation toughness, J_{IC}, is maximum at 473^{o}K, for Armco iron. The reason for this behaviour has been attributed to the difference in the mechanisms of void nucleation and coalescence in Armco iron with respect to the other alloys. However, it has been observed by them that the slope of the *J*-*R* curve (d*J*/d*a*) i.e. tearing modulus or resistance to crack propagation decreased in DSA regime with a minimum value at 423^{o}K.

Seok and Murthy [49] have observed for 1CT specimens of A516 Gr 70 steel that there is no decrease in J_{IC}, even in DSA regime. The same group, however, have observed that the total energy to fracture, obtained from the area under the load-displacement plots for three point bend Charpy size specimens shows a dip in the DSA regime. Kang et al. [50] have found no influence of DSA phenomena on J_{IC} in SA 508 steel. A few other researchers [3,4,6,36,39-44,48,49] have observed lowest fracture toughness J_{IC}/ J_{Q}/ *CTOD* and *R* curve, in the DSA operative temperature regime. Kim and Kang [3] have pointed out that the direct current potential drop (DCPD) method is more sensitive to the crack initiation toughness induced by DSA than the ASTM unloading–compliance method. The results of Leak Before Break (LBB) analysis on SA 106 Gr C piping steel [40] and stress corrosion cracking in A533B steel [46] also showed the detrimental effects of DSA on fracture toughness properties of the materials.

In brief dynamic strain aging degrades fracture resistance of a material. But dynamic strain ageing occurs under specific combination of temperature and strain rate and such test conditions must prevail for the degradation of fracture toughness properties.

Table 2.3 Effect of DSA on Fracture Resistance Behaviour of Materials.

Author	Type of test	Steel	Remarks
Chakarvartty [40]	Tensile Test	ASTM A203 D nuclear structural steels	Area under the stress strain curve has been considered as measure of toughness and it was found to be less in DSA regime.
Mukherji [41]	Side grooved CT specimen, *J-R* curves	Schedule 100SA 106B piping and welds	Fracture initiation toughness, J_{Ic} and crack growth resistance curve were found to be less at 250^{o}C in comparison to 25^{o}C due to DSA.
Samuel [43]	Multi specimen J_{Ic} and single specimen testing; Crack length measurement using by DCPD technique	SS 316L	J_{IC} decreases with increase in temperature. dJ/da is independent of temperature upto 375^{o}C and decreases drastically by 50% at 550^{o}C
Srinivas [47]	Multiple specimen *J-R* curve	Armco Iron	J_{Ic} shows a maximum value at 200^{o}C; dJ/da decreases in the DSA regime with a minimum at 150^{o}C
Kang [3]	J_{Ic} as per ASTM E 813, J_i detection by DCPD technique	SA 508 nuclear pressure vessel steel	J_{Ic} determined as per ASTM is unaffected by DSA, but J_i determined by DCPD technique shows a minimum due to DSA. Tearing modulus shows similar trend as J_i.
Marengo [46]	J_{Ic} (as per ASTM E813-89) CTOD (ASTM E 1290-89) *J-R* curve (ASTM E-1152-87)	A 533 B and 516 70	All the three fracture toughness parameter J_{Ic}, *CTOD* and *J-R* curve are lowest in the DSA operative temperature range.
Kim [4]	Side grooved compact tension specimen, *J-R* curve testing	Steel 100 SA 106 B piping and welds	J_{Ic} and *J-R* curves lower at 250^{o}C than at 25^{o}C due to DSA.
Atkinson [44]	Slow strain rate test	A 533 B reactor pressure vessel steel	Stress corrosion cracking (SCC) enhances in DSA regime.
Kim [40]	Leak Before Break (LBB) analysis: True σ-ε curves and *J-R* curves from DCPD method	SA 106 GrC piping steel	J_i, dJ/da in DSA region were 30-40% lower than at room temperature. The leakage – crack size (LSC) length has a minimum with DSA at 296^{o}C and increases with increasing strain rate (an inverse effect). The LBB allowable load window is reduced by 30% in DSA regime.

2.5. THE LOW CARBON- STEELS USED IN NUCLEAR POWER PLANT

Low carbon steels provide moderate strength, good formability and ductility at relatively low cost. Thus it finds its application in a wider range. These steels having very low levels of inclusions possess high fracture toughness properties. They are used in fabricating critical components like primary heat transfer pipings and pressure vessels in the nuclear power plants. The design philosophy of these components is "leak before break (LBB)". In high risk containment vessels LBB design concepts ensure that any damage due to accidents or natural calamities like earthquake etc leakage of fluid precedes burst/ rupture of the component. High possibility of leakages being detected enhances safe operation of these components.

'Section II A: Ferrous Materials' of the Boiler and Pressure vessel code has various material specifications, that are employed in fabrication of nuclear power plants components. The corresponding ASTM specifications are given in the Annual book of "ASTM Standards vol.1.01 Steel-Piping, Tubing, Fittings". A large number of reports are available in the literature on the various aspects of steels used in nuclear power plants. Low carbon steels or low alloy steels having suitable mechanical properties and of low cost are abundantly used in the fabrication of several meters long primary heat transfer piping system (PHT) and pressure vessels. A list is given in Table 2.4, which provides general information about their specifications, relevant components for applications and nominal chemistry [6,28,30,49,51-54]. The material selected in the present investigation is ASME grade SA333 Gr 6 steel [51]. It is used in the primary heat transport system pipings (PHT) of pressurised heavy water reactors. The equivalent ASTM grade of this steel is A333/A333 M-94 [52]. The chemical composition and the minimum specified tensile properties as per several International specifications are given in Table 2.5 and Table 2.6 respectively.

Table 2.4 List of carbon steels used in nuclear power plants.

Sl.No.	Specification	Component	Composition wt%
1.	ASTM A 106 Grade B [6]	Coolant Pipings	C (0.28)-Si (0.18)-Mn (0.82)-Ni (0.11)-C r(0.11)
2.	ASTM A 533 Grade B [53]	Pressure vessel plate	C (0.25)-Si (0.24)-Mn (1.38)-Ni (0.61)-Cu (0.13)-Mo (0.49)
3.	ASTM A 508 Class 2 [30]	Re-circulation pipes, Pressure vessel nozzle	C (0.19)-Si (0.21)-Mn (0.88)-Ni (0.81)-Cr (0.40)-Mo (0.59)
4.	OX 540 [28]	Pressure vessel steel	C (0.2)-Si (0.12-0.5)-Mn (1.8)
5.	ASME SA 516 Gr 70 [10]	Pressure vessel plate	C (0.28)-Si (0.13-0.45)-Mn (0.79-1.30)
6.	ASME SA333 Gr 1 to 6 [51]	Pipes	C (0.30)-Si (0.058)-Mn (0.29-1.06)
7.	JIS* STS 42 [54]	Pipe	C (0.16)-Si (0.28)-Mn (1.30)
8.	JIS STS 49 [54]	Pipe	C (0.16)-Si (0.28)-Mn (1.14)
9	JIS SFVC2B [54]	Pipe	C (0.20)-Si (0.25)-Mn (1.16)
10.	JIS SGV 42 [54]	Pipe	C (0.15)-Si (0.22)-Mn (1.11)

Table 2.5 Nominal chemical composition of the SA 333 Gr. 6 steel [51,52].

Name of element	wt %
C	0.30
Mn	0.29-1.06
P	0.048
S	0.058
Si	0.10

Table 2.6 Minimum tensile properties of SA 333 Gr. 6 steel at 28^{o}C [51,52]

Properties	Longitudinal	Transverse
Yield strength (MPa)	241	240
Ultimate tensile strength (MPa)	414	415
Total elongation (%)	22%	12%

2.6 RE-APPRAISAL OF THE PROBLEM

The components such as heat transport pipes are designed on the concepts of leak before break (LBB). The LBB approach implies the application of fracture mechanics principles to demonstrate that the pipes are highly unlikely to experience sudden catastrophic rupture without prior indication of detectable leakage. The

assessment of structural integrity of the pipes requires the knowledge of the fracture initiation toughness and resistance to crack propagation of the material. This necessitates detailed understanding of fracture behaviour of the pipe material. However, the effects of different factors like *R* ratio, extent of plastic displacement and the crack plane orientations are also pertinent for the steel under consideration. It is known that this material shows embrittlement phenomenon through increase in ultimate tensile strength and decrease in ductility properties in the temperature range 200 to 300^{o}C. The effect of these embrittlement aspects on fracture toughness of the steel needs to be understood. For conservatism in the flaw assessment, there is a need to understand the crack propagation behaviour of this material in various cyclic loading situations and to establish suitable lower bound fracture mechanics parameters that can be used safely and confidently for LBB analysis.

This investigation has been directed to understand the process of crack initiation in SA 333 Gr 6 steel under various types of loading situations. Generation and analysis of data related to (a) effect of strain rate and temperature on tensile properties, (b) effect of temperature in monotonic fracture behaviour and (c) nature of cyclic *J*-*R* curve at different test conditions, are essential to bring forward such understanding.

3.0 THE SELECTED STEEL AND ITS CHARACTERISTICS

3.1. INTRODUCTION

The material selected for the present investigation is ASME SA 333 Gr 6 steel. It is used in the fabrication of primary heat transfer (PHT) piping of the nuclear power plants. These components operate in the temperature range of 28-300^{o}C. The material employed in such critical applications need understanding of the fracture behaviour in its operating temperature range. Any investigation of fracture properties of steel at elevated temperature a-priori needs information about its cleanliness, microstructure and general mechanical properties, particularly the tensile behaviour at elevated temperatures. The microstructural features like nature and morphology of the inclusions and the phases govern the macro level behaviour of a material. So it is imperative to know the nature of the selected steel with respect to its cleanliness, microstructure and the mechanical properties.

It is well documented in the literature, that the low carbon steels show dynamic strain aging behaviour in the temperature range 150-450^{o}C [2,3,37] and the occurrence of this phenomenon degrades the ductility and the fracture resistance of such steels [3-7,37,47]. The phenomenon of DSA is known to be governed by the temperature and the strain rate during a tensile test. The influence of DSA on the fracture resistance of a steel would thus be controlled by the prevailing temperature and strain rates at the point of crack initiation. Thus it is necessary to understand the dynamic strain aging behaviour of the selected steel in an appropriate window of strain rate and temperature before any elaborate investigation of the fracture toughness of the steel is attempted.

The aims of the investigation reported in this chapter are (i) to generate information about the microstructure and the cleanliness of the selected steel; (ii) to determine its conventional mechanical properties like hardness, tensile and impact toughness at ambient temperature; (iii) to examine tensile behaviour of the steel at and above ambient temperatures and at different strain rates and (iv) to understand the dynamic strain aging behaviour of the steel in the temperature range of 200^{o} to 300^{o}C at different strain rates.

3.2. EXPERIMENTAL

3.2.1. Chemical Analysis

The SA 333 Gr 6 steel used in this investigation was obtained as courtesy of Bhabha Atomic Research Centre, Mumbai, India. The steel was obtained in the form of sections of a pipe having external diameter of 406 mm and wall thickness of 32mm. A small piece (of dimension 25mm x 25mm x 5mm) was cut from the as received material and its opposite surfaces were made parallel by grinding. This sample was used for determining the chemical composition of the steel with the help of a Shimadzu Optical Emission Spectrograph (model: GVM 1014P). The nitrogen analysis was done using a series of cylindrical samples of 3mm diameter and 10 mm length. This analysis was carried out with the help of a Leo N_2 Determinator (model: TC436). The chemical composition of the steel thus obtained is given in Table 3.1.

Table 3.1 Chemical composition of the steel.

Elements	C	Mn	P	S	Si	Ni	Cr	Al	Cu	N
wt%	0.16	0.838	0.004	0.0014	0.19	0.04	0.06	0.008	0.043	0.0064

3.2.2. Metallographic Specimen Preparation

Small test coupons of approximately 10mm x 10mm x 10mm size were cut from the as received material for metallographic examinations. These specimens were first ground successively on silicon carbide abrasive papers having grit sizes between 80 and 1200. Next the specimens were successively polished on Texemet cloth either using diamond paste of particle sizes of 1μm and 0.25μm or using colloidal suspension of beta alumina having particle sizes of 0.25μm and 0.1μm. It may be mentioned here that a few of the samples were subjected to hardening treatment (austenitizing at 850^{o}C for 30 min followed by quenching in water) prior to polishing. These samples were used for inclusion characterization of the steel. Samples for microstructural studies were etched with freshly prepared 2% nital solution. The microstructural examinations were carried out on two representative planes, one surface perpendicular to the axial and the other in the circumferential direction of the pipe section (as shown in Fig.3.1), using a Union Versamet-2 metallograph. The two surfaces examined will

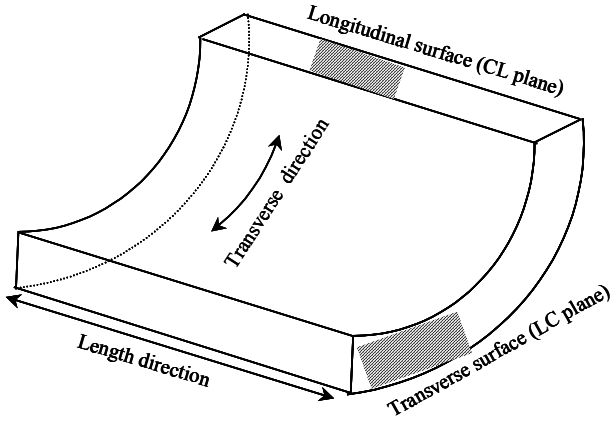

Fig.3.1 Configurations of specimen surfaces used for metallographic study

be henceforth, termed as LC and CL planes. This terminology conforms to crack plane designations for standard fracture toughness test specimens as per ASTM E-399 [55].

3.2.3. Inclusion Characterization

Inclusion characterization was carried out on water quenched and polished samples of both CL and LC planes (Fig.3.1). These samples were first examined using an optical microscope, when only a few inclusions could be observed even at high magnification of 1000x. Next, these specimens were examined with the help of a scanning electron microscope (JEOL model: 850A) at magnifications in the range of 1000x to 5000x, when the inclusions could be revealed in detail. The nature of a number of inclusions was ascertained using the EDAX system of the SEM. Typical representative photomicrographs of a few inclusions were recorded together with their EDAX analyses.

3.2.4 Metallographic Examination

The polished and etched metallographic specimens were studied using an optical microscope (Union Versamet-2) as well as a SEM. These examinations were carried out for both CL and LC planes of the pipe at different magnifications (150-2000x) and several representative microstructures of the specimens were recorded. In addition to revealing of the phases in the microstructures, the volume fraction of such phases, grain size and the banding index of the microstructures were also determined.

The volume fraction of the phases was determined manually by point counting technique following the ASTM standard E 562-89 [56]. A 20x20 grid was superimposed on a microstructure viewed at 400x magnification. Random counting was done on 30 fields of observations to estimate the mean volume fractions of the phases. The volume fraction, V_f, of a phase has been calculated using the following expression [56].

$$V_f = \frac{P}{n.P_o} \tag{3.1}$$

where P = total number of points on a phase

P_o = number of grid points

n = number of fields of observations

The amount of pearlite (V_f^P) was estimated and the volume fraction of ferrite (V_f^f) was evaluated as (1-V_f^P).

The ferrite grain size was determined at 400x using random linear intercept method following ASTM E112-96 [57]. In this method a linear test grid is superimposed on the microstructure and the number of ferrite grains intercepted by the test line are counted. A total number of 30 such random test lines were considered for obtaining the average ferrite grains. The mean ferrite grain size was calculated using the following equation [57].

$$L = \frac{V_f . L_T}{N} \tag{3.2}$$

where L = the mean ferrite grain size

V_f = volume fraction of ferrite phase

L_T = the total length of the superimposed grid lines

N = total number of ferrite grains intercepting the test lines.

The banding index was evaluated for both the CL and the LC planes, following the ASTM standard E-1268-94 [58]. The specimens were placed under the microscope and 50 images at 300x were captured for each type of specimen. After capturing the images, parallel and perpendicular grid lines of known length were drawn on each image and the pearlite colonies were used for counting the number of feature intercepts and the number of boundary intercepts. The number of feature intercepts N and the number of boundary intercepts P (as described in ref [58]**)** were counted for all grid lines parallel and perpendicular to the pearlite band. The average number of feature intercepts and the average number of boundary intercepts per unit length were calculated along both the directions parallel and perpendicular to the pearlite bands, as:

$$\cdot_{L\parallel} = \frac{\text{total no of feature intercepts counted parallel to the pearlite band}}{L_t} \tag{3.3}$$

$$P_{L\parallel} = \frac{\text{total no of boundary intercepts counted parallel to the pearlite band}}{L_t} \tag{3.4}$$

$$\cdot_{L\perp} = \frac{\text{total no of feature intercepts counted perpendicular to the pearlite band}}{L_t} \tag{3.5}$$

$$P_{L\perp} = \frac{\text{total no of boundary intercepts counted perpendicular to the pearlite band}}{L_t} \tag{3.6}$$

where, L_t = true test line in mm divided by magnification M

$\cdot_{L\parallel}$ = average number of feature intercepts per unit length parallel to the pearlite band

$P_{L\parallel}$ = average number of boundary intercepts per unit length parallel to the pearlite band

$\cdot_{L\perp}$ = average number of feature intercepts per unit length perpendicular to the pearlite band

$P_{L\perp}$ = average number of boundary intercepts per unit length perpendicular to the pearlite band

The feature counting and the boundary counting were done for over 100mm of test line length in each of the estimations for banding index. The degree of banding Ω_{12} was calculated using the following expressions [58].

$$\Omega_{12} = \frac{\cdot_{L\perp} - \cdot_{L\parallel}}{\cdot_{L\perp} + 0.571x\cdot_{L\parallel}} \tag{3.7}$$

$$\Omega_{12} = \frac{P_{L\perp} - P_{L\parallel}}{P_{L\perp} + 0.571xP_{L\parallel}} \tag{3.8}$$

The average banding index was evaluated from ten sets of readings. The banding indices calculated from feature intercept and boundary intercept, were found to be equal up to second decimal places. It may be mentioned here that the images were captured using an image analyser (Samsun Metal Power Image Analyser ver 2.2.05).

3.2.5 Hardness Evaluation

Hardness was evaluated on both CL and LC surfaces with the help of a Vickers Hardness Tester using a load of 20 kgf. The specimen surfaces used for hardness studies were polished following the procedure described in section 3.2.2 prior to hardness examination. At least ten indentations were taken to estimate the average value of hardness of the steel under investigation.

3.2.6. Tensile Testing

Round specimens of diameter 5mm and gauge length 25mm were fabricated for tensile tests following the ASTM standard E 8M-85 [59] from the as received pipe

section. The nominal dimensions of the tensile specimens and their orientation in the pipe section are shown in Fig.3.2 and in Fig.3.3. Specimens were fabricated for evaluating tensile properties for both axial and circumferential directions of the pipe section. The different orientations of the specimens will be henceforth termed as longitudinal and transverse as shown in Fig3.3.

All tensile tests were performed with the help of an INSTRON (model: 8562) electromechanical dynamic testing system fitted with a 100kN capacity load cell. The machine was equipped with 8500 digital controller interfaced to a personal computer through IEEE 488/GPIB protocols. The tests were conducted using Flaps 5, a Windows based software supplied by INSTRON. The software has provision for controlling the test conditions like displacement rate, and data acquisition on load, displacement and strain in different channels. The strain was measured through an extensometer of 25mm gauge length, attached to the middle of the specimen length. About 2500~3000 data points of engineering stress, percentage strain and displacement were acquired in each test for post processing. The tests were conducted at three different displacement rates, and four different test temperatures for each of the specimen orientations. The details of the test variables are shown in Table 3.2. Three specimens were tested for each of the combination of varied test conditions.

Table 3.2 Test variables for tensile tests.

Orientation	Displacement rate (mm s^{-1})	Nominal strain rate (s^{-1})	Test temperature (^oC)
Longitudinal	$3x10^{-2}$	$1.2x10^{-3}$	28
	$3x10^{-3}$	$1.2x10^{-4}$	200
Transverse	$3x10^{-4}$	$1.2x10^{-5}$	250
			300

The elevated temperature tensile tests were carried out in a three zone split type furnace placed around the specimen. The temperature of the specimen was monitored by a thermocouple tied at the centre of the test specimen. All elevated temperature tests were made with a temperature control of $\pm 3^oC$. For measurement of specimen

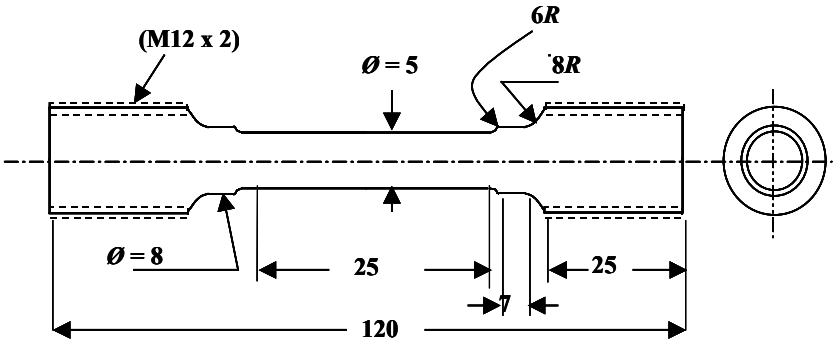

Fig.3.2 Typical round tensile test specimen

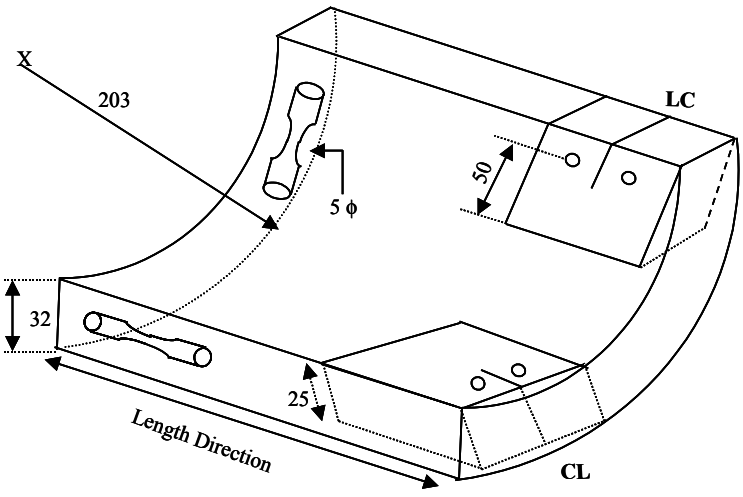

All dimensions in mm

Fig.3.3. Specimen configuration in pipe section

extension at elevated temperatures, an extensometer coupler was fabricated. The coupler is basically an axial rod and tube assembly with the ends fabricated to grip the specimen at one side and to facilitate attaching an extensometer (out side the furnace) on its other end. A 25mm gauge length extensometer was fitted for measuring extension of the sample. The set up for the specimen displacement measurement is shown in Fig.3.4. After tying the thermocouple and the extensometer assembly to the specimen, the furnace was enclosed and it was powered-up to achieve the desired test temperature. All tests were carried out after stabilizing the test temperature for 20~30 min. The digital data of stress, strain and actuator displacements for the tests at the strain rate $1.2x10^{-3}$, $1.2x10^{-4}$ and $1.2x10^{-5}s^{-1}$ were acquired at 10, 1 and 0.1Hz respectively.

3.2.7. Fractographic Examination

The fractured surfaces were cut out carefully from the broken tensile specimens and were ultrasonically cleaned prior to their examination under a scanning electron microscope. A series of representative fractographs were recorded during such examinations on fractured surfaces cut from both the longitudinal and the transverse tensile specimens tested at 28, 200, 250 and 300^{o}C.

3.2.8 Impact Toughness Testing

Standard Charpy impact specimens of size 10mm x 10mm x 55mm with 2mm deep V notch were machined. Specimens of orientation LC, CL and LR as per ASTM E-399-90 [55] guidelines were prepared. Tests were carried out at 28^{o}C using a WOLPERT Instrumented Charpy Impact Testing machine as per ASTM standard E23-94 [60]. A minimum of five specimens was tested to estimate the average CVN value for each orientation of the pipe section. All these tests were carried out at room temperature.

3.3. RESULTS AND DISCUSSION

3.3.1 Material Characteristics

The chemical composition of the steel is given in Table 3.1. Repeated analyses did not show variations of more than two units on the last significant decimal place of

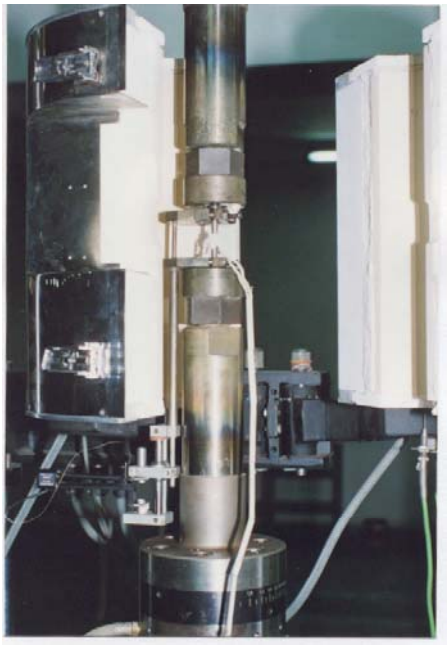

Fig.3.4 Set up for the displacement measurement of a tensile test specimen.

each elemental composition (as given in Table 3.1) and hence the analysis is considered reliable. The obtained composition indicates that the amount of carbon, manganese, phosphorous, sulphur and silicon in the investigated steel is in accordance with the ASTM A333 Gr 6 or ASME SA 3333 Gr 6. The steel will be henceforth referred to as SA333 for convenience of discussion. However, it may be mentioned at this stage that the investigated steel contains some minor amount of nickel, chromium, aluminum and copper, which are not included in the standard designation of ASTM A333 Gr6 or ASME SA 333 Gr6.

A small number of inclusions of finer sizes could be detected using optical microscope only at high magnifications such as 1000x. Hence, inclusion rating as per ASTM standard E45-87 [61] procedure could not be carried out for this material. The longitudinal surface of the specimen shows an array of fine size inclusions inclined at some angle to the length of the pipe as shown in Fig.3.5. It was possible to distinguish the size and the morphology of the inclusions by SEM both on CL and LC planes (as shown in Fig.3.1) at magnifications higher than 1000x. A typical photo-micrograph of an elongated inclusion on CL plane is shown in Fig.3.6(a). The EDAX analysis for such inclusions is illustrated in Fig.3.6(b), which indicates that the inclusions are MnS which are normally expected in plain carbon steels. The photo-micrograph of an almost spherical inclusion and its EDAX analysis as obtained on the LC plane are given in Fig.3.7(a) and Fig.3.7(b) respectively. The EDAX results in Fig.3.7(b) indicate the inclusion to be of mixed type containing both oxide and sulphide. Most of the inclusions detected in this steel are found to be primarily of sulphide type. Only a few inclusions were of mixed (oxide and sulphide) type.

Representative optical and SEM photomicrographs of the longitudinal and transverse sections of the pipe at different magnifications are shown in Fig.3.8, Fig.3.9 and Fig.3.10. A series of micrographs are presented, in order to illustrate the phases and their distribution in the microstructure, which reveal ferrite and pearlite having significant degree of banding. Whereas, Fig.3.8 shows the nature of banding, the same has been illustrated at different magnifications in Fig.3.9 and Fig.3.10 to reveal the nature and distribution of the ferrite phase and the pearlite colony. The estimated average volume fraction of the phases, the mean ferrite grain size and the banding indices for the CL and LC planes are compiled in Table 3.3. Visual examination of the

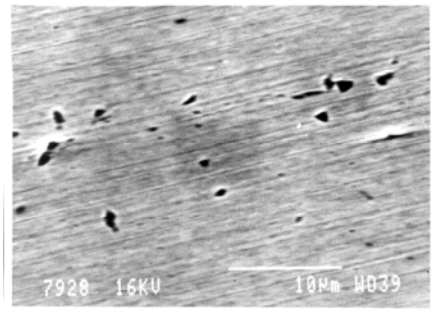

Fig.3.5 Typical array of inclusions present in the longitudinal surface of the specimen.

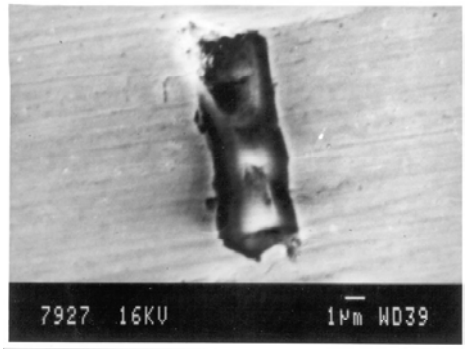

Fig.3.6(a) A typical elongated inclusion on the longitudinal surface of a specimen.

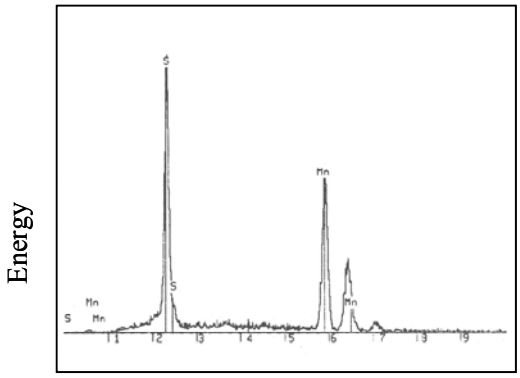

Fig.3.6(b) The EDAX analysis of the elongated inclusion shown in Fig.3.5(a)

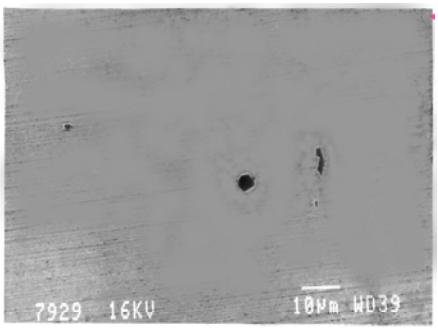

Fig.3.7(a) A typical globular inclusion on the transverse surface of a specimen..

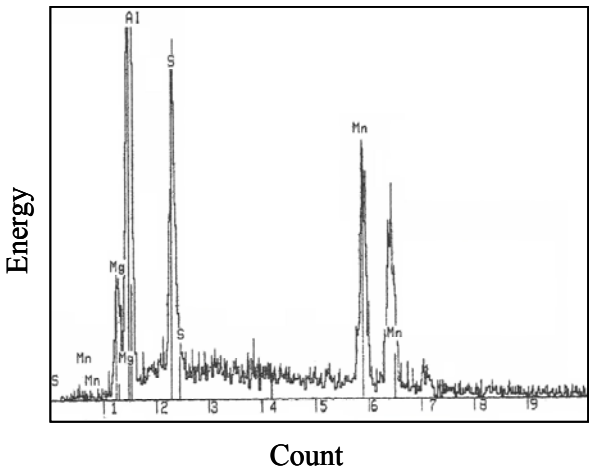

Fig.3.7(b) The EDAX analysis of the globular inclusion shown in Fig.3.6(a).

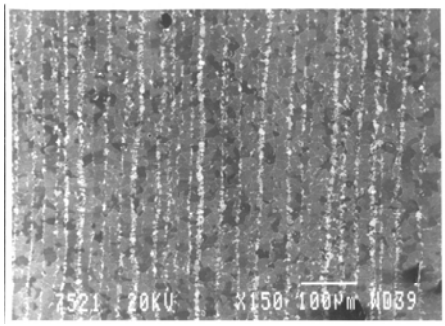

Fig.3.8(a) Typical photo-micrograph of the longitudinal surface of a specimen.

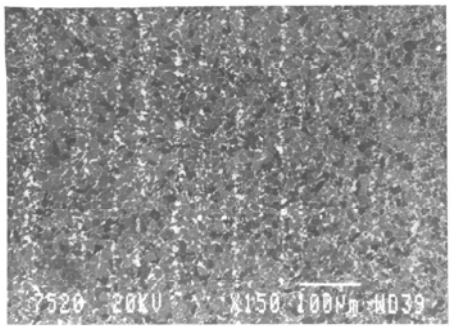

Fig.3.8(b) Typical photo-micrograph of the transverse surface of a specimen.

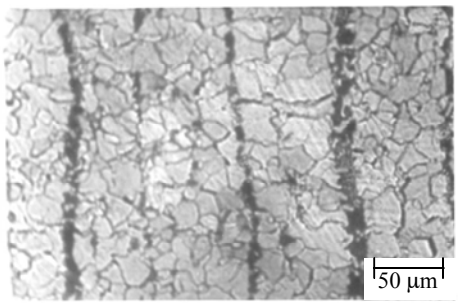

Fig.3.9(a) Typical photo-micrograph of the longitudinal surface of a specimen.

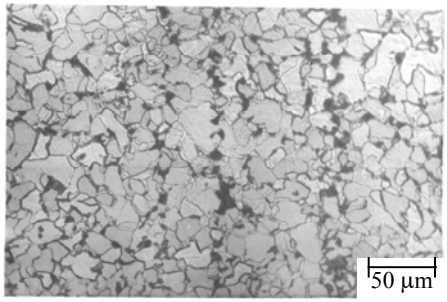

Fig.3.9(b) Typical photo-micrograph of the transverse surface of a specimen.

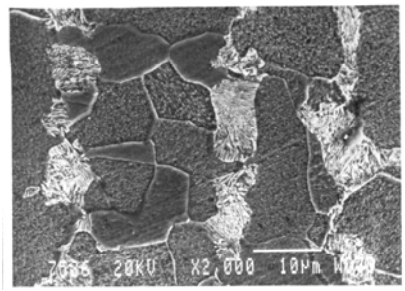

Fig.3.10(a) Typical photo-micrograph of the longitudinal surface of a specimen.

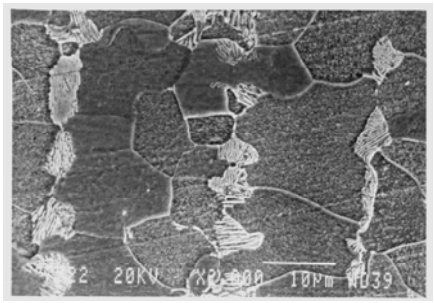

Fig.3.10(b) Typical photo-micrograph of the transverse surface of a specimen.

micrographs in Fig.3.8 and Fig.3.9 indicate that the severity of banding is more in the CL plane than that on the LC plane. Thus, the estimated banding indices of 0.468 and 0.358 for CL and LC planes respectively appear to be in order. The average volume fraction of pearlite on CL and LC planes was found to be 20.6 and 21.3 percentage, respectively. The theoretical calculations show that the volume fraction of ferrite V_f^P should be 80.8%. The differences between the V_f^P on CL and LC planes are within the associated standard deviations of the estimated mean value of V_f^P. The difference between the theoretical and experimental values is due to the presence of minor amount of alloying elements in the steel. The mean ferrite grain size on the CL and LC planes was found to be 14.5±1.2μm and 14.3±1.3μm, respectively.

Table 3.3 Average volume fraction of pearlite, mean ferrite grain size and average banding index of the steel.

Orientation	Average volume fraction of pearlite V_f^P (%)	Mean ferrite grain size, (μm)	Average Banding Index Ω_{12}
Longitudinal	20.6±1.5	14.5±1.2	0.468
Transverse	21.3±1.4	14.3±1.3	0.358

The average Charpy impact toughness values of the three different specimen orientations namely LC, CL and LR are given in Table 3.4. The impact energy value is found to be minimum for specimens having CL orientation (235J); but the CVN values for LC and LR orientations are almost the same at around 292J. The minimum CVN values for specimen with CL orientation are attributed to the presence of elongated inclusions on the CL plane as evidenced in Fig.3.6.

Table 3.4 Average CVN impact toughness of the steel.

Specimen orientation	CVN toughness (Joule)
LC	294
CL	235
LR	291

The average hardness of the steel was found to be 133 and 134 VHN on the CL and LC planes. The tensile properties of the longitudinal and the transverse specimens

tested at a strain rate of $1.2x10^{-4}$ s^{-1} at ambient temperature (28°C) are reported in Table 3.5. The tensile properties of the investigated steel were found to be in accordance with the values reported for ASTM A333 Gr 6 or ASME SA333 Gr 6 [51,52] steel.

Table 3.5 Mechanical properties of the steel

Types of specimen	Yield strength $\sigma_{ys,}$ (MPa)	Tensile strength σ_{UTS}, (MPa)	Total elongation e_t, (%)	Reduction in area RA, (%)
Longitudinal	328±15	452±22	39.5±2	75.0±4
Transverse	320±15	459±22	38.0±2	72.9±4

From the routine mechanical properties and microstructural details reported above, it may be noticed that, the features and properties are more or less same in both LC and CL planes of the pipe material. Only the impact toughness in CL orientation shows inferior properties and in this plane, the inclusions were also observed to be elongated and were directionally oriented.

3.3.2. The Tensile Behaviour at Elevated Temperature

Tensile tests were carried out at four different temperatures and at three different strain rates using both longitudinal and transverse specimens as shown in Table 3.2. In all, there were twenty-four test conditions in which these tests were done and at each of these conditions three tests have been performed. Typical engineering stress-strain plots at the strain rate of $1.2x10^{-4}$ s^{-1} and at the test temperatures of 28, 200, 250 and 300°C for longitudinal and transverse specimens are shown in Fig.3.11 and Fig.3.12 respectively. Such engineering stress-strain plots for all the test conditions can be broadly classified with the codes TI, TII and TIII following Hertzberg [35] as:

TI: Elastic-Heterogeneous Plastic - Homogeneous Plastic Response

TII: Elastic-Heterogeneous Plastic Response

TIII: Elastic-Homogeneous Plastic Response

The observed nature of the stress-strain curves has been mapped in Fig.3.13 and Fig.3.14 for longitudinal and transverse specimens respectively. At room temperature for both the specimen orientations, the stress-strain curves are elastic-heterogeneous plastic-homogeneous plastic (TI) in nature. But at 200 and 250°C the

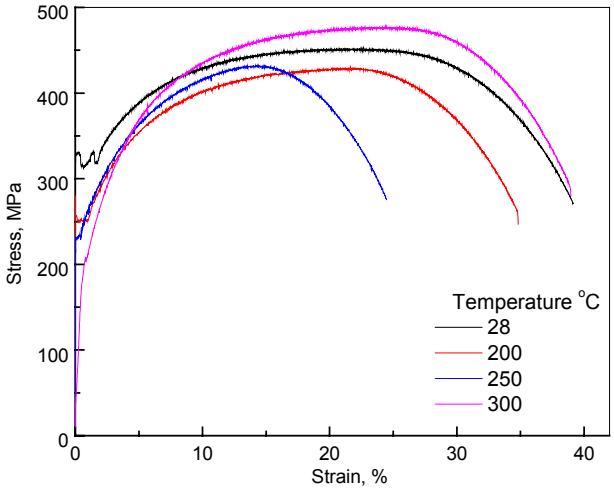

Fig.3.11 Typical engineering stress-strain curves of the longitudinal specimens at the strain rate $1.2x10^{-4}$ s^{-1}

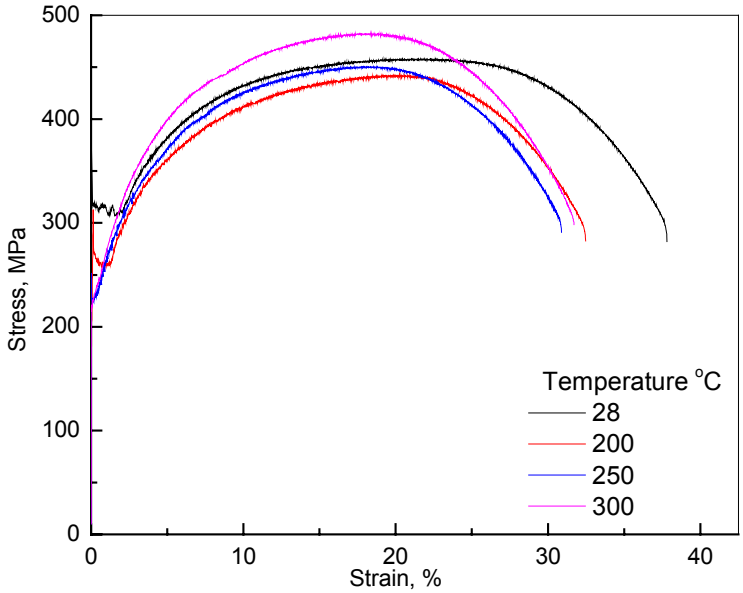

Fig.3.12 Typical engineering stress-strain curves of the transverse specimens at the strain rate $1.2x10^{-4}$ sec^{-1}

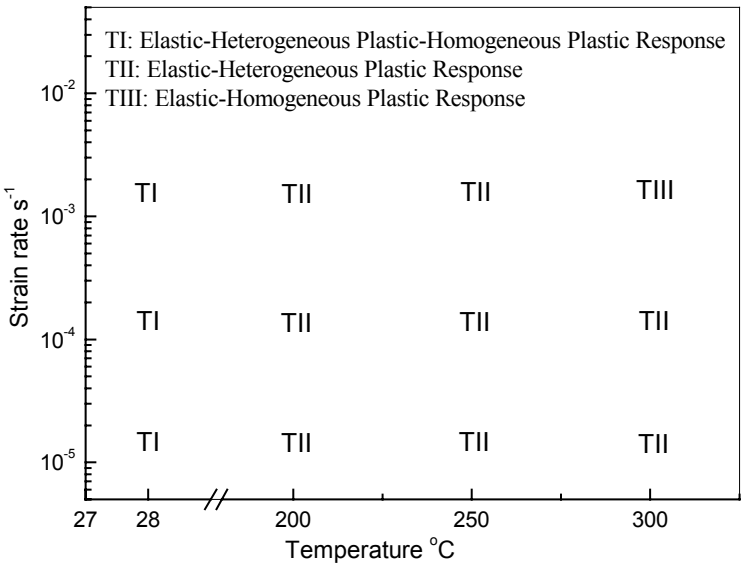

Fig.3.13 A map showing the classification of stress-strain curves for the longitudinal specimens at diffrent test conditions.

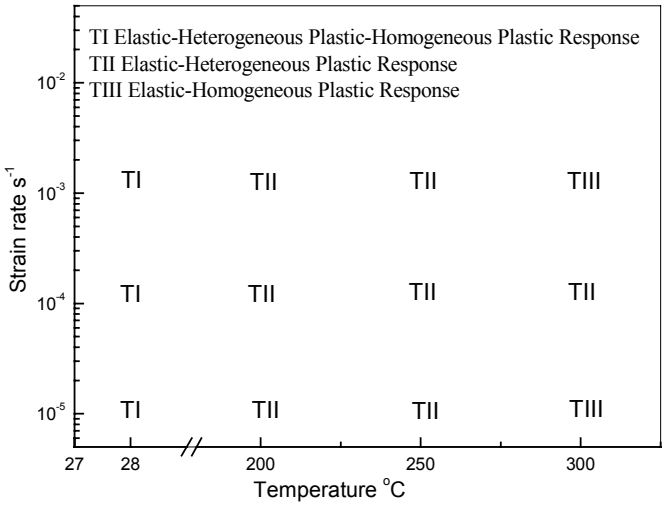

Fig.3.14 A map showing the classification of stress-strain curves for the transverse specimens at diffrent test conditions.

stress-strain curves are of elastic heterogeneous plastic (TII) in nature at all the investigated strain rates for both specimen orientations. The elastic-homogeneous plastic response (type TIII) in deformation behaviour was obtained only at 300^{o}C for the strain rate 1.2x10^{-3} s^{-1} for longitudinal specimen and for strain rates 1.2x10^{-3} and 1.2x10^{-5}s^{-1} for the transverse specimens. The TI and TII types of stress-strain curves exhibit a series of serrations, superimposed on the pre-necking regime of the curve and these reflect heterogeneous deformation in the material. Five major types of serrations in stress-strain curve namely A, B, C, D and E types have been categorized in the literature [62-66]. The nature of the serrations in the present stress-strain plots will be discussed further in the next section.

The yield strength, (σ_{ys},) ultimate tensile strength (σ_{uts}), percentage uniform elongation (e_u) and percentage total elongation (e_t) have been evaluated from the engineering stress-strain plots. The test conditions at which the stress–strain curves were found to exhibit distinct upper and lower yield point, the latter has been taken as the yield strength of the material. Alternatively the stress corresponding to 0.2% offset strain value was taken as the yield strength of the material when there were no distinct yield point phenomena. The maximum stress value exhibited by each stress–strain curve was taken as the ultimate tensile strength of the material and the strain corresponding to this value is considered as the percentage uniform elongation. The maximum strain (in percentage) from each stress–strain curves was taken as percentage total elongation; percentage reduction in area was estimated by measuring the diameter of a specimen before and after the test at the location of fracture. The average values of all these properties are reported in Table 3.6. The mean values of σ_{ys}, σ_{uts}, e_u, e_t and RA were estimated from the test results of the three specimens and it was noted that the individual readings were within ±5% of the mean value.

The influence of temperature on yield strength (σ_{ys}) and tensile strength (σ_{uts}) of the steel at the investigated strain rates are shown in Fig.3.15 and Fig.3.16, for the longitudinal and transverse specimens respectively. As expected, the yield strength of the steel was in general, found to decrease with increase in temperature for all the specimen conditions that were tested. The ultimate tensile strength of the material, on the other hand, was found to decrease marginally between the test temperatures of 28 and 200^{o}C, followed by a distinct increase between 200 and 300^{o}C for the longitudinal

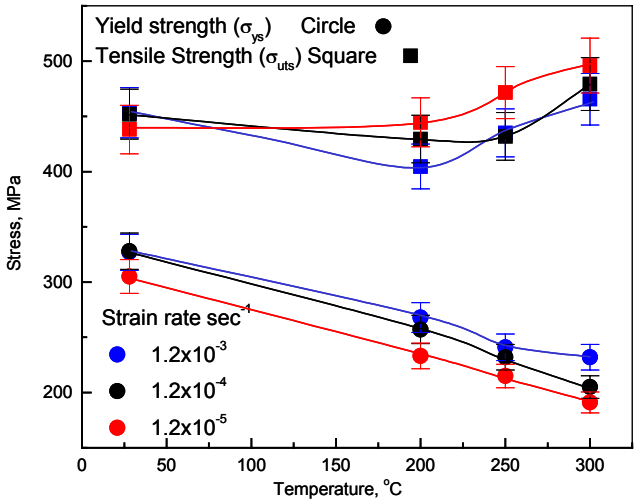

Fig.3.15. Variation of yield (σ_o) and tensile strength (σ_{uts}) with temperature for the longitudinal specimens at all the investigated strain rates

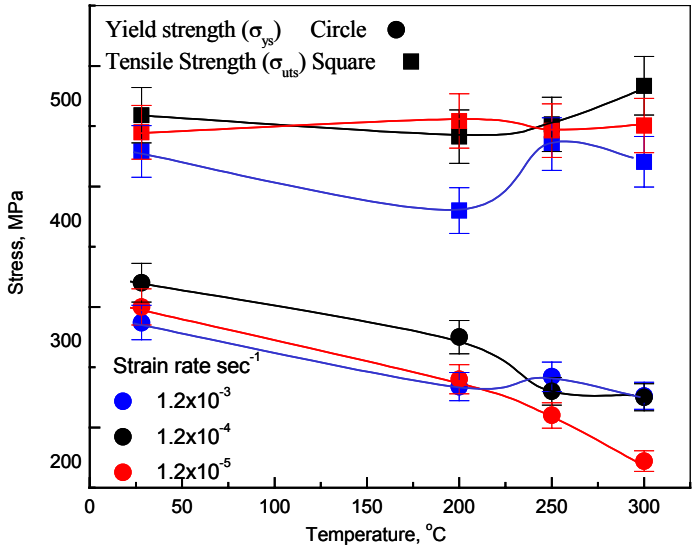

Fig.3.16. Variation of yield (σ_{ys}) and tensile strength (σ_{uts}) with temperature for the transverse specimens at all the investigated strain rates

specimens. The nature of variation of σ_{uts} with temperature for the transverse specimens resembles to those of the longitudinal specimens; but the change in σ_{uts} with temperature between 200 and 300^{o}C does not depict a generalized trend as it has been observed in the longitudinal specimens. In addition, it is noted that higher strain rates resulted in lower σ_{uts} value for longitudinal specimens tested between 200 and 300^{o}C temperature, contrary to the expected trends. The influence of strain rate on σ_{uts} between 200 and 300^{o}C do not provide any generalized pattern.

The influence of temperature on uniform (e_u) and total elongation (e_t) is shown in Fig.3.17 and Fig.3.18 respectively for the longitudinal specimens. Similar plots for the transverse specimens are shown in Fig.3.19 and Fig.3.20. The variation e_u and e_t with temperature at different strain rates lead to the following inferences:

(a) The longitudinal specimens show a general decrease in the magnitude of e_u and e_t at all the strain rates with the increase in temperature from 28 to 250^{o}C, there after at 300^{o}C temperature it shows an increasing trend. The minimum total elongation has been observed at 250^{o}C for the longitudinal specimen at a strain rate of $1.2x10^{-4}s^{-1}$.

(b) The magnitude of e_u for transverse specimens remains almost unchanged between 28 and 200^{o}C temperature at all the strain rates, but the e_t values show a decreasing trend with increase in temperature from 28 to 300^{o}C. The magnitude of e_u shows an increasing trend with a rise in temperature from 200 to 300^{o}C for the transverse specimen at a strain rate $1.2x10^{-3}$ s^{-1}.

(c) The magnitude of e_u and e_t were found to increase steeply from its minimum value with increase in test temperature.

(d) For longitudinal specimens the magnitude of e_u and e_t were found to increase with increase in strain rates at 28 and 200^{o}C; but such a general trend was not observed for the range of temperatures under investigation. The variation of e_u and e_t at different strain rates for the transverse specimens also do not show any consistent trend.

Over all, the decrease in the magnitude of e_u and e_t with increase in temperature at a particular strain rate or that with decrease in strain rate at a particular temperature are opposite to what is commonly expected. It is well established that

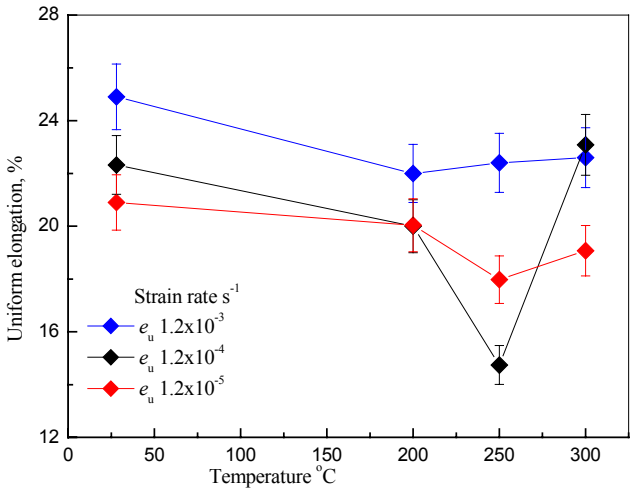

Fig.3.17 Variation of uniform elongation (e_u) with temperature for the longitudinal specimens.

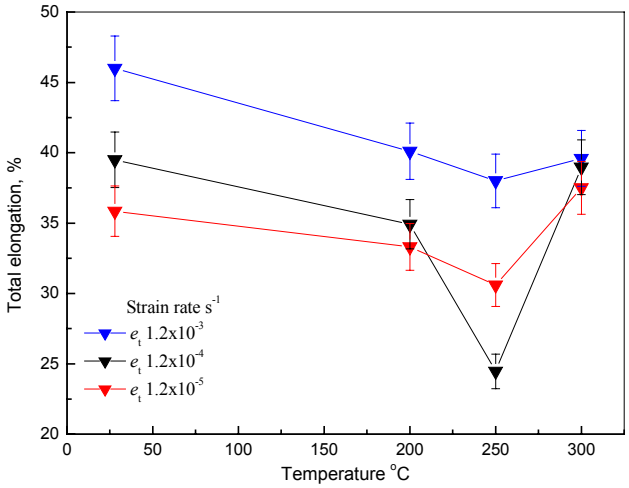

Fig.3.18 Variation of total elongation (e_t) with temperature for the longitudinal specimens.

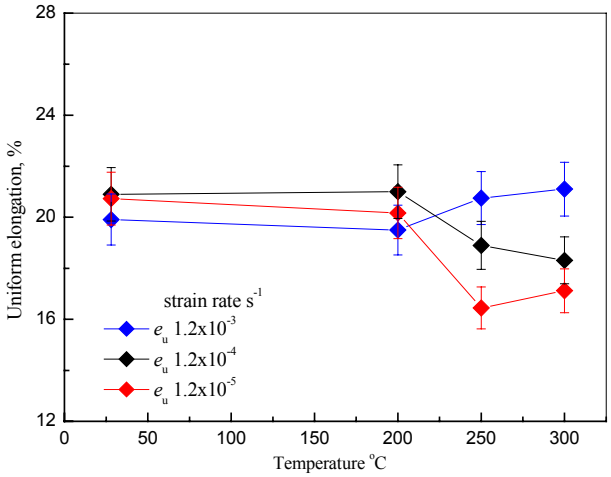

Fig.3.19 Variation of uniform elongation (e_u) with temperature for the transverse specimens.

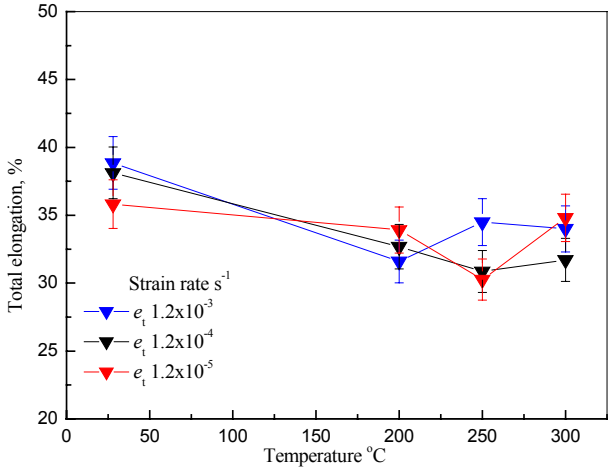

Fig.3.20 Variation of total elongation (e_u) with temperature for the longitudinal specimens.

increase in test temperature or decrease in strain rates commonly enhance the ductility of a material [67,68].

The influence of temperature on reduction in area (RA) of the steel is shown in Fig.3.21 and Fig.3.22 for longitudinal and transverse specimens respectively at all the strain rates. The variation in the percentage reduction in area RA with temperature also shows a similar trend as that of e_u and e_t *vs* temperature at all the investigated strain rates for the longitudinal specimens. The trends of variation of RA with temperature for transverse specimens do not depict any generalized pattern. In general, under the employed test conditions the minimum value of RA is observed in tensile tests conducted at 250^oC with the only exception for transverse specimen tested at $1.2x10^{-4}$ s^{-1}. The nature of variation of RA with test temperature and strain rates is also in disagreement with the conventional understanding of variation in ductility with test temperature and strain rate.

The material shows 50-60 MPa increase in ultimate tensile strength (Fig.3.15) and a slight decrease in ductility properties with increase in test temperature from 200 to 300^oC (Fig.3.17) for all the investigated strain rates for longitudinal specimens. Singh et al. [5] have reported similar observations for SA333 Gr6 steel. Kim et al. [4] and Marschall et al. [6] have observed an increase in ultimate tensile strength and decrease in percentage total elongation for SA106 Gr C and SA106 Gr B steels. The presence of serrations in the pre-necking region of engineering stress-strain plots have been also reported by these authors [4,6] for SA 106 Gr C steels. The reason for such abnormal behaviour has been attributed to dynamic strain aging phenomena in these steels [4-6]. Thus the obtained tensile results in this investigation indicate that a dynamic strain aging, (DSA), phenomenon is taking place in this material at elevated temperature.

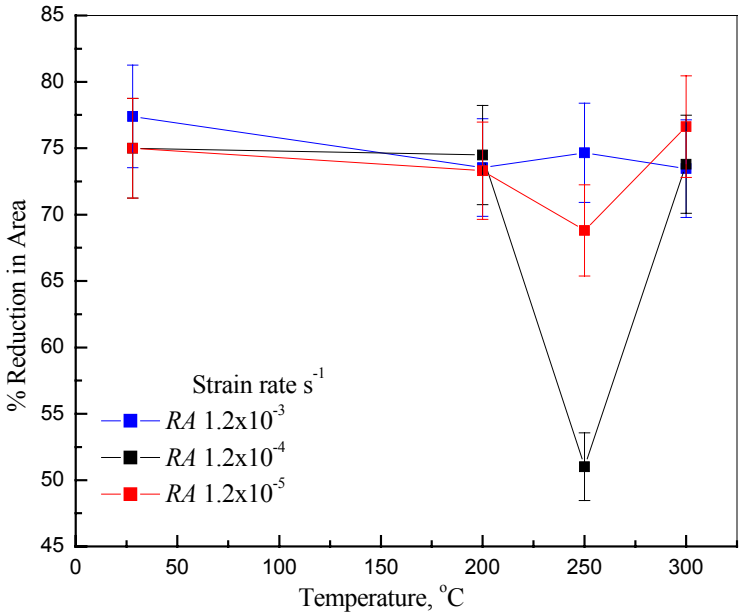

Fig.3.21 Variation of Reduction in Area (*RA*) with temperature for the longitudinal specimen at all the strain rates.

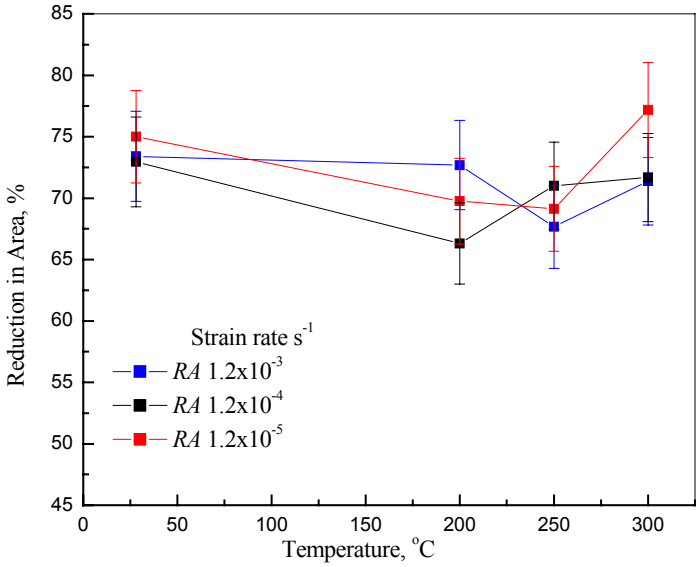

Fig.3.22 Variation of reduction in area (*RA*) with temperature for the transverse specimen at all the strain rates

Table 3.6 Average tensile properties of the steel under investigation

Temperature (^{o}C)	σ_{ys} (MPa)	σ_{uts} (MPa)	e_u (%)	e_t (%)	RA (%)	Strain Rate (s^{-1})
Longitudinal						
28	311	453	25.5	45.6	77.4	$1.2x10^{-3}$
200	262	405	19.0	35.5	73.5	$1.2x10^{-3}$
250	237	435	22.2	37.7	74.6	$1.2x10^{-3}$
300	228	465	22.5	37.5	73.5	$1.2x10^{-3}$
28	328	452	22.3	39.5	75.0	$1.2x10^{-4}$
200	257	429	20.0	34.0	74.5	$1.2x10^{-4}$
250	232	432	14.7	24.5	51.0	$1.2x10^{-4}$
300	205	479	23.1	38.9	73.8	$1.2x10^{-4}$
28	305	438	20.9	36.5	75.0	$1.2x10^{-5}$
200	233	444	20.0	33.3	73.3	$1.2x10^{-5}$
250	215	471	17.9	30.6	68.8	$1.2x10^{-5}$
300	193	499	19.1	37.3	76.6	$1.2x10^{-5}$
Transverse						
28	287	429	19.9	38.8	73.4	$1.2x10^{-3}$
200	234	380	19.5	31.8	72.7	$1.2x10^{-3}$
250	242	435	20.7	35.1	67.7	$1.2x10^{-3}$
300	226	420	21.1	34.0	71.3	$1.2x10^{-3}$
28	320	459	20.9	38.0	72.9	$1.2x10^{-4}$
200	275	441	21.0	32.7	66.3	$1.2x10^{-4}$
250	230	451	18.9	30.8	71.0	$1.2x10^{-4}$
300	229	483	18.3	31.7	71.7	$1.2x10^{-4}$
28	300	445	20.7	35.8	75.0	$1.2x10^{-5}$
200	240	454	20.2	33.3	69.7	$1.2x10^{-5}$
250	210	446	16.4	30.26	69.1	$1.2x10^{-5}$
300	172	450	17.1	34.81	77.2	$1.2x10^{-5}$

σ_{ys} - Yield strength, σ_{uts} - Tensile strength

e_u - Uniform elongation, e_t - Total elongation, RA - Reduction in area

3.3.3. Dynamic Strain Aging Behaviour of the Material

The observed increase in σ_{uts} and decrease in e_u and e_t with increase in temperature, and TII type stress-strain curves, as shown in Fig.3.13 and Fig.3.14, infer that the steel exhibits dynamic strain aging at several conditions of tensile tests. The heterogeneous plastic response is marked with serrations primarily in the pre-necking region of the stress-strain curves. The serrated stress-strain response can occur in metals and alloys due to any one or a combination of the following reasons:

(a) Interaction of moving dislocations with interstitial or substitutional atoms [1,39,69-72].

(b) Continuous mechanical twinning in hexagonal close-packed metals [35,73].

(c) Order-disorder transformations taking place at the test conditions [74,75].

(d) Phase transformations induced by stress and strain changes in the material [76].

By principle of exclusions, the observed DSA in SA 333 steel in the present investigation may be attributed to the interaction of moving dislocations with the interstitial atoms. The interaction of solute atom with mobile dislocation is described as follows: when sufficient amount of stress is available during tensile deformation, dislocations become free from the interstitial carbon and nitrogen atoms or the solute clusters like Mn and nitrogen [2,70,71,77], resulting in a small drop in the flow curve. The solute atoms are able to diffuse again to the dislocations and re-trap them causing an increase in the flow stress. The repeated occurrence of these two phenomenon leads to the formation of serrations in the pre-necking region of engineering stress-strain plots. During this process the plastic strain rate fluctuates around the imposed strain rate, because of varying dislocation density.

An attempt was made to examine the nature of serrations obtained in various stress-strain curves. In order to do this, the pre-necking regions of the TII type stress-strain curves were plotted with suitable amount of enlargements. A few representative enlarged curves are shown in Fig.3.23 and Fig.3.24 for longitudinal and transverse specimens respectively. The observed serrations in such curves were compared with different types of serrations reported in literature, as shown schematically in Fig.3.25. The schematic diagram in Fig.3.25 describes the nature of A, B, C, D and E types suggested by various other investigators [62-66]. Type A, B and C serrations have been discussed by Russel [62], Solar et al. [63], Cuddly et al [64]; whereas type D and

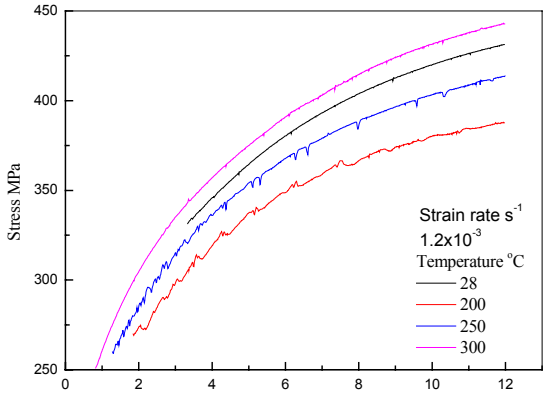

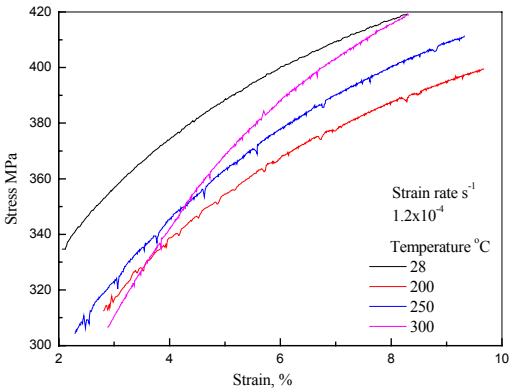

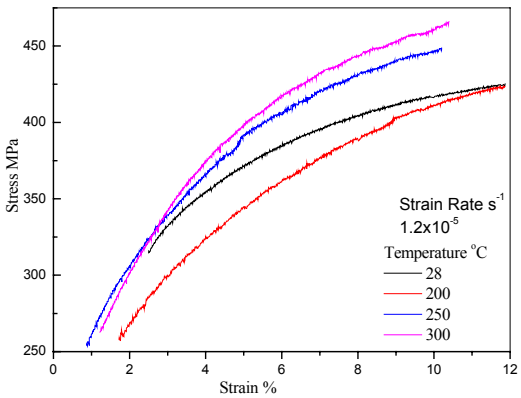

Fig.3.23 Serrations observed in the pre necking region of engineering stress-strain curves for the longitudinal specimens

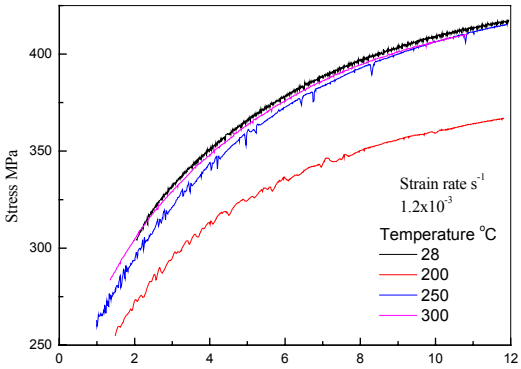

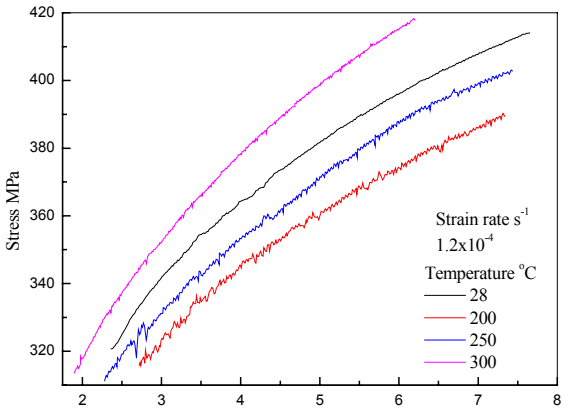

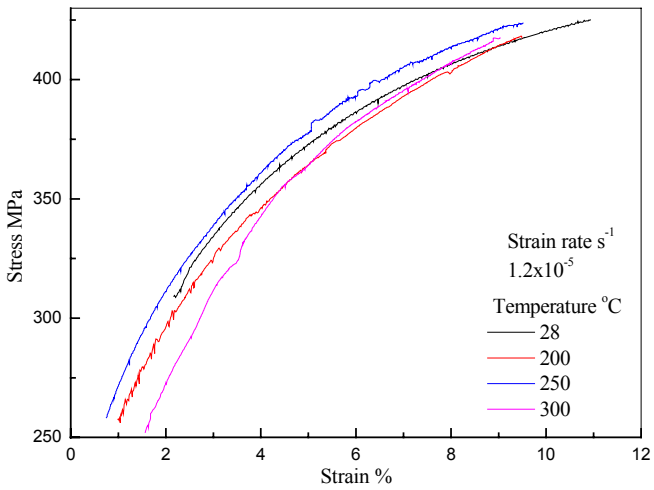

Fig.3.24 Serrations observed in the pre necking region of engineering stress-strain curves for the transverse specimens

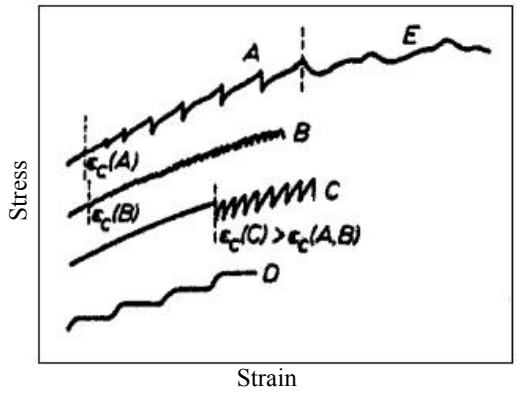

Fig.3.25 Schematic representation of five types of serrations reported in literature.

E serrations are found referred in reports by Pink et al. [65] and Wijler et al. [66]. The occurrence of different types of serrations is dependent upon the material and the test variables like temperature and strain rate.

It was noted that both longitudinal and transverse specimens commonly exhibit mixed A and B type serrations in the test conditions of the present experiments. However, type C serrations were recorded for the longitudinal specimens tested at the lowest strain rate of $1.2x10^{-5}$ s^{-1} at all elevated temperature tests. The exception from the common trend was noted at 250^{o}C for the strain rate of $1.2x10^{-5}s^{-1}$ for transverse specimens; in the stress-strain curve of this specimen, the serration could be possibly classified as mixed A and E type. However, serrations were not observed in longitudinal or transverse specimens tested at room temperature. The serrations recorded in all the investigated stress-strain curves have been compiled in Fig.3.26 and Fig.3.27 respectively for longitudinal and transverse specimens. The observation of the mixed type A and type B serrations during the tensile tests conducted at the strain rates of $1.2x10^{-3}$ and $1.2x10^{-4}s^{-1}$ and temperature range of 200-300^{o}C, indicates the occurrence of discontinuous slip band propagation across the gauge length of the specimen [39]. The nature of the type C serrations observed in longitudinal specimens at the slowest strain rate of $1.2x10^{-5}$ s^{-1} is in agreement with the observations of some earlier investigators [39,64,65].

Type A serration is produced due to the formation and propagation of deformation bands across the gauge length of a specimen. It usually starts at one end of the specimen and propagates along the same direction across its gauge length [39,66,78]. These are known as locking serrations. These show an abrupt rise followed by a drop in stress from the general level of the stress-strain curve. These occur usually in the lower temperature region. Type B serration is oscillation type of serration. It occurs in quick succession due to discontinuous band propagation arising from the moving dislocations within the band. Type B serration are usually found accompanied by type A or type D. Type C serration is yield drops that occur below the general level of the flow curve. These are due to dislocation unlocking. This type of serration originates at lower strain rates in comparison to type A and type B serrations. Type E serrations appear at higher strains when the engineering stress-strain curves approach the ultimate tensile strength of the material. Type A serrations generally

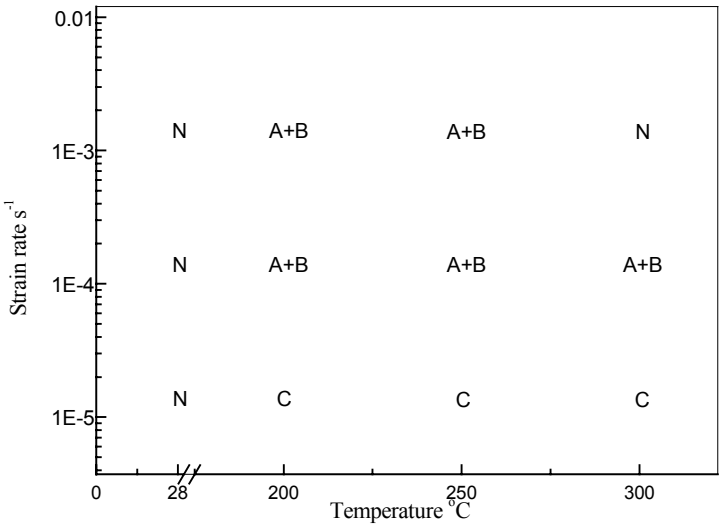

Fig.3.26 A map showing the types of serration observed for the longitudinal specimens at different test conditions.

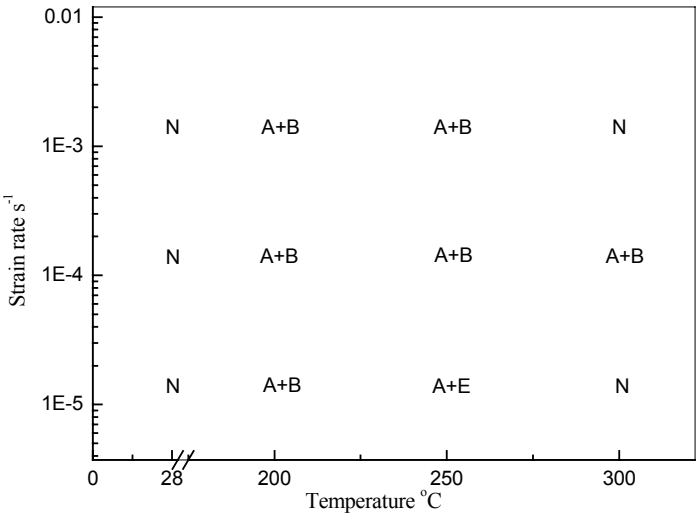

Fig.3.27 A map showing the types of serration observed for the transverse specimens at different test conditions.

change over to type E serration. The deformation band propagates with little or no work hardening.

3.3.4. Effect of Strain Rate Change on DSA

The discussion in the previous sections lead to infer that the steel under investigation exhibits DSA in the temperature range of 200 to 300^{o}C. Rodriguez [39] has indicated that the DSA behaviour in a material should be accompanied with negative strain rate sensitivity. In order to confirm this phenomenon some additional experiments were carried out to study the tensile flow behaviour of the material using strain rate changes. The schematic plan of the test is portrayed in Fig.3.28. Three tensile tests have been carried out with changing strain rates during deformation. These are: (a) a test on a longitudinal specimen at ambient temperature of 28^{o}C, (b) a test on a longitudinal specimen at 250^{o}C and (c) a test on a transverse specimen at 200^{o}C. In all these tests the specimen was loaded at an initial strain rate of $1.2x10^{-5}s^{-1}$, which, was changed to $1.2x10^{-3}s^{-1}$ at 5% strain. Subsequently without unloading the specimen, the strain rates were alternated between slow ($1.2x10^{-5}s^{-1}$) and fast ($1.2x10^{-3}s^{-1}$) rates at 5% strain interval. The results of the above three tests are shown in Fig.3.29, Fig.3.30 and Fig.3.31, in which the points at which strain rate alterations were done are marked as X_1, X_2, X_3 and X_4.

In general when the strain rate changes from a slower to a higher value during tensile deformation of a material the flow curve shifts upwards [67,68], causing an instantaneous increase in stress. This is observed at point X_1 in Fig.3.29. Such an increase in flow stress is associated with positive strain rate sensitivity. Similarly if the strain rate is changed from a faster to a slower value, a drop in the flow stress occurs, as illustrated at point X_2 in Fig.3.29. This is also associated with positive strain rate sensitivity. The changes in flow stress at points X_3 and point X_4, for the room temperature test (Fig.3.29) are also in accordance with the observations made at the points X_1 and X_2. Thus it can be said that the longitudinal specimen, when, loaded in tension at 28^{o}C show a positive strain rate sensitivity through out the test.

An examination of the influence of strain rate changes at the points X_1, X_2, X_3 and X_4 in Fig.3.30 and Fig.3.31 reveals negative strain rate sensitivity. It may be observed that: (a) when the strain rate is changed from a slower to a faster rate, the stress drops and (b) when the strain rate is changed from a faster to a slower value, the

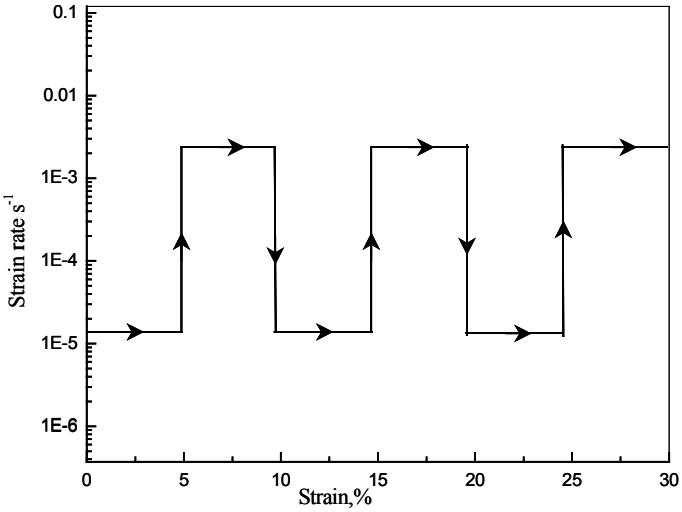

Fig.3.28 Schematic plan of strain rate change tensile tests

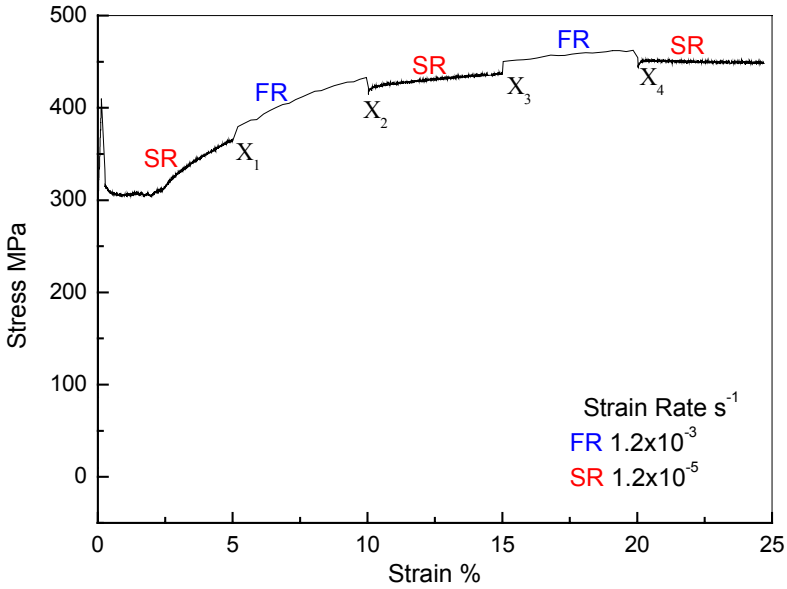

Fig.3.29 Engineering stress-strain plot of strain rate change test for the longitudinal specimen at 28°C.

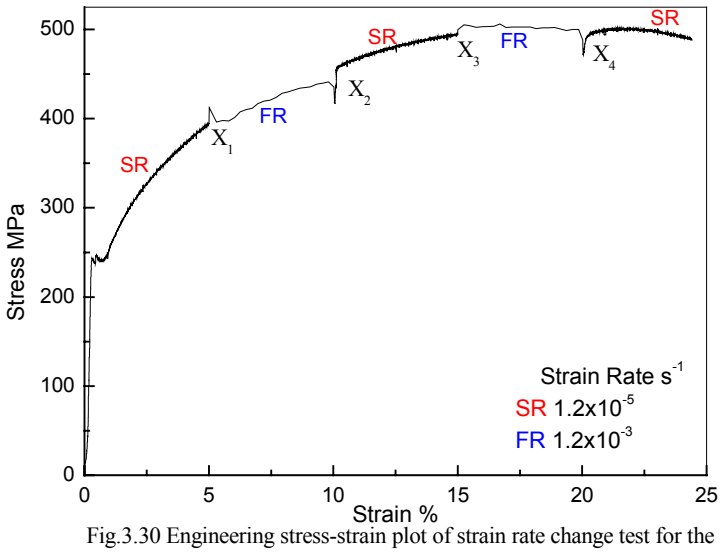

Fig.3.30 Engineering stress-strain plot of strain rate change test for the longitudinal specimen at 250°C.

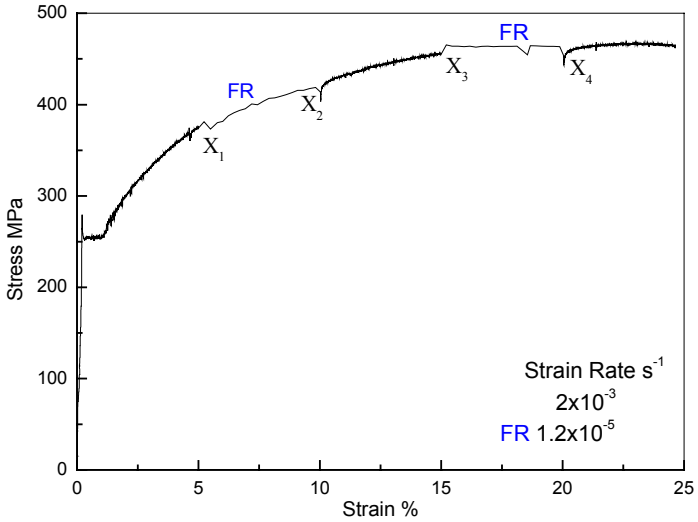

Fig.3.31 Engineering stress-strain plot of strain rate change test for the transverse specimen at 200°C.

flow stress increases or at times does not alter significantly. All these phenomena are associated with either negative strain rate sensitivity or strain rate sensitivity approaching zero. Thus the tensile behaviour of the longitudinal and the transverse specimens tested at elevated temperatures under the influence of strain rate change is markedly different than that of the specimens tested at room temperature under similar conditions. It could, thus, be concluded that the investigated steel is not prone to DSA at room temperature unlike that at elevated temperatures as shown in Fig.3.13 and Fig.3.14. However, it can be noted from Table 3.6 and Fig.3.13 and Fig.3.14, that the lowest value of e_u is only 11% lower than its value at ambient temperature, in the case of specimen tested at 250^{o}C under strain rate of $1.2x10^{-4}$ s^{-1}. A detailed examination of the fracture surfaces, discussed in next section, also does not reveal any noticeable changes in the fracture morphology.

3.3.5. Study of Fracture Surfaces of The Tensile Tested Specimens

Typical representative fractographs of the broken tensile specimens tested at various temperatures for, both, the longitudinal and the transverse specimens are shown in Fig.3.32 and Fig.3.33 respectively. The fractographs in Fig.3.32 and Fig.3.33 indicate that the dimple sizes are slightly smaller in the case of transverse specimens. A possible reason for this could be an influence of the banding direction on the formation of dimples. In the case of longitudinal specimens the tensile loading direction is parallel to the bands whereas in the transverse specimens loading direction is at an angle to the bands.

The features of the fracture surfaces of the longitudinal specimens tested at room and at elevated temperatures do not show any significant difference. The fractographs in Fig.3.32 also depict that morphology of the dimples on the fracture surfaces of longitudinal specimens is not influenced by test temperature. It can only be postulated that initiation of the dimples in these specimens may occur at different strains, but the subsequent growth of the voids require almost equal strains. Similar fractographic features were also observed on the broken surfaces of transverse specimens tested at different temperatures as shown in Fig.3.33. The fractographs shown in Fig.3.32 and Fig.3.33 correspond to tensile specimens tested using the nominal strain rate of $1.2x10^{-4}$ s^{-1}. The fracture-features of specimens tested at the other two strain rates ($1.2x10^{-3}$ and $1.2x10^{-5}s^{-1}$) were also similar to that exhibited by

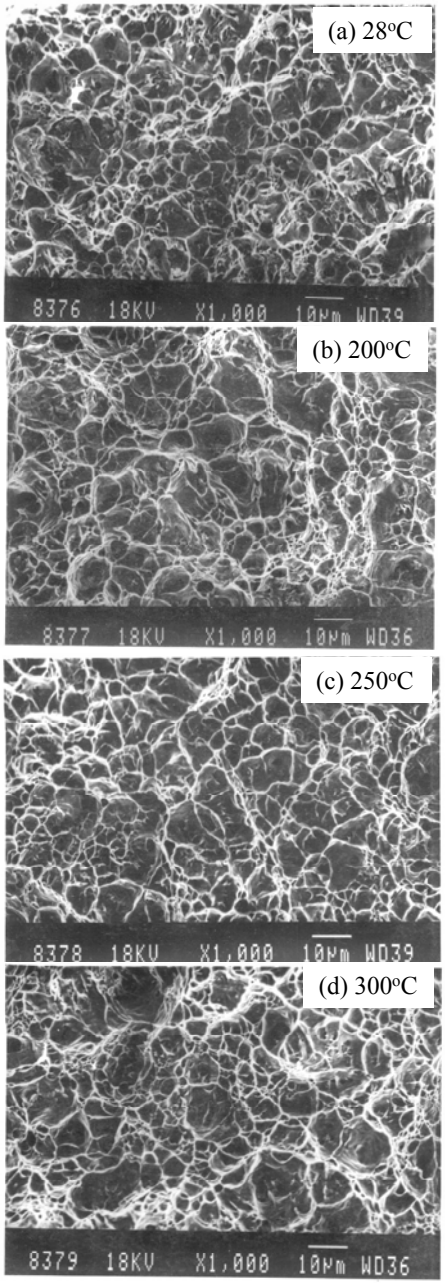

Fig.3.32 Typical representative fractographs of the longitudinal specimen tested at the strain rate 1.2×10^{-4} sec^{-1} at (a) 28°C, (b) 200°C, (c)250°C and (d) 300°C.

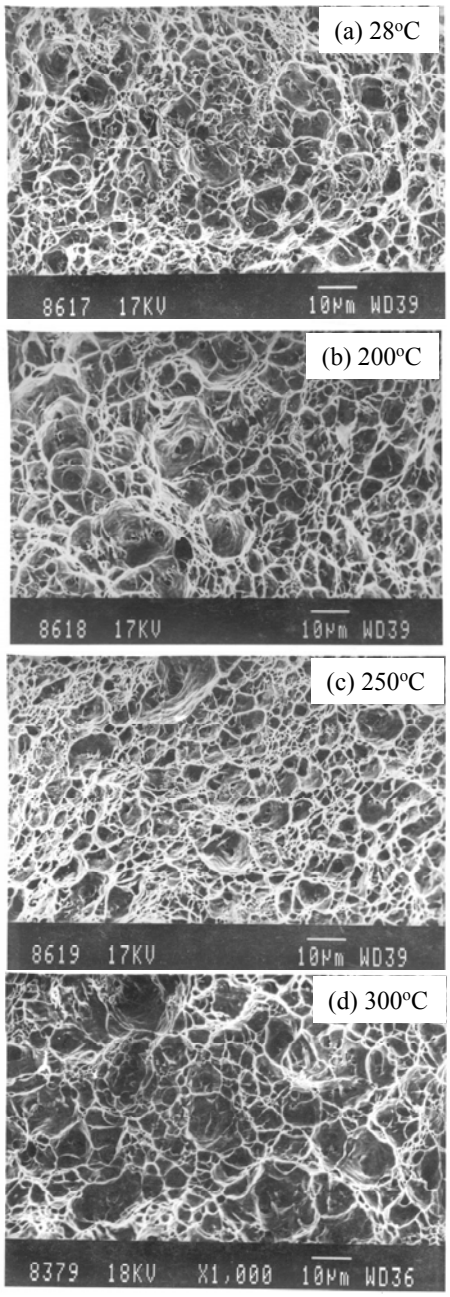

Fig.3.33 Typical representative fractographs of the transverse specimens tested at the strain rate 1.2×10^{-4} sec^{-1} at (a) 28°C, (b) 200°C,(c) 250°C and (d) 300°C.

Fig.3.32 and Fig.3.33. It may be inferred that through DSA affects the tensile properties of the steel its influence on the mechanism of crack propagation is not detectable by qualitative fractography.

3.4. CONCLUSIONS

The following major conclusions can be drawn from the investigations carried out in this chapter.

1. The chemical analysis of the investigated steel confirms that it belongs to be ASME SA 333 Gr 6 variety. Metallographic examinations revealed the steel to contain low amount of inclusions but presence of several elongated MnS are detected along the length of the pipe. The microstructure of the steel exhibits ferrite and pearlite, having good degree of banding. The average banding index is found to be 0.468 and 0.358 for the longitudinal and the transverse specimens respectively. The mean ferrite grain size of the steel is 14.4±1.2μm.

2. The yield strength, tensile strength and percentage elongation of the material are in accordance with the requirements of ASME SA 333 Gr 6 steel.

3. The steel exhibits dynamic strain aging in the temperature range of 200 to 300^{o}C and within the strain rate ranges of $1.2x10^{-3}$ to $1.2x10^{-5}s^{-1}$. The occurrence of dynamic strain aging is found to be associated with increase in tensile strength and decrease in ductility.

4. Strain rate change tests show that room temperature tensile flow is associated with positive strain rate sensitivity, whereas, such flow at elevated temperature is associated with either zero or negative strain rate sensitivity.

5. The serrations in the heterogeneous regime of the tensile flow curves were usually found to be as a mixture of type A plus type B.

4.0 MONOTONIC FRACTURE BEHAVIOUR OF THE STEEL

4.1. INTRODUCTION

The integrity of the primary heat transfer piping system of nuclear power plants in which the selected steel is used is commonly assessed using Leak Before Break (LBB) concepts. The LBB approach using fracture mechanics principles attempts to ensure that no catastrophic rupture would occur in an engineering component without prior indication of detectable leakage. In order to encompass fracture mechanics principles in such component integrity program one requires information and understanding about the fracture behaviour of a material in different experimental conditions. This chapter deals with studies related to crack initiation toughness of the SA 333 steel in monotonic loading condition.

The plane strain fracture toughness K_{IC}, cannot be used for characterizing the fracture toughness of the selected low carbon steel having moderate strength and good ductility, because the maximum thickness of the CT specimens that can be fabricated from the available form is only 25mm. A rough estimate reveals that the thickness requirement would be around 45mm. For characterizing the steel thus one has to estimate its fracture toughness criteria using the approach of elastic plastic fracture mechanics such as *J*-integral or *CTOD* [68,79]. The *J*-integral fracture criterion is currently popular and is used for the LBB analysis of the piping systems. Hence in the present investigation, attempts have been directed to study the fracture behaviour of the steel using *J*-integral analysis.

The steel SA 333 is usually exposed to a temperature range of 28 to 300^{o}C in its service life. It has been already discussed in the previous chapter that the steel has a tendency to exhibit dynamic strain ageing (DSA) in the temperature range of 200-300^{o}C. The occurrence of DSA is known to degrade fracture initiation toughness and the resistance to crack propagation in several materials [3-5,7,37,42-44,46,47,49,50]. The only exception to this trend has been observed by Srinivas et al. for Armco iron [48]. The experimental evidences gathered by the previous investigators indicate that low carbon steels, which are susceptible to DSA, exhibit increased strength and decreased fracture resistance in the temperature range where DSA is operative, in

comparison to their corresponding values at room temperature. Thus it is considered in this investigation that the fracture toughness value of the selected SA 333 steel needs to be systematically examined in its service temperature range of 200-300^{o}C. Additionally, since the steel shows banding, it is important to generate information related to the effect of specimen-orientation on *J*-integral based fracture criteria.

The objectives in this part of investigation are thus: (i) to determine the fracture toughness of the selected steel using *J*-integral analysis, (ii) to examine the effect of specimen orientation on the fracture behaviour of the steel and (iii) to understand the fracture behaviour of the steel at elevated temperature *vis-a-vis* that at ambient temperature.

4.2. EXPERIMENTAL

4.2.1. Specimen Preparation

The fracture toughness tests in this investigation were planned on compact tension specimens on two different orientations. Considering the available form of the material, standard 1CT specimens were machined following the guidelines of ASTM E 399-90 [55], in two orientations, LC and CL of the crack plane. Typical configuration of a specimen is shown in Fig.4.1 and the positions of the specimen blanks for the preparation of the two types of specimens has already been shown in Fig.3.3. The designed dimensions of the specimens were; thickness (B) = 25mm, width (W) = 50mm and machine notch length (a_N) = 15mm. The dimensions of the specimens used in this investigation are shown in Table 4.1.

Fatigue pre-cracking of the CT specimens was carried out at room temperature in decreasing ΔK mode as described in ASTM standard E 647 [80] using a commercial software (Advanced Fatigue Crack Propagation, AFCP) supplied by INSTRON Ltd U.K. The crack lengths were measured by compliance technique using a COD gauge fitted on the load line of the specimen. The software permitted on-line monitoring of the crack length (a), stress intensity factor range (ΔK) and the crack growth rate per cycle, da/dN. All pre-cracking experiments were carried out at a stress ratio of R = 0.1 using a frequency of 15Hz and with a starting ΔK between 25 and 28MPa$\sqrt{m}$. The magnitude of ΔK was decreased as per the expression $\Delta K=\Delta K_o \exp\{c(a-a_o)\}$, where the

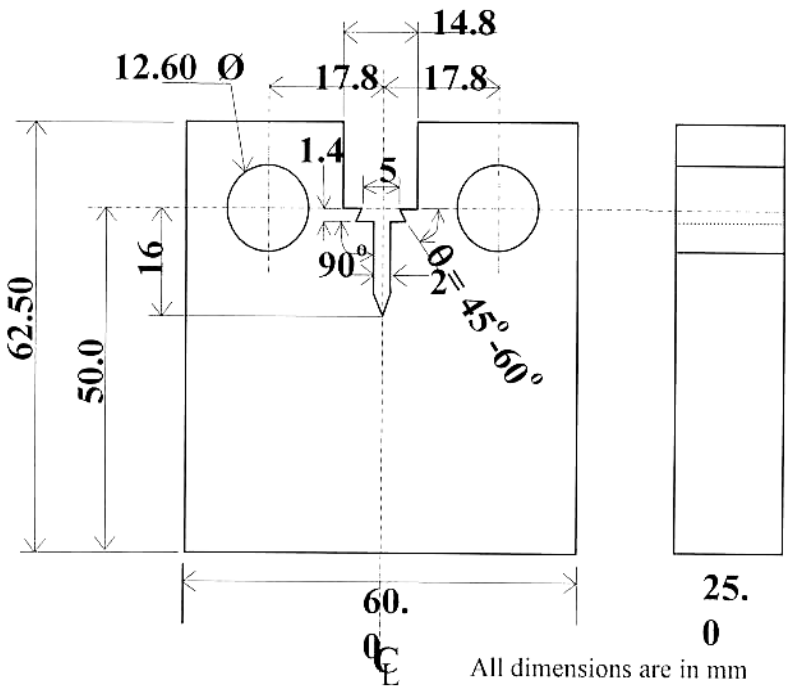

Fig.4.1. Nominal dimensions of the 1"CT specimens

value of 'c′ was taken as -0.08. All specimens were pre-cracked to achieve a total crack length of approximately 25mm, which corresponds to $a/W \approx 0.5$. The magnitude of ΔK achieved at the end of precracking was kept between 16~18 MPa√m in all the specimens. A typical plot of ΔK vs. crack length as obtained during the fatigue pre-cracking experiments is shown in Fig.4.2. The total crack lengths a_o (including fatigue pre-crack) and the terminal ΔK value at the end of pre-cracking for each specimen are given in Table 4.1. The pre-cracked specimens were provided with a side groove of 20% of the specimen-thickness. The side grooving was carried out by keeping a notch angle of 60^o to a depth of approximately 2.5mm on each side of the specimen. This was done to enhance the stress tri-axialty at the crack tip and to enhance confidence level in the post–test measurement of Δa by optical means. The net thickness (B_N) of all the specimens is also shown in Table 4.1.

Table 4.1. Details of the tested specimens dimensions

Sl. No	Specimen Code	Specimen Dimensions			a_o (mm)	$\Delta K^{\#}$ (MPa√m)	B_N (mm)
		W (mm)	B (mm)	a_N (mm)			
1.	LC1	49.84	25.00	15.8	25.16	16.62	19.60
2	LC2	50.22	25.00	15.5	25.11	16.51	19.98
3.	LC3	50.18	25.02	16.4	25.01	16.25	20.08
4.	LC4	50.16	25.04	15.6	25.08	16.34	19.85
5.	CL1	50.18	25.04	16.5	25.10	16.68	19.82
6.	CL2	50.05	25.05	15.4	25.02	16.23	19.87
7.	CL3	50.01	24.94	15.4	24.96	16.07	19.85
8.	CL4	50.13	25.03	15.8	25.06	16.15	19.80

$\Delta K^{\#} = \Delta K$ at the end of pre-cracking, W = width of the specimen,
B = total thickness of the specimen, B_N = net thickness of the specimen
a_N = machined notch length of the specimen, a_o = crack length after pre-cracking,

4.2.2. Fracture Toughness Testing

The estimation of *J*-integral values of the fabricated specimens was carried out using an INSTRON (model: 8562) machine as described earlier (§ section 3.2.6). The single specimen unloading compliance technique has been used for evaluation of *J*-integral fracture toughness. In this method the crack lengths are determined from elastic unloading compliance measurements. This is done by carrying out a series of

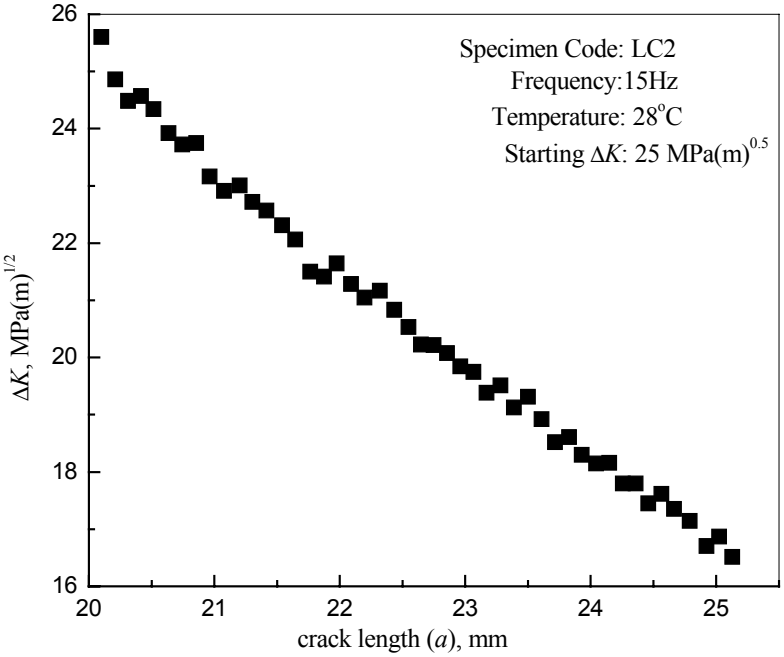

Fig.4.2 Typical plot of ΔK vs cracklength obtained during fatigue pre-cracking of specimen.

sequential unloading and reloading during the test, the interruptions being made in a manner that these are almost equally spaced along the load versus displacement record. These experiments have been carried out following the ASTM E 813 [81] standard; (its current designation is E-1820 [18])

In the single specimen *J*-integral tests unloading should not exceed more than 50% (§ 18) of the current load value and hence design and control of the test procedure is important. Some initial trial experiments indicated that a specific actuator displacement control for the selected steel could lead to the desired test procedure. This control consisted of loading a specimen to a level of 0.3mm, unloading through 0.15mm, reloading through 0.15mm and then repeating the sequence till an appreciable load drop was noticed on the load displacement plot. A schematic representation of the variation of displacement with time used for the present tests is shown in Fig.4.3. The displacement cycles were carried out using an actuator rate of 8.3×10^{-3} mm s^{-1}. The tests were controlled through a computer attached to the machine. The actuator displacement, load and the load line displacement (LLD), were recorded continuously through out the test at a frequency of 2Hz. The magnitude of LLD was monitored by a crack opening displacement (COD) gauge attached to the specimen. A minimum of approximately 35 data points of load-LLD was collected from the unloading part of the loading sequence for crack length calculations. A typical load displacement plot for a specimen tested at room temperature is shown in Fig.4.4.

The elevated temperature *J-R*- tests were carried out in an INSTRON split furnace. After mounting a CT specimen in its grips on the loading frame, the furnace was brought to position around the specimen, and was switched on. The loading on a specimen was started only after achieving the desired temperature and stabilizing it for 30 min. The temperature of the furnace was controlled by a three zone digital controller. A chromel-alumel thermocouple was tied on the specimen in a manner so that the temperature at the notch tip can be recorded. The temperature of the specimen during a test was monitored via this thermocouple. The *J-R* tests were carried out at three different temperatures 200, 250 and 300^{o}C in addition to the tests carried out at the ambient temperature of 28^{o}C.

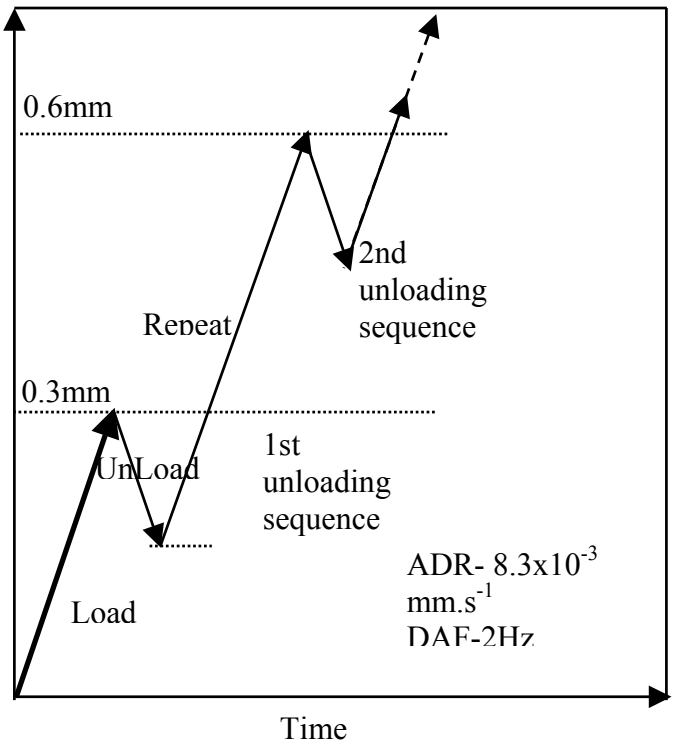

Fig.4.3. Schematic representation of the loading sequence for *J*-integral testing. The actuator displacement rate (ADR) and the data acquisition frequency (DAF) for these tests are also indicated.

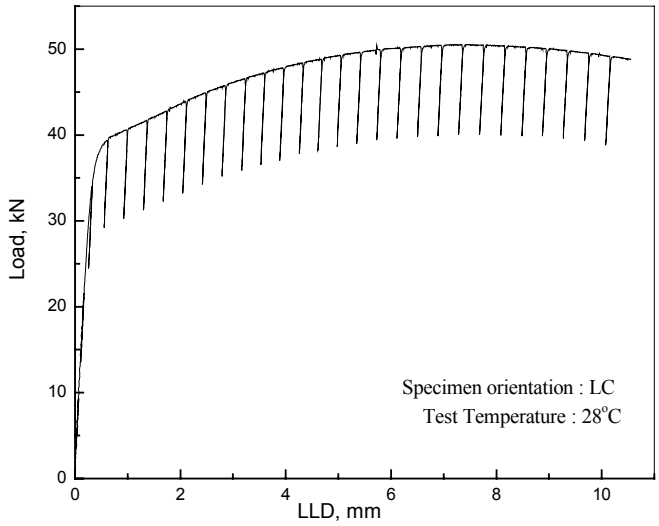

Fig.4.4 Typical load vs displacement plot at 28°C for LC specimen

Owing to the non-availability of a high temperature COD gauge of large travel the load line displacement (LLD) of the specimens (tested at elevated temperatures) were calculated from the actuator displacement data using a suitable calibration following the procedure suggested in ASTM E 1820 [18]. For the calibration a dummy specimen was loaded to 150% of the expected load on the test specimen. The recorded load-position data of the dummy specimen were subtracted from that of displacement of the actual specimen at the corresponding loads, to obtain the true load-load line data for the latter. It may be mentioned at this stage that the dummy specimen was fabricated from the same material with identical dimensions to those of the actual specimens with two specific differences. The dummy specimen was un-notched and was without any side grooving. The obtained displacement on the dummy specimen corresponds to the elastic compliance of the loading train and also accounts for the indentation of the loading pins on the specimen holes.

The method of obtaining load-LLD data is further illustrated using a schematic diagram in Fig.4.5. The load-displacement record of the dummy specimen is denoted here by the line OA and that for a test specimen is represented by the curve OBC. The displacement recorded in the curve OBC is due to that of the specimen as well as due to the loading train. The displacement values at each load on the curve OBC was reduced by the displacement for the corresponding load along OA to get the actual load line displacement of the specimen. The curve ODE represents the effective load-load line displacement of the test specimen. Using the above method of correction the experimental results of a specimen during a *J-R* test are shown in Fig.4.6. In this figure, both, the LLD measured employing a COD gauge and the actuator displacement corrected for LLD plots are exhibited. It may be seen that both the plots virtually lie over each other and hence one can analyse the load-displacement data for *J-R* curves of the selected material without introducing any appreciable error. In the present investigation all the elevated temperature test data were corrected prior to constructing the *J-R* curves.

The specimens, after the *J*-integral tests, were post fatigue cracked. The initial and the final crack lengths were measured as recommended in the ASTM standard [18] using a travelling microscope, and these values were then compared with the crack lengths estimated through unloading compliance technique. The magnitudes of the optically measured crack lengths were found to be within ±0.05mm of that

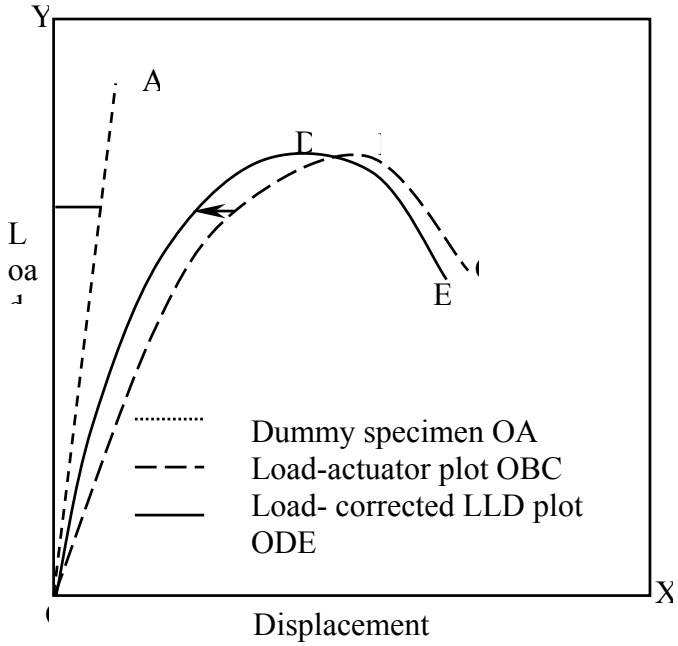

Fig.4.5. Schematic illustration of the method of correction of load-actuator displacement plot to get load-

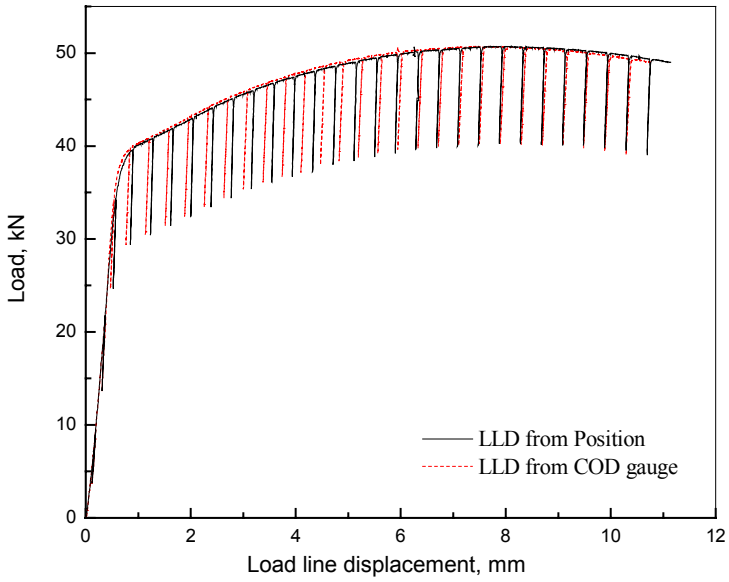

Fig.4.6 Comparision of load vs displacement plots from COD gauge at LLD and position data at 28°C.

calculated by compliance crack length (CCL) relation as discussed next. This procedure was followed for all the tested specimens.

4.2.3 Generation of *J-R* curve and evaluation of J_c

The experimental data obtained from the fracture toughness tests were analysed following the recommendations of ASTM standard E1820 [18]. The load *vs.* LLD data obtained from the tests were analysed to compute the magnitude of crack extension (Δa) and the corresponding *J* integral value at each unloading sequence.

The slope of each unloading path was calculated by linear regression analysis. The inverse of the slope yielded the compliance (C_i) of the specimen corresponding to the load from which the unloading has been carried out. The obtained C_i–values were corrected for the specimen rotation using the following expression to get the corrected compliance (C_{ci}) of the specimen at that particular load [18].

$$C_{ci} = \frac{C_i}{\left(\frac{H^*}{R}\sin\theta - \cos\theta\right)\left(\frac{D}{R}\sin\theta - \cos\theta\right)} \tag{4.1}$$

where H^* = initial half-span of the load points (centre of pin holes)

R = radius of rotation of the crack centre line, $(W+a)/2$

D = one half of the initial distance between the displacement measurement points

θ =angle of rotation of a rigid body element about the unbroken midsection line, or

$\theta = \sin^{-1}[(d_m/2+D)/(D^2+R^2)^{1/2}] - \tan^{-1}(D/R)$,

d_m=total measured load-line displacement.

The crack length (a_i) at this point of interest was next estimated using the expression suggested by Hudak et. al. [82].

$$\frac{a_i}{W} = 1.000196 - 4.06319U_x + 11.242U_x^2 - 106.043\,U_x^3 + 464.335U_x^4 - 650.677U_x^5 \tag{4.2}$$

where $$U_x = \frac{1}{(B_e E' C_{ci})^{½}+1} \tag{4.3}$$

B_e = Effective thickness of the specimen

$$= B - \left[\frac{(B-B_N)^2}{B}\right] \tag{4.4}$$

$$E' = \frac{E}{(1-\nu^2)} \tag{4.5}$$

W =width of the specimen

B = total thickness of the specimen

B_N = net thickness of the specimen

$$\Delta a = a_i - a_o$$

The magnitude of J is the sum of its elastic and plastic component denoted by J_e and J_{pl}. The elastic component of J was calculated using the equation:

$$J_e = \frac{K_i^2(1-\nu^2)}{E} \tag{4.6}$$

where K_i is the elastic stress intensity parameter evaluated using the expression given below [18]

$$K_i = \left[\frac{P_i}{(BB_N W)^{1/2}}\right] f\left(\frac{a_i}{W}\right) \tag{4.7}$$

where,

$$f\left(\frac{a_i}{W}\right) = \frac{\left((2+a_i/W)(0.886+4.64(a_i/W)-13.32(a_i/W)^2+14.72(a_i/W)^3-5.6(a_i/W)^4)\right)}{(1-a_i/W)^{3/2}} \tag{4.8}$$

The magnitude of J_{pl} was calculated by considering only load *vs* plastic load line displacement. In order to obtain the latter, the elastic part of displacement at different loads was first calculated from the slope of the initial load-LLD diagram. A simple subtraction of the elastic component from the total displacement yielded the plastic part of LLD. The area under the load *vs* plastic LLD data from the start of the test to the load of interest was calculated to obtain the magnitude of J_{pl}. This was done by using the expression [18]:

$$J_{pl(i)} = \left(J_{pl(i-1)} + \frac{\eta_{(i-1)}(A_{pl(i)}-A_{pl(i-1)})}{b_{(i-1)}B_N}\right)\left(1 - \frac{\gamma_{(i-1)}(a_i-a_{(i-1)})}{b_{(i-1)}}\right) \tag{4.9}$$

where $A_{pl(i)}-A_{pl(i-1)}$ = incremental plastic area

$$\eta_{(i-1)} = 2.0+0.522.b_{(i-1)}/W$$

$$\gamma_{(i-1)} = 1.0 + 0.76.b_{(i-1)}/W$$

The obtained values of J and the corresponding crack extension Δa were plotted to get the J- Δa curves of the material in various test conditions.

4.2.4 Fractography

The end of the ductile crack extension during loading of the specimens, subjected to J-integral test, was marked by post fatigue cracking, and then the specimens were loaded to fracture. The fractured surfaces were ultrasonically cleaned and examined using a scanning electron microscope. This was done to record the interesting features of stable crack extension as well as to understand the mode of failure.

4.3. RESULT AND DISCUSSION

In this section the procedure employed to evaluate the critical value of J is first presented. The estimated critical values of J are next discussed in two subsections elucidating the fracture behaviour of the material at ambient and at elevated temperatures. The effect of specimen orientation on the J-R curves is also discussed along with the effect of temperature on fracture behaviour of the investigated steel.

4.3.1 Determination of the Critical *J*-integral Fracture toughness

A typical J-R curve (a plot of J against Δa) for the specimen LC1 is shown in Fig.4.7. Initially attempts were made to evaluate tentative fracture toughness J_Q, value by conventional method, which consists of locating the intercept of a theoretical blunting line with the J-R curve. The equation of the blunting line as suggested in the ASTM standard E-813-89 is [81]:

$$J = m.\sigma_o.\Delta a \tag{4.12}$$

where, the value of m is taken as 2.

The parameter σ_o is the flow stress of the material at the test temperature and was taken as $(\sigma_{ys}+\sigma_{uts})/2$. The values of σ_{ys} and σ_{uts} have been already reported in Table 3.6. The values of σ_{ys} and σ_{uts} were taken from the results of tensile tests carried out at the actuator displacement rate $3x10^{-3}mms^{-1}$. The ASTM blunting line for the specimen LC1 was computed and is shown in Fig.4.7. However, this line (in Fig.4.7) does not intersect the experimental J-R curve. Similar observations were also made for

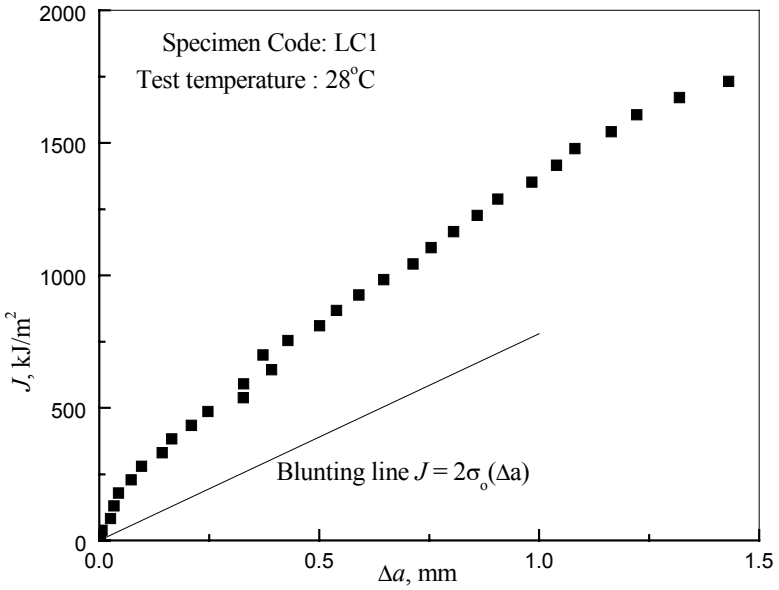

Fig.4.7 Typical *J-R* curve for a specimen having LC orientation

the other tested specimens as listed in Table 4.2. These observations are in following the results reported by several earlier investigators on high toughness materials [83-86]. In order to estimate the J_Q values, an experimental blunting line was then drawn considering the initial linear portion of *J vs.* Δa data for each of the specimens. The slopes of such blunting lines were estimated, and the values of *m* were calculated from the slope values using the corresponding value of σ_o.

A line parallel to the experimental blunting line at Δa = 0.2mm was next constructed. The intersection of this offset line with the fitted *J-R* curve was considered as the critical value of *J,* i.e. J_Q. In order to fit the power law equation for *J-R* curve, the experimental points of *J vs.* Δa lying between two exclusion lines were considered. The exclusion lines were constructed parallel to the experimental blunting line at Δa-offset values of 0.15 and 1.5mm following the ASTM standard E813. The experimental points between the two exclusion lines were then fitted to a power law equation of the form [81]:

$$J = C_1(\Delta a)^{C_2} \tag{4.13}$$

where C_1 and C_2 are material constants at the test conditions.

Two typical evaluations of J_Q for specimens having LC and CL orientations are shown in Fig.4.8(a) and Fig.4.8(b) respectively. Estimations of J_Q for the other specimens were also made in a similar manner. The results of C_1, C_2, J_{QC} and *m* are shown in Table 4.3. The estimated J_Q values were next examined for the validity of referring these as J_C/J_{IC} as per ASTM standard E813-89. The validity criterion states that the thickness (*B)* and the remaining ligament (b_o) of the specimen should be greater than $25(J_Q/\sigma_o)$. A typical calculation indicates the thickness requirement to be 43.3mm for the specimen LC1 considering J_Q = 674.5kJ/m^2 and σ_o = 389.5MPa. This thickness is more than the thickness of the tested specimen and even that of the available maximum thickness of the PHT pipe. Hence the evaluated J_Q value for this specimen cannot be referred as J_C/J_{IC} as per ASTM standard E813-89. Similar results (Table 4.4) were obtained when the J_Q values for the other specimens were subjected to the validity test. The wall thickness of the PHT pipe, thus, does not permit one to fabricate specimens for determining J_C/J_{IC} of the steel. For convenience, the J_Q values

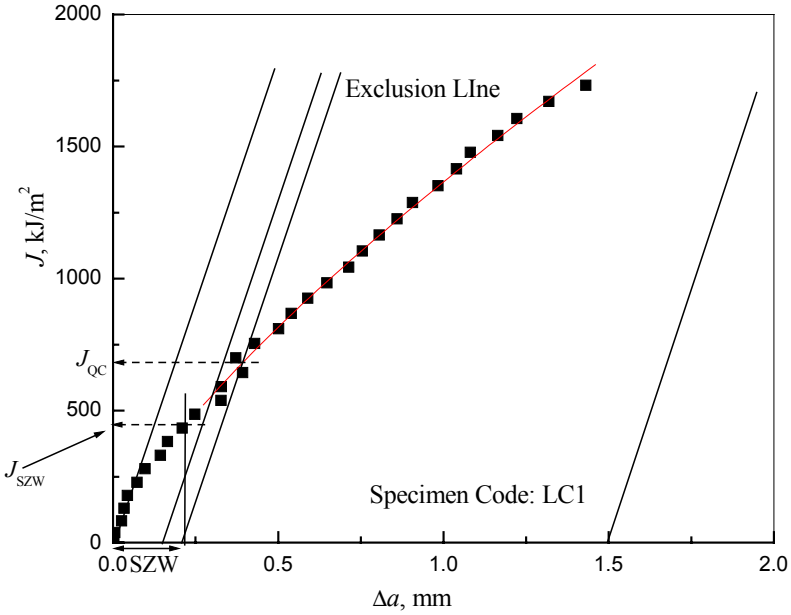

Fig.4.8(a) *J-R* curve of the material along LC orientaion at 28°C

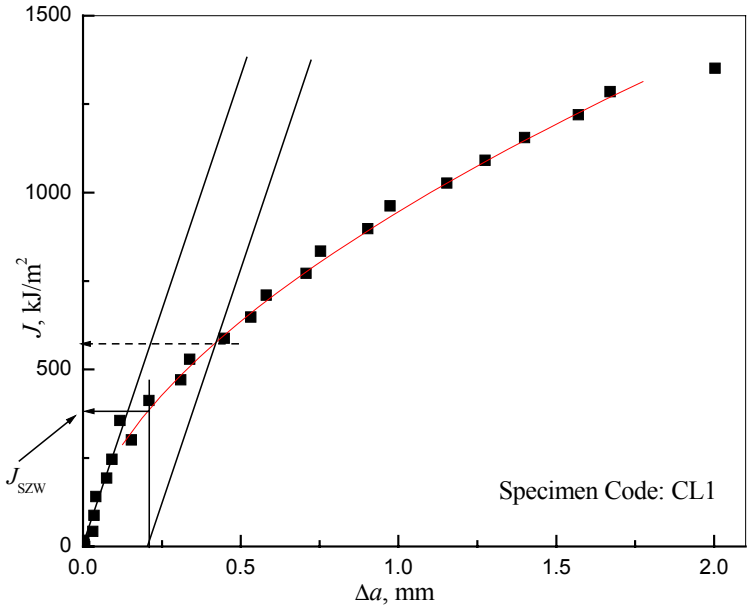

Fig.4.8(b) *J-R* curve of the material along CL orientaion at 28°C

estimated in this investigation are considered as the critical fracture toughness criterion of the material, and are denoted as J_{QC} in further discussion.

The crack growth resistance parameter dJ/da is the slope of the linear regression line of J and Δa data points. Here the data points lying between the crack extension of 0.2mm and 6.2 mm (i.e. 25% of the remaining ligament) has been considered for linear regression analysis as suggested by Newman et al. [87]. The magnitudes of dJ/da are also included in Table 4.3.

Table 4.3 Fracture toughness parameters of the investigated steel

Specimen code	Temp.^{o}C	C_1	C_2	J_{QC} kJ/m^2	m	dJ/da MJ/m^3
LC1	28	1351.5	0.758	674.5	9.73	1088.51
LC2	200	891.6	0.559	530.0	8.04	489.71
LC3	250	805.2	0.605	446.8	6.63	466.10
LC4	300	887.8	0.552	532.2	7.28	484.58
CL1	28	961.7	0.562	567.5	6.92	534.67
CL2	200	687.8	0.515	423.6	5.14	340.05
CL3	250	823.3	0.468	377.2	5.62	319.42
CL4	300	701.8	0.559	401.2	5.45	365.12

Table 4.4. Thickness validity criteria of the specimens for fracture toughness test

Specimen code	Temp.^{o}C	σ_o (MPa)	J_{QC} kJ/m^2	B (mm)	25(J_{QC}/σ_o)
LC1	28	389	674.5	25.00	43.3
LC2	200	358	530.0	25.00	37.1
LC3	250	341	446.8	25.02	32.8
LC4	300	354	532.2	25.04	37.6
CL1	28	390	567.5	25.04	36.4
CL2	200	343	423.6	25.05	30.9
CL3	250	332	377.2	24.94	28.4
CL4	300	342	401.2	25.03	29.3

σ_o = flow stress, J_{QC} = critical value of J,
B = specimen thickness, and 25(J_{QC}/σ_o) = thickness criterion.

4.3.2 *J* Integral Fracture Toughness at Room Temperature

The estimated *J*-integral fracture toughness values of the steel at room temperature are 674.5 and 567.5 kJ/m^2 (§ Table 4.3) for specimens with LC and CL orientations respectively. Singh et al. [5] and Marshall et al. [88] have earlier studied *J* resistance of similar materials. The obtained values of J_{QC} are found to be in excellent agreement with the values reported by Singh et al., but are significantly higher than those reported by Marschall et al. The latter investigators [88] have reported an average value of fracture initiation toughness for 1T CT specimens of SA 333 Gr. 6 steel as 325 kJ/m^2. The determination of J_{QC} by Singh et al. and by the present author is based on unloading compliance method to obtain *J-R* curve, whereas fracture initiation toughness by Marschall et al. [88] has been detected by Direct Current Potential Difference (DCPD) method. In the DCPD technique fracture initiation toughness is determined from the point of deviation of an initial linear region of a plot between electric potential *vs.* displacement (Fig.4.9). The displacement value at the point of deviation (as marked in Fig.4.9) is next used to obtain the corresponding load, from which the magnitude of J_i is calculated. It can thus be inferred that the difference in the reported [88] values of J_i and the present estimated J_{QC} is due to the different types of measurement, apart from the possibility of minor variations in the material characteristics used in these investigations.

In order to understand the difference in the values of J_{QC} obtained in this investigation and that by Marschall et al. [88], the fracture surfaces of the specimen LC1 were observed in SEM. A typical representative photograph of the initial region of the ductile crack extension is shown in Fig.4.10. The fatigue pre-cracked region is found to be followed by an expanse of stretch zone (SZ), which in turn is followed by ridges of ductile crack extension. But another dark region depicting the characteristics of stretch zone is found to follow the ductile crack extension (Fig.4.10). The observed nature of the stretch zone is thus of unusual type, and it is difficult to unambiguously estimate the width of the stretch zone and further stable crack initiation toughness.

The width of a stretch zone (SZW) gives indication about the fracture initiation toughness of a material [84-86,89,90]. An attempt was made to evaluate the SZW of LC1 and CL1 specimens. Measurements were done on a series of fractographs representing almost the entire stretch zone region across the specimen thickness considering (i) the first expanse of stretching as well as (ii) the entire region of the SZ incorporating the inter-laid ridges of ductile crack extension. If only the first expanse

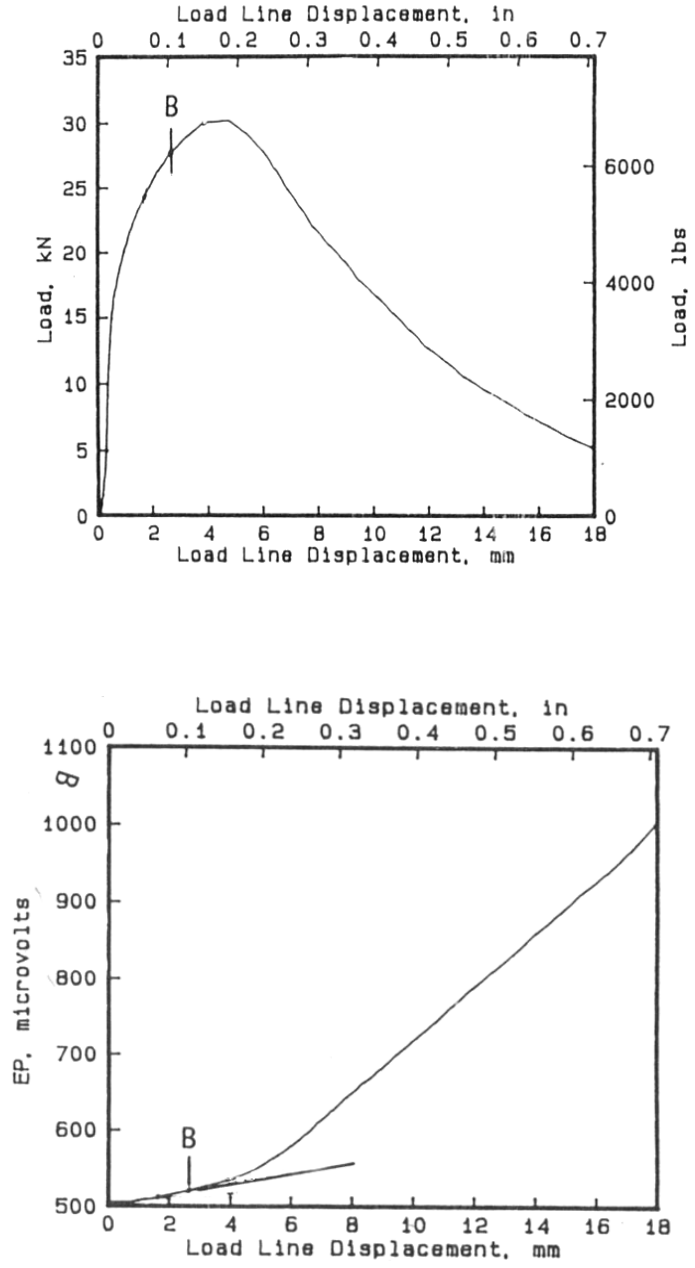

Fig.4.9 Load vs.displacement and vs. d-c electric potential data for SA 333 Gr 6 steel to illustrate determination of crack initiation at point B [88].

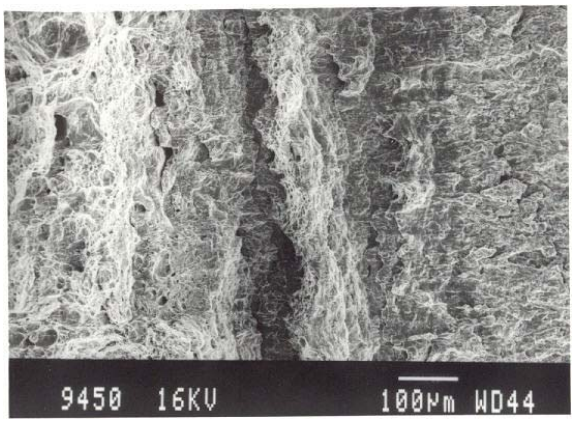

Fig.4.10 Typical SEM fractograph showing alternation stretch and void coalescence ahead of the fatigue pre-crack.

of stretching was considered, the average value of SZW comes out to be 219±27 μm; but if the entire dark region including the ridges of ductile crack extension is considered its value comes out to be 410±18 μm for LC specimen. Thus the SZW is not uniform and its variation could be of the order of 10-20%. The average value of SZW comes out to be 213±27 μm for CL specimen.

Fracture initiation toughness can be evaluated from the *J-R* curve by vertical intercept at Δa = SZW on *J*-Δa plot as shown in Fig.4.8(a). The values of fracture initiation toughness (J_{SZW}) are found to be 441 and 696 kJ/m^2 for first and total expanse of SZW values of 219 and 410 μm respectively. The value of J_{SZW} for SZW = 219 μm is found to be higher than the value of J_i reported by Marschall et al. [88], whereas the value of J_{SZW} for SZW = 410 μm can be considered closer to the J_{QC} value evaluated in the present investigation. The difference in the values of fracture initiation toughness (J_i) and critical fracture toughness (J_{IC}) is schematically illustrated in Fig.4.11. The estimation of J_i reflects the start of physical crack extension and J_c or J_{IC} inherently allows for some physical crack growth. The present observation indicate that in the selected steel, measuring SZW for identifying critical *J* also yields an ambiguous value. The possibility is that J_i can be calculated either from the initial stretch of SZW or from the total magnitude of SZW intermixed with regions of ductile stretching. The former estimation leads to a value of J_i close to the magnitude predicted by DCPD technique [88]. On the other hand, the magnitude of J_i estimated using the total stretch of SZW is closer to the value of J_{QC}. Hence it can be inferred that DCPD technique yields fracture initiation toughness, which corresponds to the initial stretch zone whereas the estimated J_{QC} takes account of the complete stretch of SZW. The value of J_{SZW} for 213 μm SZW is 382 kJ/m^2 for CL specimen and is lower than the LC specimen.

The magnitudes of the crack growth resistance parameter i.e. d*J*/d*a* was evaluated from the slope of the linear regression analysis of data points lying between Δa = 0.2 and 6.2mm (i.e. 25% of the remaining ligament). In case of the LC specimen only 1.5mm crack growth could be recorded for the maximum available travel (10mm) of the employed COD gauge. In case of the CL specimen the crack extension was found to be 2.5mm for the same extent of the COD gauge. The values of d*J*/d*a* were found to be 1088.5 and 534.7 MJ/m^3 for LC and CL specimens respectively.

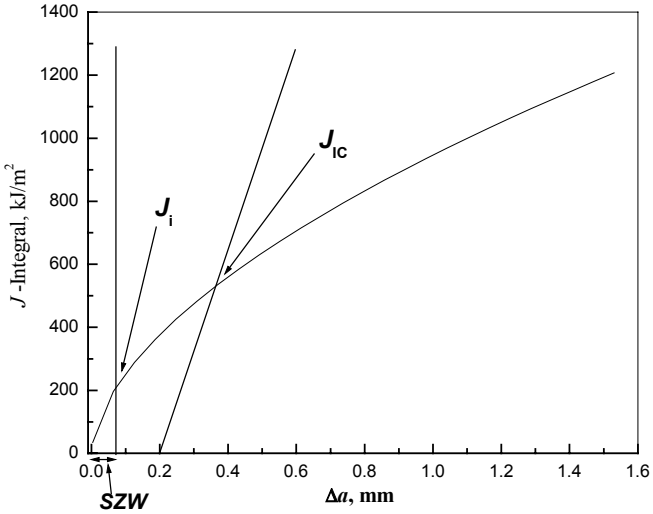

Fig.4.11 Schematic illustration of fracture initiation toughness from SZW and J_{IC} on *J-R* curve

A comparison of *J-R* curves at room temperature along two orientations is given in Fig.4.12.

The obtained results related to the fracture behaviour of LC and CL specimens (§ Table 4.3, Fig.4.12) indicate that fracture toughness (J_{QC}) and the crack growth resistance (d*J*/da) of the LC specimen are considerably higher than that of the CL specimen. The magnitude of J_{QC} for LC specimen is almost 20% higher than that of CL specimens and the value of d*J*/da for LC specimen is almost double than that of CL specimen. The difference in the fracture behaviour of the steel along LC and CL orientations can be attributed to the synergistic effect of the following

(a) The morphology of the inclusions along the crack propagation planes of LC and CL specimens is different. The inclusions were found elongated along the crack propagation plane of CL specimens unlike that in LC specimens. This has been illustrated earlier in Fig.3.6.

(b) The inclusions (Fig.3.5) were found to be in arrays at an angle to the pipe length axis.

(c) The microstructure of the steel was banded. The banding indices on the crack planes of LC and CL specimens are 0.358 and 0.468 (Table 3.3) respectively.

Marshall et al. [88] have reported that the morphology and preferred orientation of the inclusions on the crack plane of CL specimens facilitate nucleation and coalescence of voids during crack propagation. It is considered here that this micro mechanism of ductile fracture is operative here in addition to the fact that the process of initiation, growth and coalescence of voids also gets influenced by the banding index.

4.3.3 Fracture Toughness at Elevated Temperature

It has been mentioned earlier that the selected steel is commonly used in the temperature range of 200-300^{o}C. Hence the elevated temperature fracture behaviour of the steel was characterised at three temperatures, viz., 200, 250 and 300^{o}C pertaining to this temperature range. The *J-R* curves of specimens with LC and CL orientations at these temperatures are shown in Fig.4.13(a) and Fig.4.13(b) respectively. The room temperature *J-R* curves for these two orientations are also superimposed in these figures. The results in Fig.4.13(a) and Fig.4.13(b) indicate: (a) the estimated *J-R* curves at elevated temperatures lie below the one obtained at 28^{o}C, (b) up to about

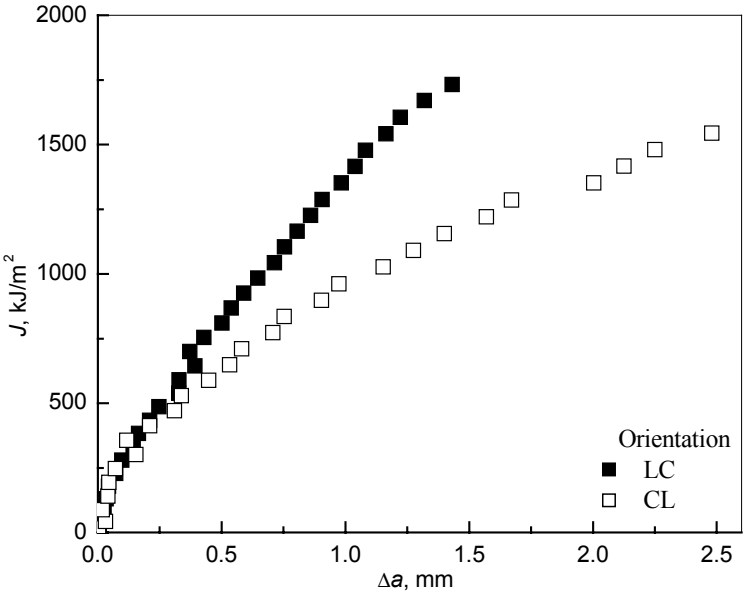

Fig.4.12 Comparison of *J* - *R* curves for specimens with LC and CL orientations at 28°C

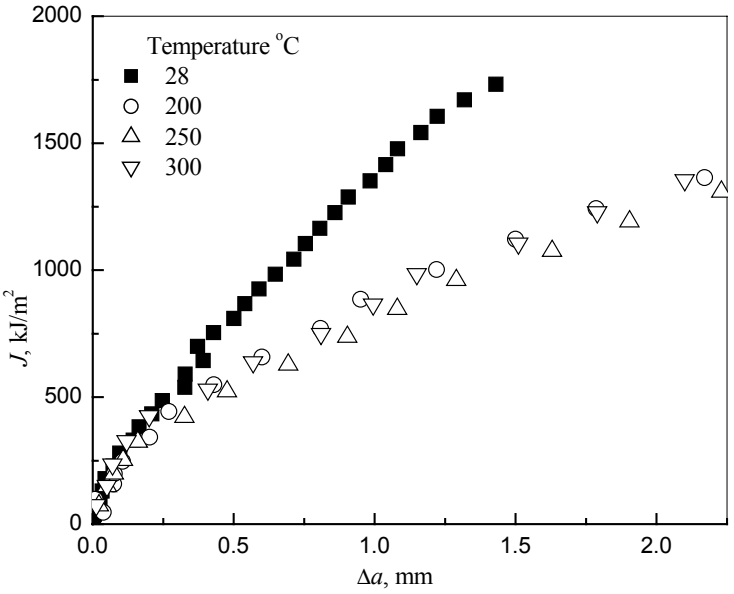

Fig.4.13(a) Effect of temperature on *J* - *R* curves for specimens with LC orientation

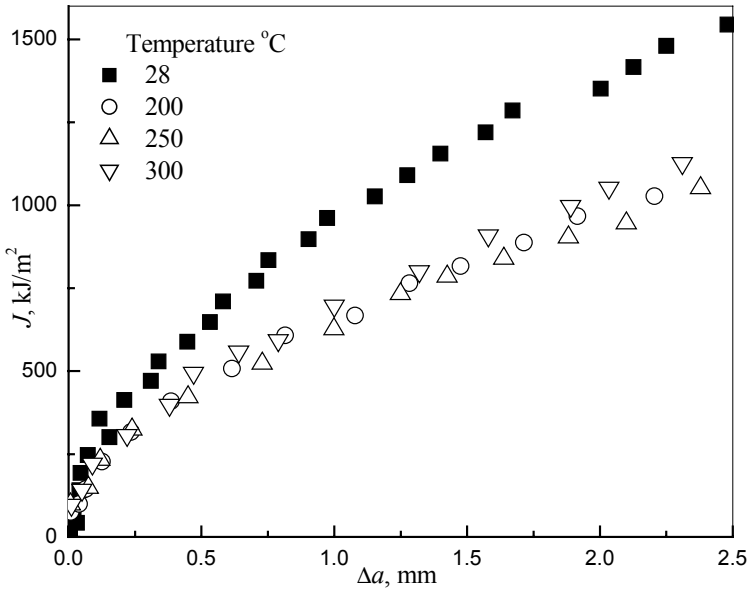

Fig.4.13(b) Effect of temperature on *J* - *R* curves for specimens with CL orientation

0.2mm of crack extension, elevated temperature *J-R* curves are almost identical, (c) for Δa >0.2 mm, the *J-R* curve at 250^{o}C is inferior amongst all the estimated *J-R* curves for both specimens with LC and CL orientations. The magnitudes of fracture toughness parameters J_{QC}, m and dJ/da for all the specimens tested at elevated temperatures have been estimated (§ section 4.3.1) and are shown earlier in Table 4.3.

In order to understand the influence of temperature on the fracture initiation toughness and the crack propagation resistance, the magnitudes of J_{QC} and dJ/da were plotted against the test temperatures. These plots are shown in Fig.4.14(a) and Fig.4.14(b). It may be observed from Fig.4.14(a) that J_{QC} decreases steeply with increase in test temperature up to 250^{o}C, beyond which it appears to increase. The results in Fig.4.14(a) also indicate that (a) fracture initiation toughness of CL specimens are lower at all test temperatures compared to that of LC specimens and (b) the decrease in fracture initiation toughness between 28 and 250^{o}C for both types of specimens are approximately 34%. (c) Between 250^{o}C and 300^{o}C, the increase in toughness is about 86 and 24kJ/m^2 for LC and CL specimens respectively.

The nature of variation of crack propagation resistance with temperature for both types of specimens are shown in Fig.4.14(b). Here also one finds that dJ/da sharply decreases from 28 to 200^{o}C and attains a minimum at 250^{o}C. But the variation of dJ/da between 200 to 300^{o}C is subtle in nature compared to the variation of J_{QC} in the identical temperature domain. It may be mentioned at this stage that the drop of dJ/da from 28 to 200^{o}C is 57% for LC specimen and 40% for CL specimens. Other researchers have also reported similar decrease in fracture resistance of the material due to dynamic strain aging as summarised in Table 2.3 [3,4,40-47]. Singh et al. [5] observed minor difference in *J-R* curves of SA 333 Gr 6 steel in the temperature range 28^{o} to 300^{o}C. Marschal et al. [6] have also reported drop in the *J-R* curve at 288^{o}C as compared to that of room temperature *J-R* curve for ASTM A 106 Grade B low carbon steel.

The nature of variation of J_{QC} with temperature was found to be analogous to the variation of percentage uniform elongation and percentage total elongation with temperature (§ Fig.3.12). The nature of variation of elongation of the steel with temperature has been attributed to dynamic strain aging; hence the specific variation of J_{QC} with temperature for this steel can also be attributed to the same phenomena. In

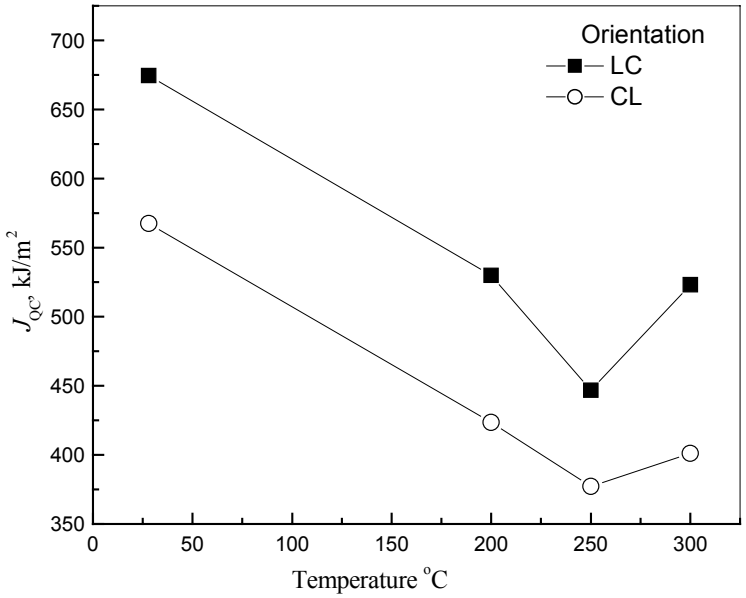

Fig.4.14(a) Variation of J_{QC} *vs* temperature along LC and CL orientations

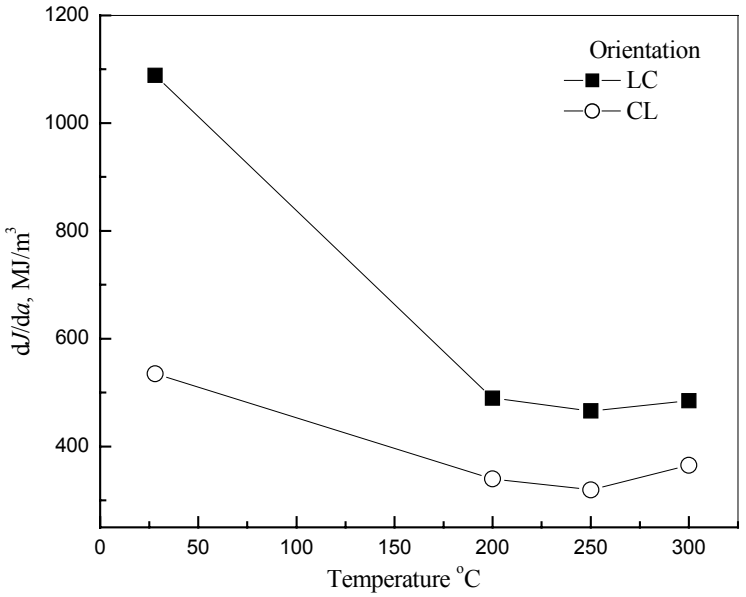

Fig.4.14(b) Variation of d*J*/d*a* *vs* temperature along LC and CL orientations

order to substantiate this fact, indirect estimates of fracture initiation toughness for this selected steel were made from the tensile properties and were compared with their experimental values. One can find several empirical expressions [91-97] relating fracture toughness and tensile properties of the materials. Amongst these the one suggested by Hahn and Rosenfield [91] and that by Sivaprasad et al. [97] are convenient to deal with. The expression suggested by Hahn and Rosenfield relates plain strain fracture toughness with tensile properties where as the relationship one suggested by Sivaprasad et al. is between *J* integral fracture toughness and tensile properties. The expression suggested by Sivaprasad et al. appears appropriate to evaluate indirect fracture toughness of the material from tensile properties.

The relationship between *J*-integral fracture toughness and tensile properties is [97]

$$J_{cal} = 2C\lambda(\varepsilon_u)^2\varepsilon_f\sigma_o \qquad (4.14)$$

where, C = a constant = 0.025m

λ = slope of *J*-δ curve

ε_u = True uniform elongation

ε_f = true fracture strain

σ_o = flow stress of the material.

The value of λ was obtained from the experimental *J*-δ curves for specimens tested at different temperatures. The tensile properties ε_u, ε_f and σ_o were taken from Table 3.6 The magnitude of σ_o was taken as $(\sigma_{ys+}\sigma_{uts})/2$. It may be mentioned at this stage that the tensile properties taken for these calculations correspond to the tensile tests carried out at the strain rate $1.2x10^{-4}s^{-1}$. Initial estimates of J_{cal} using equation (4.14) indicated a large difference between the calculated and the experimental values. This large difference was traced to the use of ε_f in equation (4.14). Hahn and Rosenfield have suggested "fracture strain" in such expressions be considered as $\varepsilon_f/3$. Replacing ε_f by $\varepsilon_f/3$ and computing J_{cal}, it was noted that the theoretical estimates are in reasonable agreement with the experimental values. A plot of J_{QC} against J_{cal} is presented in Fig.4.15. It is obvious from this figure that J_{QC} corresponds closely to the empirical estimates of J_{cal}. Hence it can be concluded that the phenomenon responsible to influence tensile properties at elevated temperature also influences the fracture

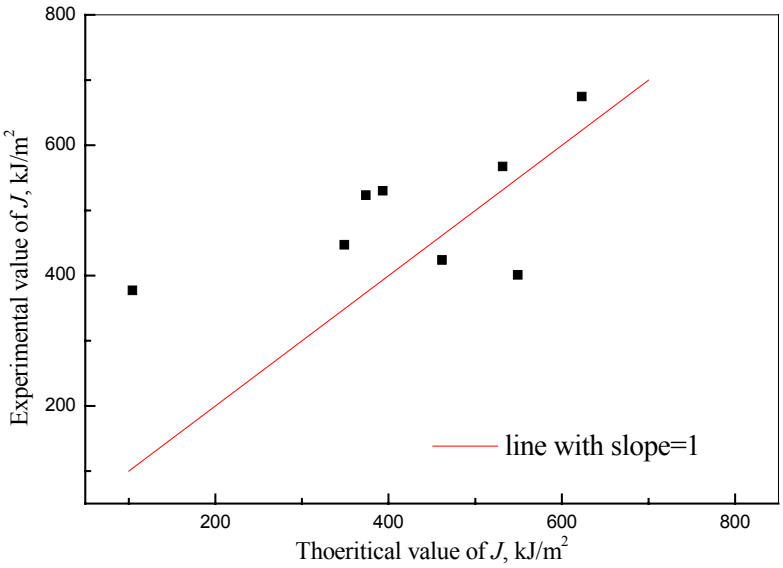

Fig.4.15. Plot showing corelation of J_{cal} value with the experimental J_{QC} value.

initiation toughness at elevated temperatures. Thus it can be inferred that the obtained variation of J_{QC} with temperature is due to dynamic strain aging.

The mechanism responsible for lower fracture initiation toughness at elevated temperatures was a priori searched for in terms of the nature of stretch zone. Clear demarcation of stretch zone in specimen tested at elevated temperatures was found to be difficult because of oxide layer. But some interrupted domains could be photographed. Two typical stretch zone configurations in LC specimen tested at 200 and 250^{o}C are shown in Fig.4.16 and Fig.4.17. A comparison of this stretch zone with the one observed in specimens tested at room temperature (Fig.4.10) indicates distinct difference. The expanse of stretch zone at elevated temperature is not interrupted by ridges of ductile crack extension unlike that has been observed for LC1 specimen tested at 28^{o}C (in Fig.4.10). It is thus considered that the absence of re-toughening of the crack tip, which increases the apparent toughness of the material at room temperature is the cause to reflect lower toughness at elevated temperatures. The DSA can be presumed to have altered the crack tip re-sharpening mechanism. However no correlation has been sought for between indirect estimates of J_{SZW} from stretch zone width and the magnitudes of J_{QC} for specimens tested at elevated temperatures because of the difficulty in reasonable estimation of SZW as discussed earlier.

The fracture surfaces of the specimens (both LC and CL type) tested at different temperatures were examined to assess the mechanism of crack propagation. Some typical fractographs are shown in Fig.4.18 and Fig.4.19 for specimens with LC and CL orientations. The crack propagation paths are typically marked with dimples indicating void initiation, coalescence and growth mechanism. Interestingly the dimple sizes on fracture surfaces of specimens broken at 250^{o}C were found to be smaller compared to those broken at 28^{o}C {Fig.4.19(b)}. This is indicative of the fact that crack propagation resistance of the material also gets influenced by dynamic strain aging phenomenon. This fractographic observation is in agreement with lower dJ/da of the specimens at elevated temperature.

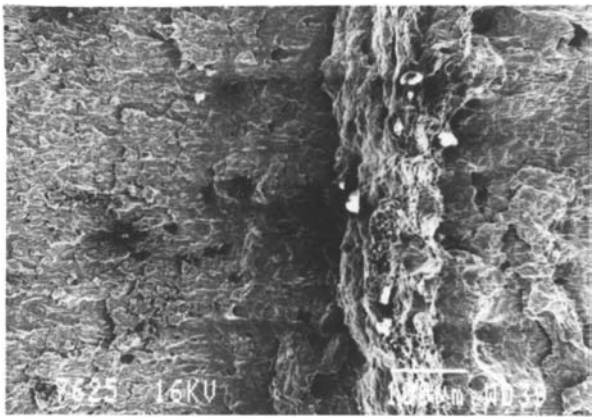

Fig.4.16. Typical SEM fractograph of SZW of *J* integral tested LC specimen at 200^{o}C.

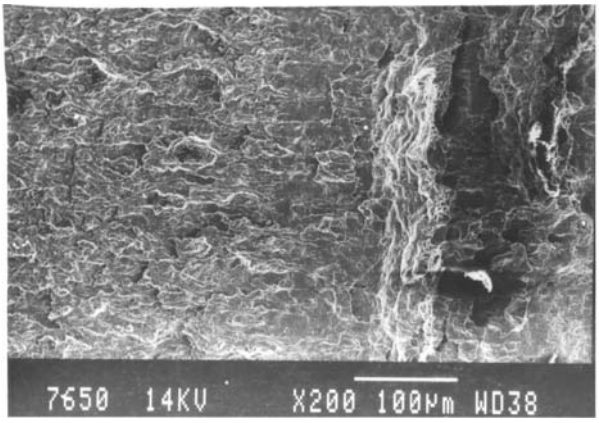

Fig.4.17. Typical SEM fractograph of SZW of *J* integral tested LC specimen at 250^{o}C.

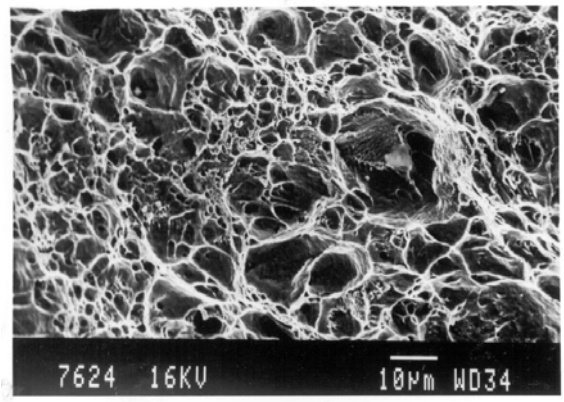

Fig.18(a) SEM fractograph of fractured surfaces of *J* integral tested LC specimen at 28^{o}C

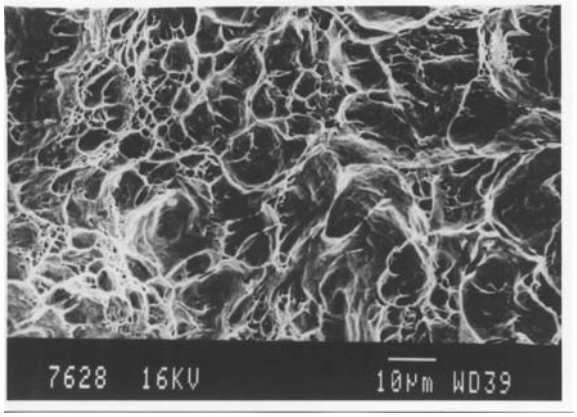

Fig.18(b) SEM fractograph of fractured surfaces of *J* integral tested LC specimen at 250^{o}C

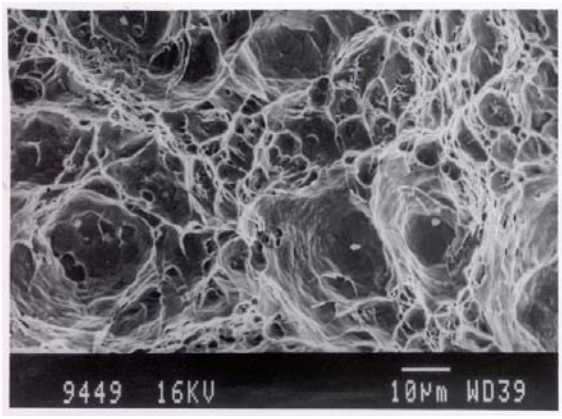

Fig.19(a) SEM fractograph of fractured surfaces of *J* integral tested CL specimen at 28^{o}C

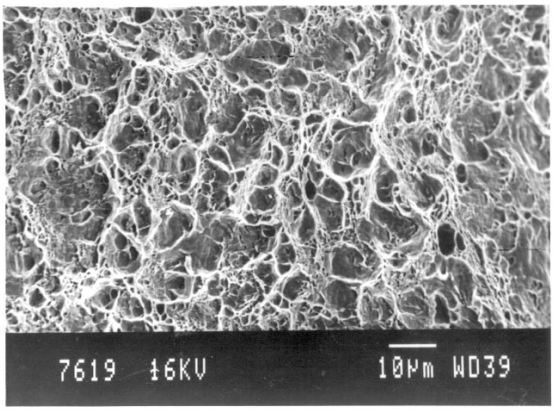

Fig.19(b) SEM fractograph of fractured surfaces of *J* integral tested CL specimen at 250^{o}C

4.4. CONCLUSIONS

The following major conclusions can be drawn from the investigations presented in this chapter.

1. The J_Q fracture toughness values of 1CT specimens prepared from the selected SA 333 Gr6 steel do not satisfy the validity criteria suggested in ASTM E-813 standard. Since one can at best fabricate 1CT specimens from the PHT piping, the J_{QC} (as defined here, equivalent to J_Q in standard) value has to be used for LBB analysis.

2. The characteristics of the stretch zone in the investigated steel are of unconventional type and is intermixed with ductile tearing. Its initial and total expanse can be used to estimate approximate values of J_i and J_{QC} respectively.

3. Alternate blunting and void growth at the crack tip provides higher resistance to crack propagation in the selected material in comparison to several commercial steels of similar carbon level.

4. The crack initiation and the crack propagation toughness of the steel are inferior in CL plane in comparison to that in LC plane because of the differences in the nature of inclusions and banding pattern in these planes.

5. The magnitudes of J_{QC} and dJ/da of the steel estimated in the temperature range of 200-300^oC are lower than those at room temperature for both LC and CL orientations of the specimen. This has been attributed to dynamic strain aging being operative in the above-stated temperature range.

5 THE EVALUATION OF CYCLIC *J-R* CURVES

5.1 INTRODUCTION

The general material characteristics and the dynamic strain aging behaviour of the selected SA 333 steel have been discussed in chapter 3. The results and discussion related to the study on monotonic fracture toughness behaviour of the steel have been presented in chapter 4. The nature of application of the steel demands that its fracture resistance under cyclic loading be examined for careful assessment of its integrity in service. This requirement emerges from the fact, that fracture toughness behaviour in monotonic loading and in cyclic loading are different, and the latter is generally inferior compared to the former one. Several report e.g. that by Landes et.al. on 4340 and A 508 steel [8,9], Seok et al. [10,33] on SA 516 steel, Rudland et al [11] on SS304 and A106 steel etc., support the earlier statement. There is no report is available on the study of fracture toughness behaviour of SA 333 steel in cyclic loading condition. This aspect is the major content of investigation in this chapter.

Earlier investigations on crack growth resistance of structural materials under cyclic loading have established that either decrease in stress ratio or decrease in plastic displacement degrades the fracture toughness of the material [10,11]. Thus it is required that the effect of these variables on the cyclic crack growth resistance of SA 333 steel should also be explored systematically. In addition one finds scanty efforts are directed to understand micro mechanism of crack propagation during this type of tests. This aspect is also considered pertinent while an investigation is being made on cyclic crack growth resistance of this steel. Further the cyclic fracture toughness tests are tedious, expensive and time taking in nature compared to monotonic fracture toughness tests. It would thus be useful if a correlation can be established between monotonic and cyclic fracture toughness properties of steels. In this part of investigation, some attempts were also directed to address this problem.

In summary the objectives of the investigation presented in this chapter are (i) To examine the effect of cyclic loading on the *J-R* curves at various stress ratios. (ii) To study the effect of plastic displacement on the cyclic *J-R* curves. (iii) To understand the micro mechanisms of crack propagation in the material

during various types of cyclic loading and (iv) to search for correlation between the monotonic and cyclic fracture toughness of the selected steel.

5.2 EXPERIMENTAL

5.2.1 Cyclic *J-R* Curve Testing

The cyclic *J–R* curve testing was carried out using compact tension specimens as described in section 4.1.1. A series of these tests were carried out and the details of the specimen used for this investigation are given in Table 5.1. These tests were done with the help of an INSTRON machine (the actuator of the machine being attached with an anti rotation fixture) and with the use of a COD gauge. The details of the testing system have been previously described in section 3.1.5. An additional x-y recorder was attached to the analogue out put ports of the machine to get on line load displacement plot during a test, apart from recording the digital data in a computer (§ section 3.1.5).

The cyclic *J* tests were semi-automated. The loading sequence for the test is given in Fig.5.1 while the test variables are shown in the Table 5.2. The cyclic *J* tests were carried out in stroke control mode using an actuator speed of 0.5mm/min. Each test consisted of the following steps as shown in Fig.5.2.

(1) A specimen was loaded (segment OA in Fig.1) to a desired plastic displacement level ΔV (0.15, or 0.3 or 0.5 mm),

(2) This was then unloaded to the desired predetermined load P_{min} ($=R.P_{max}$) where R is the stress ratio on which the test was being conducted and P_{max} is the load achieved before start of unloading. The magnitude of R was varied in different tests (§ Table 5.2)

(3) Next it was reloaded till it achieved the displacement level corresponding to point C in the unloading path (as shown in Fig.5.2)

(4) The specimen was further loaded to the next desired plastic displacement level (as shown by point D in Fig.5.1 and Fig.5.2) and the steps 2 to 4 were iterated. These iterations were continued till the maximum load-bearing capacity of the sample or to a point corresponding to some significant crack growth in the specimen (as observed on the specimen surface).

(5) After the completion of the cyclic *J* test, the specimens were post fatigue cracked till failure.

The digital data of load, position and LLD were collected through a computer attached to the machine.

The initial and the final crack length were optically measured using a travelling microscope as described in section 4.1.2 on the broken fracture surface of three specimens. The optically measured value of crack length was found to be within ±0.05mm of what has been estimated from CCL relation {§ eqn. (4.3) in section 4.2.3}

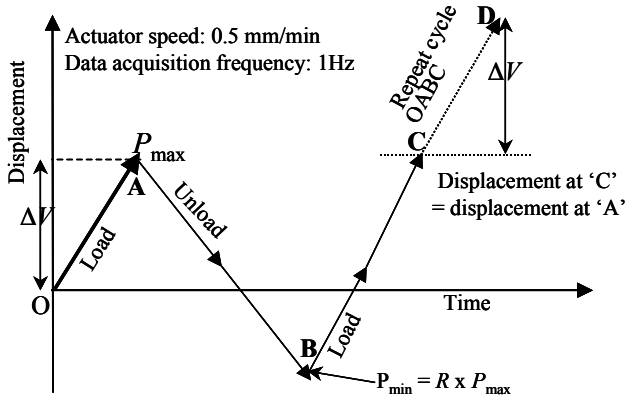

Fig.5.1 Loading sequence for cyclic J at zero and negative stress ratios, conducted with pre-selected values of ΔV and R as shown in Table 5.2.

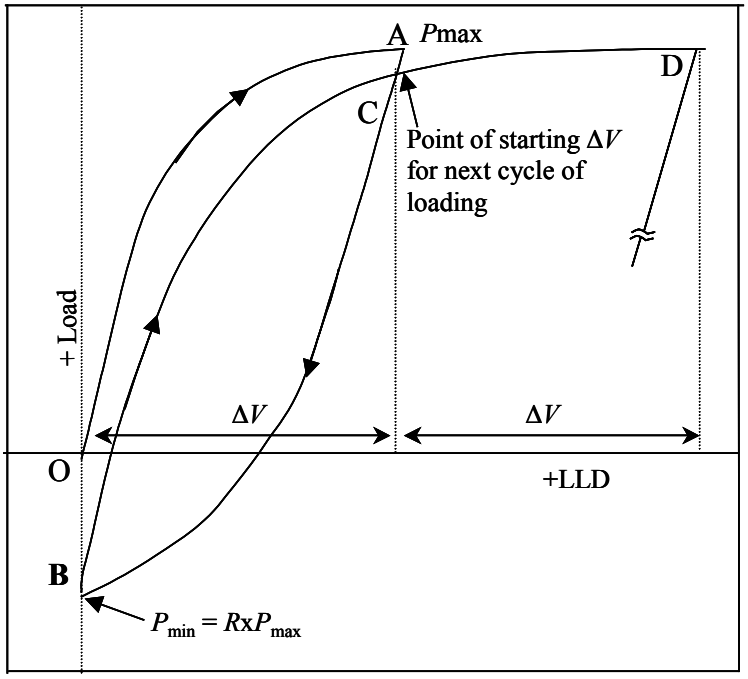

Fig.5.2 Demonstration of loading sequence for negative stress ratio cyclic ***J*** tests

Table 5.1. Dimensions of the specimens used in cyclic *J* test together with the fatigue pre-cracking conditions.

Sl. No.	Specimen Code	W (mm)	B (mm)	B_N (mm)	a_N (mm)	a_o (mm)	$\Delta K^{\#}$ (MPa√m)
1.	LC5	50.14	25.02	19.9	15.5	25.11	18.48
2.	LC6	50.21	24.83	20.04	15.4	25.07	18.71
3.	LC7	50.20	25.03	19.32	15.6	25.08	18.43
4.	LC8	50.16	25.04	19.85	15.6	25.08	18.08
5.	LC9	50.22	25.03	19.52	16.19	25.05	16.90
6.	LC10	50.32	24.98	19.64	16.34	25.01	16.64
7.	LC11	50.18	25.02	20.08	16.47	25.01	16.64
8.	LC12	50.18	25.04	19.82	16.59	25.13	16.58
9.	LC13	50.05	25.05	19.87	15.49	25.02	17.54
10.	LC14	50.01	24.94	19.85	15.46	24.96	16.74
11.	LC15	50.13	25.03	19.80	15.85	25.06	16.74
12.	LC16	50.13	25.03	19.52	16.34	25.02	16.84
13.	LC17	49.94	25.04	19.64	19.76	25.16	18.64
14.	LC18	50.40	24.90	19.87	15.98	25.09	18.31
15.	LC19	50.41	24.94	19.85	16.16	25.02	18.34
16.	LC20	49.61	24.98	19.80	16.30	24.98	18.36
17.	LC21	50.09	24.85	19.53	16.42	25.21	18.52
18.	LC22	50.54	24.86	19.98	15.47	25.23	16.90
19.	LC23	50.87	24.86	20.24	15.82	25.71	16.64
20.	LC24	50.36	24.89	19.37	16.56	25.14	16.64
22.	CL5	50.58	24.91	19.52	16.51	25.18	17.54
23.	CL6	50.9	24.92	19.64	16.38	25.83	16.74
24.	CL7	50.74	24.95	20.08	16.49	25.52	16.74

$\Delta K^{\#} = \Delta K$ at the end of pre-cracking, W = width of the specimen,
B= total thickness of the specimen, B_N = net thickness of the specimen
a_N = machine notch length of the specimen, a_o = crack length after pre-cracking,

Table 5.2 Test variables for cyclic *J* tests.

Specimen Orientation	Stress Ratio *R*	Plastic Displacement ΔV (mm)
	N (0.9)	
	0	0.15
LC	-0.5	0.30
CL	-0.8	0.50
	-1.0	
	-1.2	

5.2.2. Fractography

The fractured surfaces were ultrasonically cleaned and then examined under a scanning electron microscope. The prominent features of interest were recorded. Fractographs of ductile crack extension were recorded for each specimen. Two additional tests were carried out for fractographic examinations. These are: (a) after the completion of a cyclic *J* test, a specimen was subjected to zero load level in its unloading path and was taken out and (b) a similar specimen was taken out during its loading path from a minimum load corresponding to $R = -1$. These specimens were sectioned from the mid thickness encompassing the crack tip. The specimens were slowly polished starting from grade 80 onwards up to 1200. Next the specimens were successively polished on Texemet cloth using diamond paste of particle sizes 1μm and 0.25μm. These polished samples were observed in optical microscope and SEM with suitable recording of the crack path.

5.3 RESULTS AND DISCUSSION

The results obtained from the cyclic *J* tests and the concerned fractographic studies are described in this part. The observations are discussed with respect to (i) Development of cyclic *J-R* behaviour, (ii) Effect of stress ratios on cyclic *J-R* curve, (iii) Effect of plastic displacement on cyclic *J-R* curve, (iv) Determination of critical *J* and d*J*/da, (v) Validation of linear summation model (vi) Monotonic fracture toughness *vis* a *vis* cyclic fracture toughness, (vii) Alternative analysis of cyclic *J* test, and (viii) Mechanism of crack propagation under cyclic loading.

5.3.1. Development of Cyclic *J–R* Curves

Typical recorded load *vs* load line displacement (LLD) plots generated during cyclic *J* tests are shown in Fig.5.3. The *J-R* curves were constructed using these load-LLD data as described in section 4.2.3. The magnitudes of J_e and J_{pl} were calculated using eqn (4.8) and eqn (4.11). The values of J_{pl} were estimated taking account of the area only under tensile loading following several earlier reports [10,11,33,98]. The crack length was calculated using the unloading data falling between P_{max} and 70% of P_{max}. The selection of the unloading data range for estimating the crack length was based on its compatibility with that estimated by optical measurements. The cyclic *J-R* curves were developed by plotting values of *J* against values of crack extension Δa.

The *J-R* curves for stress ratio $R = 0$ and for plastic displacements 0.15, 0.3 and 0.5mm are shown in Fig.5.4. All the cyclic *J-R* curves appear coincident at the stress ratio $R = 0$. Hence it may be inferred that the magnitude of plastic displacement do not considerably influence the *J-R* curves of the selected material at stress ratio $R = 0$. Kaiser [28] has reported that the resistance offered by *J-R* curve can decrease with decrease in plastic displacement for ΔV less than 62μm but for ΔV ranging between 62.5 and 250mm, the *J-R* curves obtained by this investigation for OX 813 steel are similar. Hence the current results of the invariant nature of *J-R* curve for $150 \leq \Delta V \leq 500$μm are in agreement with the results reported by Kaiser.

The monotonic *J-R* curves for ΔV=0.3mm are shown in Fig.4.7. Two additional *J-R* curves at plastic displacement 0.5 and 0.15mm were determined. A comparison of the monotonic and cyclic *J-R* curves at identical plastic displacements is illustrated in Fig5.5. The results in Fig.5.5 indicate that monotonic *J-R* curve at $R = 0.9$ is almost identical with cyclic *J-R* curves at R=0 for the three levels of plastic displacements at which these experiments were made. This observation is in accordance with the observations of Rudland et al. [11] for SS 304 and A106 Grade B steel. But Seok et al. and Joyce [27] have reported that cyclic *J-R* curves at $R = 0$ are inferior to the monotonic *J-R* curves for SA 516 Gr70 steel and 3% Ni steel respectively. It is not clear at this stage what exactly brings forth difference between monotonic and cyclic *J-R* curves at $R = 0$ in a few materials where as the *J-R* curves remain similar in some other material.

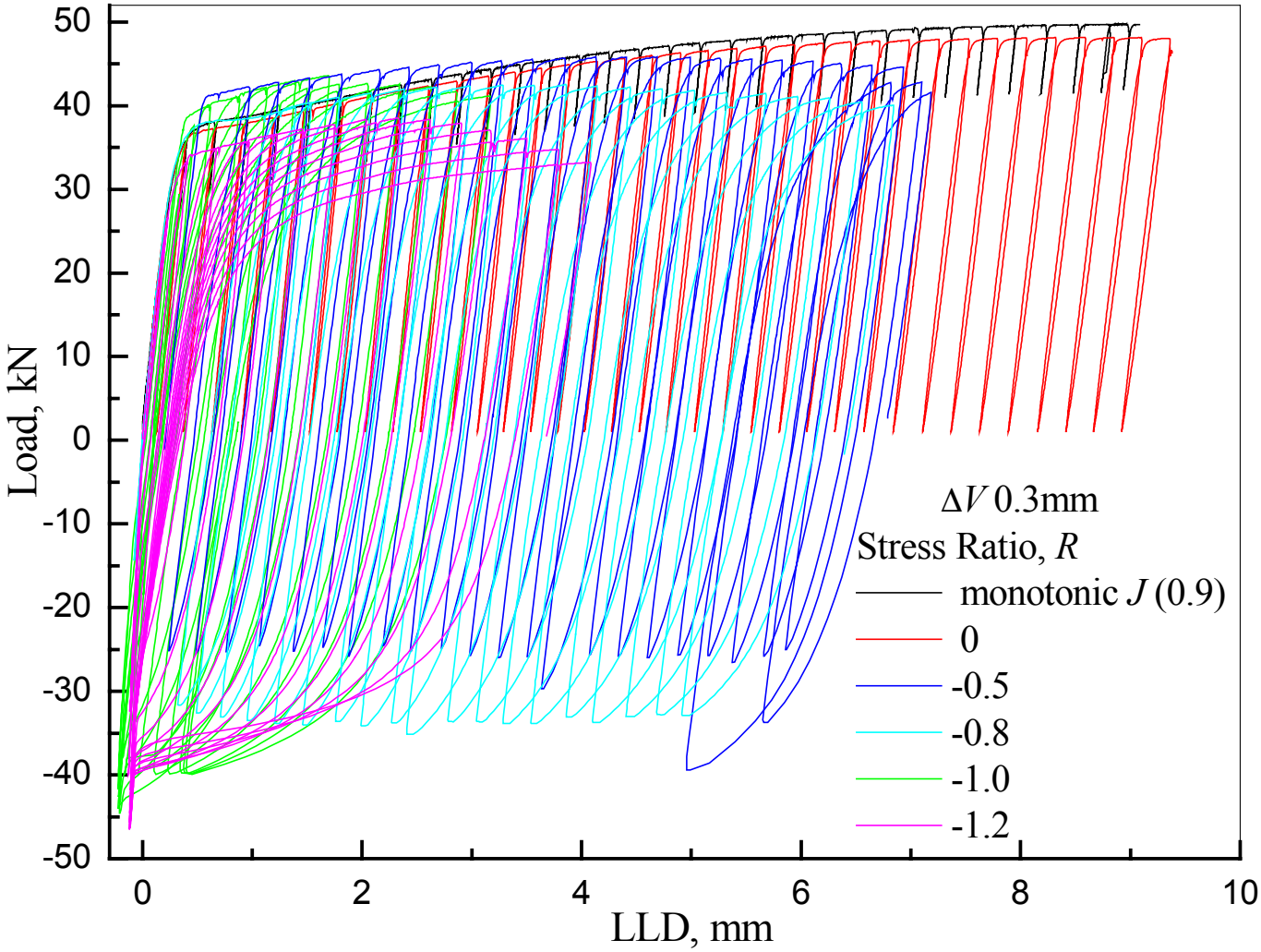

Fig.5.3 Typical load-displacement plots obtained during cyclic *J*-test on specimens with LC orientation

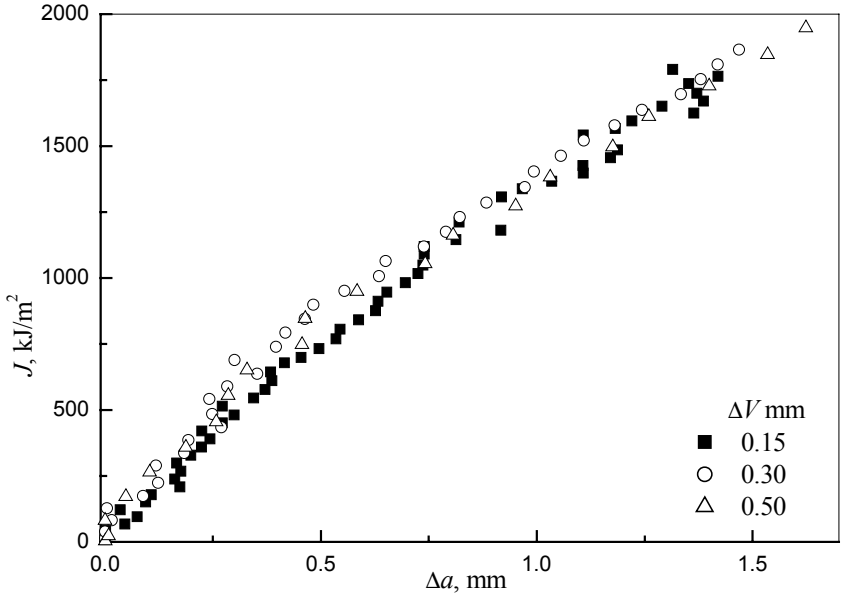

Fig.5.4 Effect of plastic displacement ΔV on *J*-*R* curve at the stress ratio 0 for LC specimen

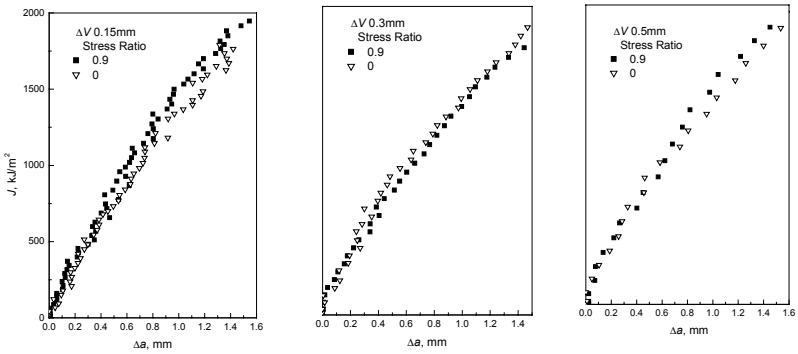

Fig.5.5 Effect of variation of stress ratio *R*.0 on *J*-*R* curve for LC specimens.

5.3.2. Effect of stress ratio on cyclic *J-R* curves

Some typical *J-R* curves generated using the experimental load-LLD data for R<0 are shown in Fig.5.6, Fig.5.7 and Fig.5.8 for ΔV = 0.3, 0.5 and 0.15mm respectively. At each plastic displacement level the *J-R* curves are found to lie systematically below each other with decrease in stress ratio. The *J-R* curves at the stress ratios $R = -1.0$ and -1.2 are, however, almost identical for $0.15 \leq \Delta V \leq 0.5$mm. Information related to cyclic *J-R* curves under tension-compression load cycle is limited [8-11,98]. Seok et.al. [10,33] have observed resistance to crack propagation for SA516 steel decreases as it is subjected to increased compressive loads; the minimum resistance to crack propagation being encountered at stress ratio R = -1.0. Landes and Liaw [9] have also observed cyclic *J-R* curves at R =-1.0 to be inferior to monotonic *J-R* curve for AISI 4340 steel. Rudland et al. [11] have also made observation for 304 and A 106 B steels; but the minimum resistance to crack propagation is attained at R = -0.8 and at –1.0 for A 106 B steel and 304 SS respectively.

A comparison of the present results related to *J-R* curves at $R < 0$ (Fig.5.6, Fig.5.7 and Fig.5.8) with similar results reported by earlier investigators indicate a general trend. It can be inferred that resistance to crack propagation in cyclic loading of structural materials deteriorates with increased magnitude of the compressive load cycle up to about R = -1.0, below which there is no further deterioration in the resistance to crack propagation. Rudland et al. has explained this phenomenon in terms of re-sharpening of the blunted crack tip and the void formed ahead of it [11]. It has been observed by them that both crack tip and void ahead of it gets compressed during the compressive load cycle and forms a sharp crack tip, which needs very less amount of energy to open up in the next cycle of tensile load. This phenomena causes decrease in resistance to crack propagation in the case of stress ratio $R < 0$.

5.3.3. Effect of plastic displacement on cyclic *J-R* curve

The effect of plastic displacement on the cyclic *J-R* curves is illustrated in Fig.5.9, Fig.5.10, Fig.5.11 and Fig.5.12 for the stress ratio –0.5, -0.8, -1.0 and –1.2 respectively. At negative stress ratio decreasing plastic displacement leads to enhanced degradation in the resistance to crack propagation. This is obvious from the results shown in Fig.5.9 to Fig.5.12 where one can notice that the cyclic *J-R* curve at ΔV = 0.15 lies below all others. The obtained nature of degradation of cyclic *J-R* curve is

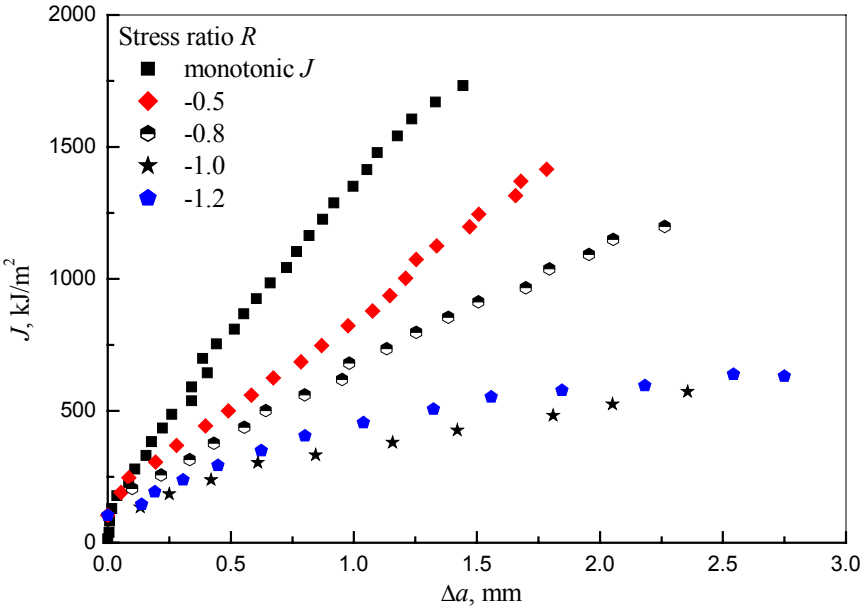

Fig.5.6 Effect of stress ratio on cyclic *J*-*R* curves for $\Delta V = 0.3$mm along LC orientation

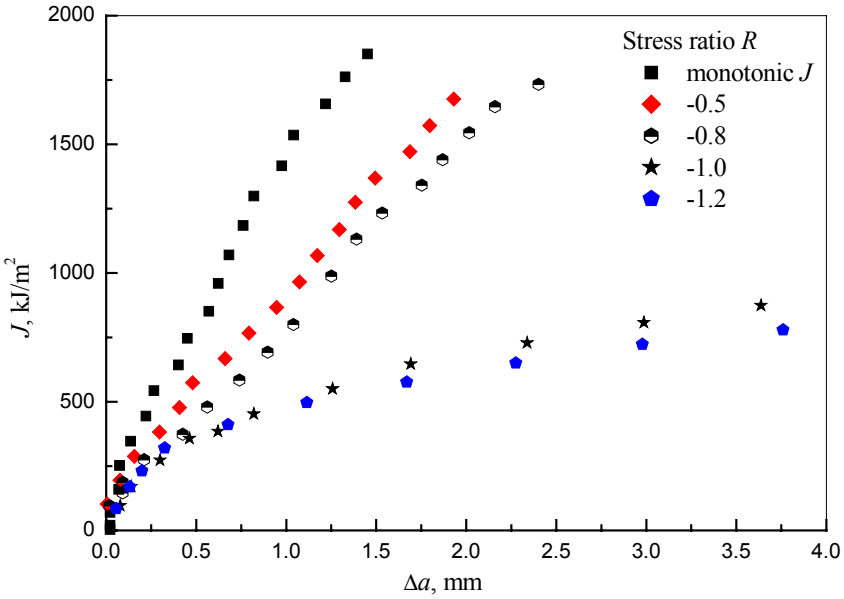

Fig.5.7 Effect of stress ratio on cyclic *J*-*R* curves for ΔV 0.5mm along LC orientation

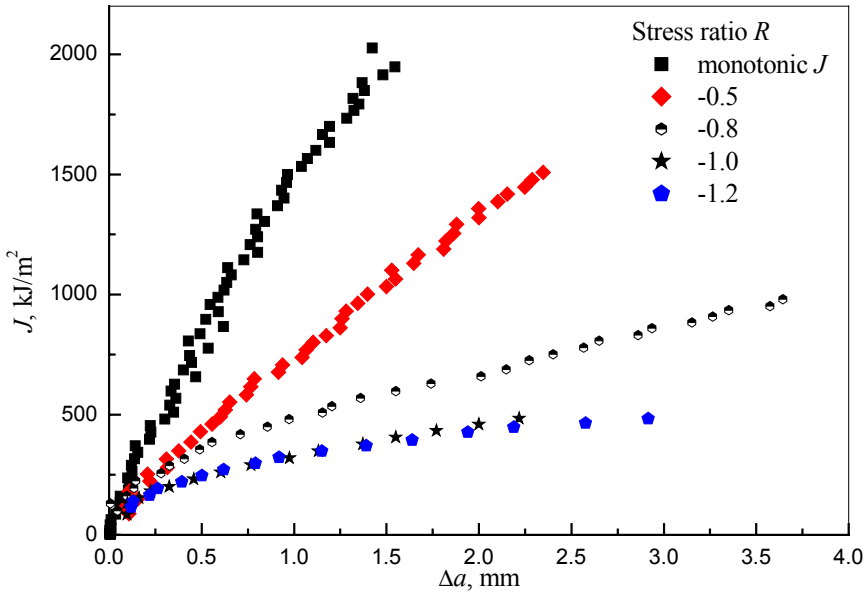

Fig.5.8 Effect of stress ratio on cyclic *J*-*R* curves for $\Delta V = 0.15$mm along LC orientation

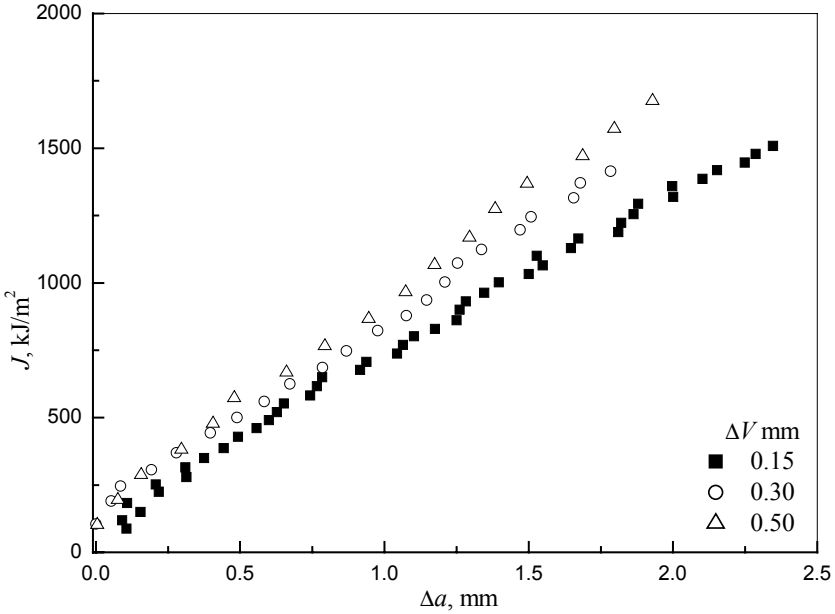

Fig.5.9 Effect of plastic displacement ΔV on *J-R* curve for the stress ratio -0.5 for LC specimen

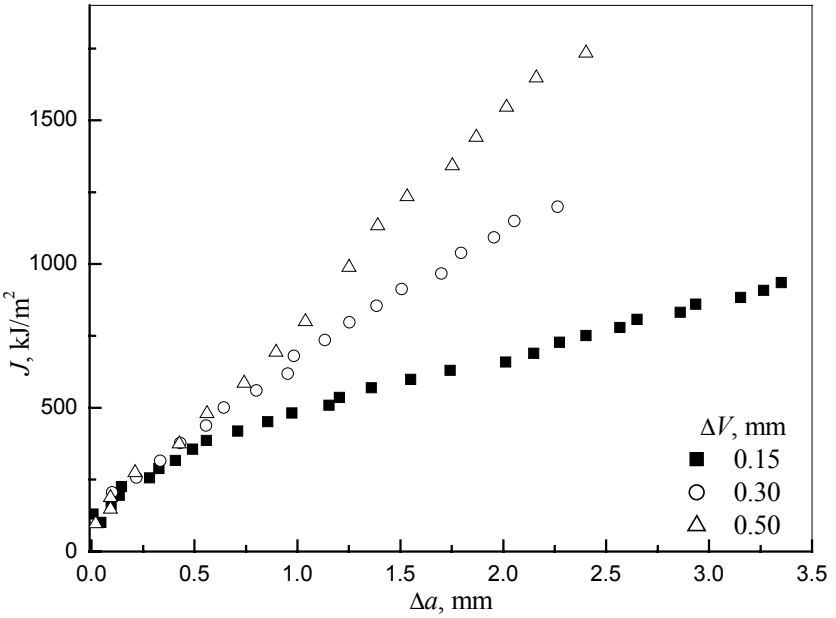

Fig.5.10 Effect of plastic displacement ΔV on *J-R* curve for the stress ratio -0.8 for LC specimen

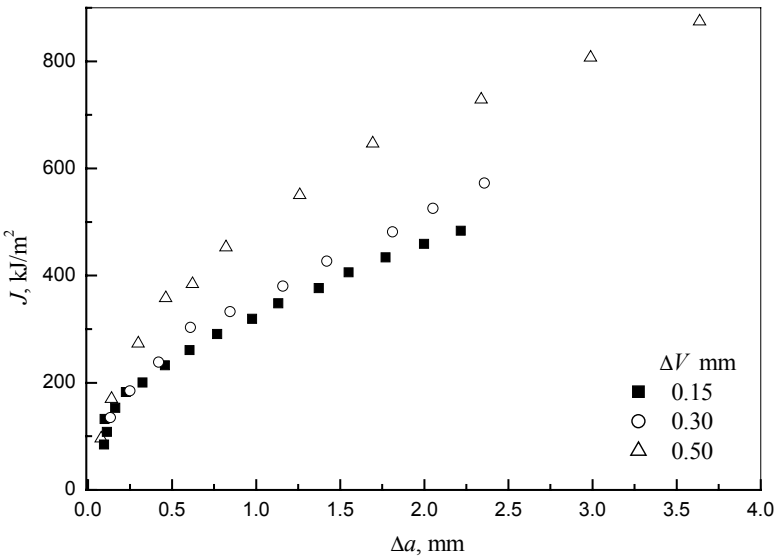

Fig.5.11 Effect of plastic displacement ΔV on *J-R* curve for the stress ratio -1.0 for LC specimen

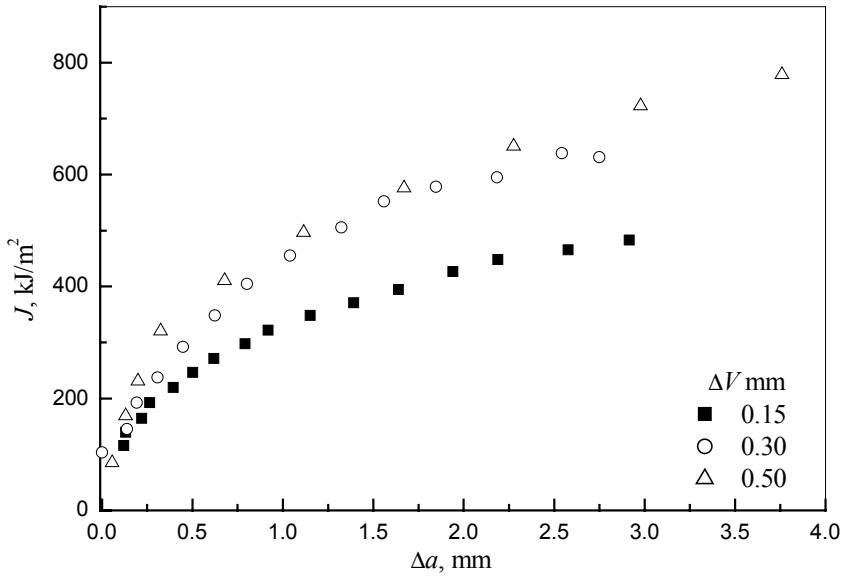

Fig.5.12 Effect of plastic displacement ΔV on *J-R* curve for the stress ratio -1.2 for LC specimen

similar to that observed by Landes et al. [8] and Seok et al. [10,33] for A 508 and SA 516 Gr 70 steel respectively. So it can be inferred that at negative stress ratio lower plastic displacement leads to higher degradation in resistance to crack propagation in structural materials; but variation of plastic displacement does not affect cyclic *J*-*R* curves of this material for stress ratio $R \geq 0$.

The decrease in plastic displacement during cyclic *J* test means imposition of more number of cycles for obtaining *J*-Δa variation. Alternatively when more number of cycles is imposed on a structural steel at negative stress ratio during cyclic *J*-test, the resistance to crack propagation degrades in comparison to that which requires less number of cycles for such tests. The decrease in the magnitude of cyclic *J*-*R* curve with increase in number of cycles is due to increased residual tensile stress at the crack tip. Soek et al. [10,33] had shown that when a specimen passes through zero load from compressive load, some amount of tensile residual stress is left at the crack tip at zero load, and increased number of cycles increase the magnitude of this residual stress. This aspect has been supported by suitable stress analysis carried out by Seok et al. [10,33]. The crack tip is subjected to more number of cycles at lower ΔV than that at higher ΔV. Since higher magnitude of tensile residual stress builds up at the crack tip in experiments conducted with lower magnitude of ΔV, the applied stress in conjunction with this results in inferior resistance to crack propagation.

5.3.4. Determination of critical *J* and d*J*/da

There is neither any standard nor any suggested guideline by any International Committee for evaluating fracture initiation toughness in cyclic *J* test unlike that [81] for monotonic J_c determination. An attempt has been made here to evaluate J_c from the cyclic *J*-*R* curves following the guidelines for evaluating J_c in monotonic tests. The magnitude of J_c in monotonic tests, as discussed in section 4.3.1, has been determined with the help of experimental blunting line. Similar attempts to obtain J_c in cyclic *J*-*R* curves were found unsuitable because points on the *J*-*R* curve qualifying for the experimental blunting line were a few in number. So an alternate method was adopted. The (J, Δa) data points lying between 0.15 mm to 0.3x(W-a_i) mm of crack extension were power law fitted to eqn. (4.13). The intercept of the fitted curve with a vertical offset at 0.2mm crack extension was considered as critical $J_{0.2}$. A typical example illustrating the procedure for the evaluation of $J_{0.2}$ is illustrated in Fig.5.13. This

method is in following the recommendations of European Structural Integrity Society (ESIS) [99]. The evaluated values of $J_{0.2}$, the relevant experimental conditions and the magnitudes of C_1 and C_2 obtained through eqn. (4.13) are reported in Table5.3. The magnitudes of $J_{0.2}$ for the monotonic *J-R* curves were also evaluated for comparison purpose and are shown in this Table.5.3

Table 5.3 Fracture toughness parameters for cyclic *J* tests

Specimen code	ΔV mm	Stress Ratio *R*	$J_{0.2}$ kJ/m^2	C_1	C_2	dJ/da MJ/m^3
LC5	0.15	0.9	405.28	1455.07	0.797	1209.30
LC6	0.15	0	375.61	1333.89	0.824	1145.76
LC7	0.15	-0.5	194.43	753.35	0.814	597.25
LC8	0.15	-0.8	199.25	478.98	0.554	200.716
LC9	0.15	-1	158.87	332.76	0.452	151.15
LC10	0.15	-1.2	168.84	322.47	0.404	114.50
LC11	0.3	0.9	413.66	1365.86	0.743	1088.50
LC12	0.3	0	438.66	1405.25	0.713	1085.12
LC13	0.3	-0.5	254.66	842.94	0.833	711.51
LC14	0.3	-0.8	223.85	681.22	0.696	469.47
LC15	0.3	-1	180.81	361.80	0.508	173.65
LC16	0.3	-1.2	211.92	429.322	0.437	169.69
LC17	0.5	0.9	399.55	1424.701	0.776	1183.88
LC18	0.5	0	419.64	1353.423	0.727	1031.79
LC19	0.5	-0.5	233.28	923.658	0.843	789.99
LC20	0.5	-0.8	245.47	814.96	0.698	714.05
LC21	0.5	-1	198.53	462.459	0.518	175.29
LC22	0.5	-1.2	242.59	481.135	0.371	130.66

The magnitudes of J_c and $J_{0.2}$ for plastic displacements ΔV=0.15, 0.3, 0.5 for monotonic tests are compared as a bar diagram in Fig.5.14. It is obvious from this figure that the magnitudes of $J_{0.2}$ are lower in comparison to the values of J_c, in agreement with the schematic illustrations in Fig.4.11. Since the magnitude of $J_{0.2}$ is lower and more conservative with respect to J_c, its value should be considered for life

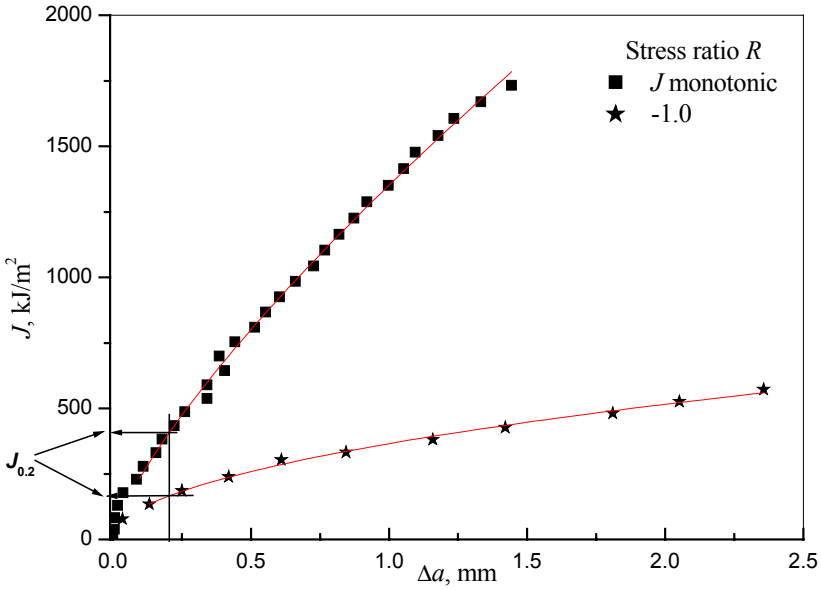

Fig.5.13 Evaluation of 0.2 mm vertical intercept fracture toughness $J_{0.2}$ at ΔV 0.3mm along LC orientation

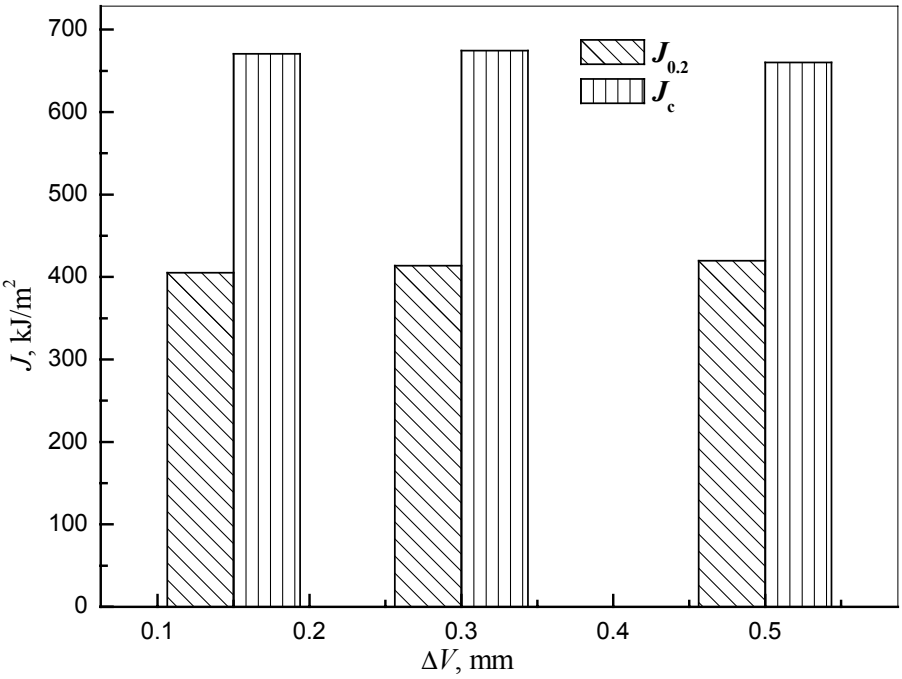

Fig.5.14 Comparison of values of J_c and $J_{0.2}$ for monotonic J tests

assessment of structural components subjected to cyclic loading till a standard emerges on measurement of fracture initiation toughness in cyclic loading.

The variation of fracture initiation toughness of the steel with stress ratio for different plastic displacements is shown in Fig.5.15. The magnitude of $J_{0.2}$ was found to decrease with decrease in stress ratio from 0 to –1.0. The fracture initiation toughness was found to be minimum at the stress ratio –1.0. The magnitude of $J_{0.2}$ at the stress ratio –1.0 for all the three plastic displacements was found to be 180±20 kJ/m^2. A comparison of $J_{0.2}$ at R = –1.0 with J_c at R > 0 indicates that the former is significantly lower (almost by about 55%) than the latter one. This observation is similar to that reported by Rudland et al. in 304 SS and A 106 B steel. These investigators have reported degradation of cyclic fracture initiation toughness for 304 SS and the A 106 B steel by 60% and 30% respectively [11].

The resistance to crack propagation (dJ/da) for cyclic J-R curves was also evaluated following the procedure described in section 4.3.1. The magnitudes of dJ/da are found to decrease with decrease in stress ratio from 0 to –1.2 for all the three plastic displacement levels as shown in Fig.5.16. The magnitude of dJ/da was found to be minimum at the condition R =-1.2 and ΔV=0.15mm. The dJ/da value at R= –1.2 is only about 11% of its monotonic value for plastic displacement 0.15mm. The decrease in dJ/da is found to lie in the range 85-88% for ΔV=0.3 and ΔV=0.5 mm. The cyclic loading through compressive loads has thus significant deleterious effects on the fracture initiation toughness and the resistance to crack propagation behaviour of SA 333 steel. The observed degradation of dJ/da in the investigated steel is in agreement with similar observations by Rudland et al. for 304 stainless steel and A 106 B steel [11]. The comparative analysis of $J_{0.2}$ and dJ/da in cyclic and monotonic loading thus lead to the conclusion that fracture initiation toughness and the resistance to crack propagation of materials degrade considerably in compressive cyclic loading.

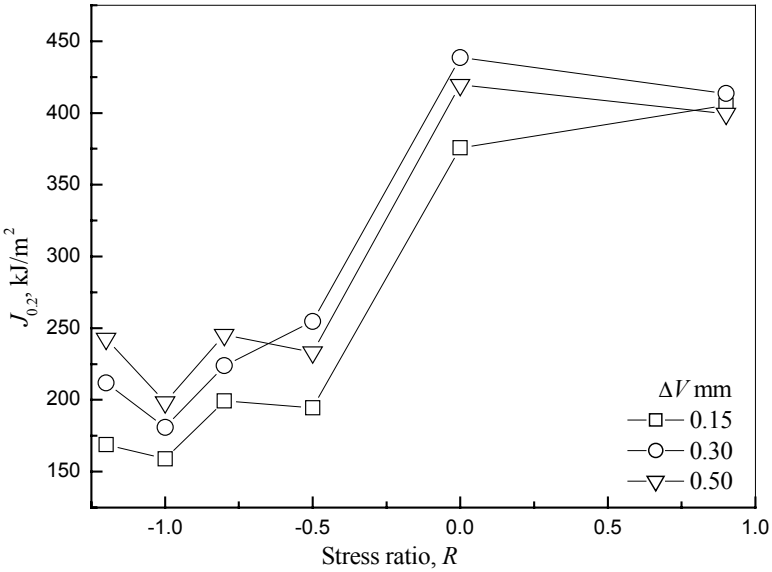

Fig.5.15 Effect of stress ratio on magnitudes of $J_{0.2}$ for specimens with LC orientation

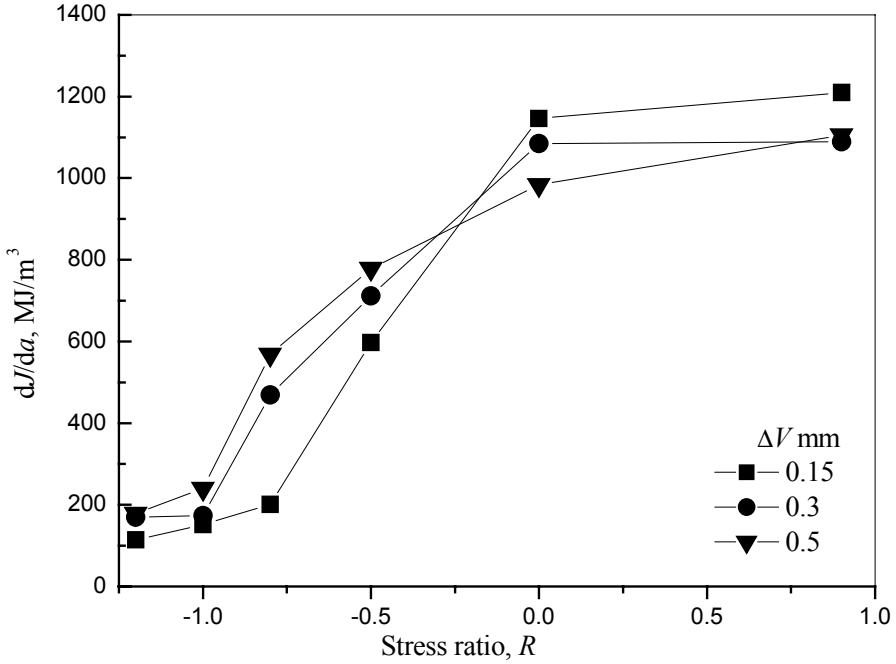

Fig.5.16 Effect of stress ratio on the magnitudes of dJ /da for specimens with LC orientation

5.3.5. Validation of linear summation model

Joyce[27] and Kaiser[28] have reported estimation of cyclic crack growth from monotonic and fatigue crack growth data for positive stress ratios ($R \geq 0$). They assumed that Δa_{cyclic} is linear sum of $\Delta a_{monotonic}$ and $\Delta a_{fatigue}$ as given below:

$$\Delta a_{cyclic} = \Delta a_{mono} + \Delta a_{fatigue} \tag{5.1}$$

where, Δa_{cyclic} = computed crack extension

$\Delta a_{monotinic}$ = crack extension due to monotonic tearing

$\Delta a_{fatigue}$ = crack extension due to fatigue cycling

In the present investigation attempts were made to examine this model for cyclic tension–compression loading (i.e. $R < 0$). The magnitude of $\Delta a_{fatigue}$ and $\Delta a_{monotinic}$ were computed as:

$$\Delta a_{fatigue} = \frac{da}{dN} = C(\Delta K)^m \tag{5.2}$$

where, C and m are Paris constants from conventional FCGR tests.

The magnitude of ΔK in eqn. (5.2) was taken as K_{max} because $K_{min} = 0$ for fatigue tests with negative R ratio as per ASTM standard E-647 [100]. The magnitude of K_{max} was obtained from the value of P_{max} achieved in each cycle during cyclic J test. This was done using the eqn (4.9).

$$\Delta a_{monotonic} = \left(\frac{J}{C_1}\right)^{1/C_2} \tag{5.3}$$

where, C_1 and C_2 are power law constants obtained from monotonic J-R curve.

A separate FCGR test was carried out to obtain the value of C and m for this material. This test was done following the ASTM standard E-647 [100] in decreasing ΔK mode. The fatigue crack growth data is given in Fig.5.17 and the experimental details for this test are given as legends. The log(da/dN) *vs* log(ΔK) were subjected to linear regression analysis to obtain the value of C and m. The magnitudes of $\Delta a_{monotonic}$ were obtained from the J-R curve data given in Table 5.3. Then the cyclic crack extension i.e. Δa_{cyclic} was evaluated by summing up $\Delta a_{monotonic}$ and $\Delta a_{fatigue}$.

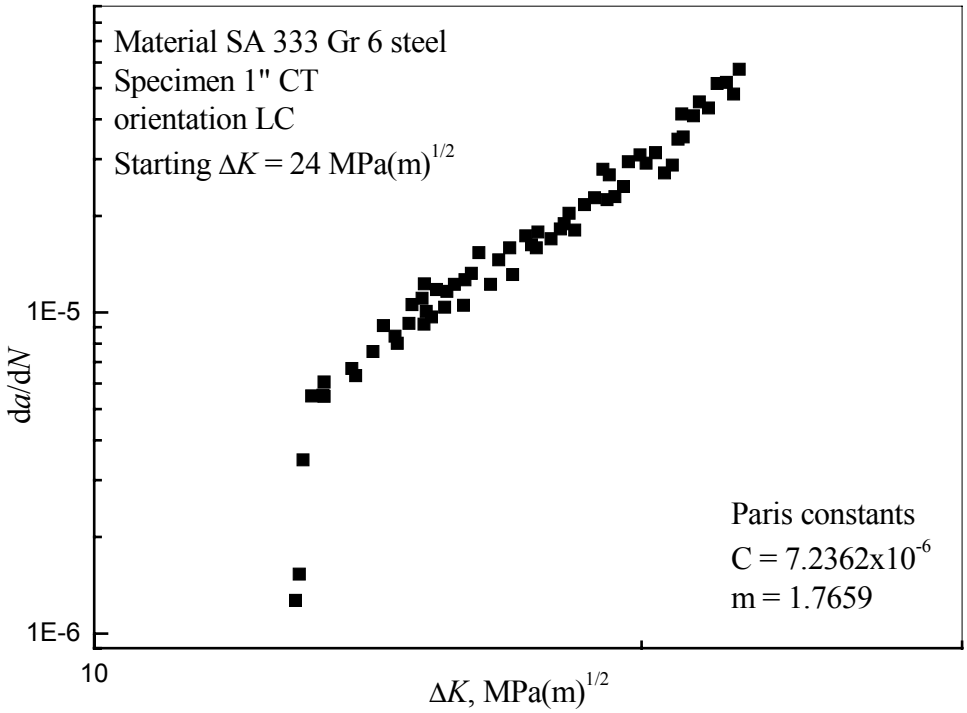

Fig.5.17 da/dN vs ΔK plot showing paris regime of fatigue crack growth behaviour of the material.

The computed values of Δa_{cyclic} were then compared with the crack extension data obtained from the cyclic *J* test (denoted here as Δa_{expt}). A typical comparison is illustrated in Fig.5.18 corresponding to cyclic *J* test carried out at ΔV = 0.5mm and *R* = -1.0.

The experimentally obtained Δa_{expt} is found to be always greater than the computed Δa_{cyclic}. This implies that there is some additional crack extension. This additional crack extension is considered to arise due to interaction between tear and fatigue and is denoted as $\Delta a_{interactive}$. Thus the simple linear summation model suggested by Joyce[27] and Kaiser[28] does not appear to be valid for negative *R* ratio. It may be noted here that the published literature in this direction are only for stress ratio $R \geq 0$ [27,28]. In the case of R<0, voids and crack tip re-sharpening enhances the stress tri-axiality. This results in additional crack extensions, $\Delta a_{interactive}$. It may thus be inferred that the cyclic *J* test crack extension data of SA 333 steel for negative stress ratio cannot be predicted by linear summation model.

The $\Delta a_{interactive}$ was computed by subtracting Δa_{cyclic} from Δa_{expt}. The nature of variation of magnitude of $\Delta a_{interactive}$ with the magnitude of $\Delta a_{fatigue}$ for ΔV=0.15, 0.3 and 0.5mm is given in Fig.5.19, Fig.5.20 and Fig.5.21 respectively. It is evident from the figures that $\Delta a_{interactive}$ is a function of ΔV and *R* ratio. Thus it can be concluded that $\Delta a_{interactive}$ increases with the decrease in stress ratio and decrease in the magnitude of plastic displacement and both have synergistic effect on it.

5.3.6. Monotonic fracture toughness *vis* a *vis* cyclic fracture toughness

Determination of cyclic fracture toughness of a material is tedious, time consuming and expensive in nature comparison to fracture toughness tests. As a consequence reports related to cyclic fracture behaviour of materials are limited in number unlike that for monotonic fracture behaviour, but information related to cyclic fracture toughness may be required for critical applications like nuclear power plants. An attempt is made here to search for a co-relation between monotonic and cyclic fracture toughness of the material in order to get a crude estimate of the latter from the former. Any such correlation will be of much use and will help in predicting the safe operation life of the components.

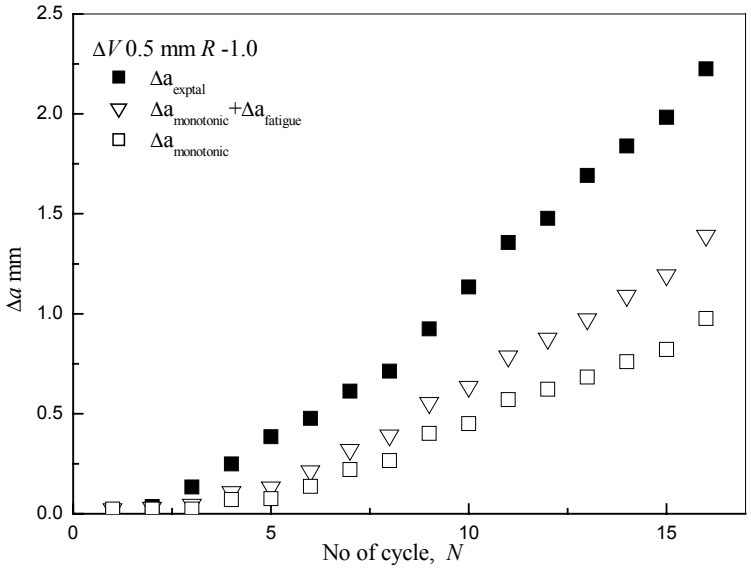

Fig.5.18 Comparision of experimental crack extension Δa_{expt} with computed crack extension Δa_{cyc} against no of cycle

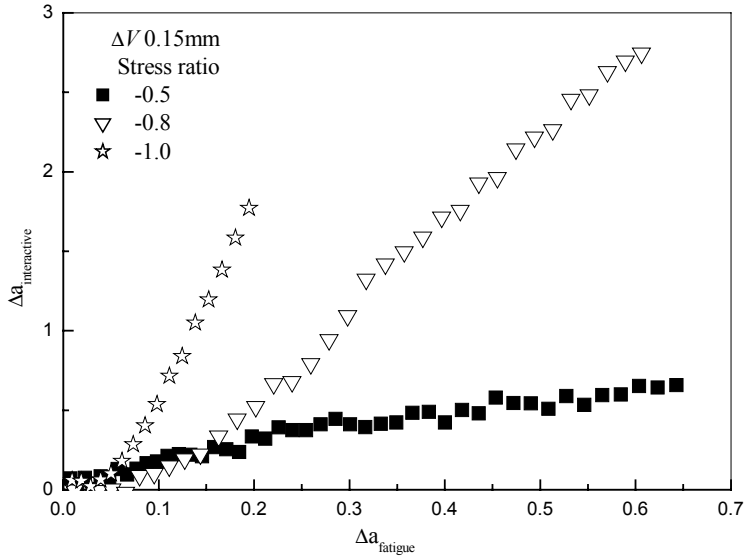

Fig.5.19 Variation of $\Delta a_{interactive}$ with $\Delta a_{fatigue}$ at ΔV=0.15mm

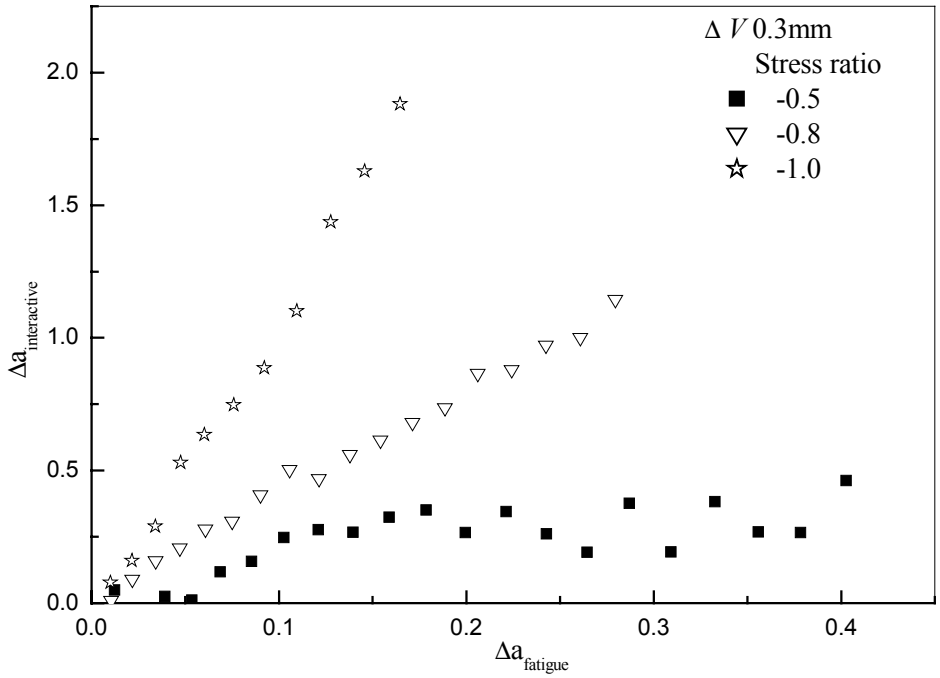

Fig.5.20 Variation of $\Delta a_{interactive}$ with $\Delta a_{fatigue}$ at ΔV=0.3mm

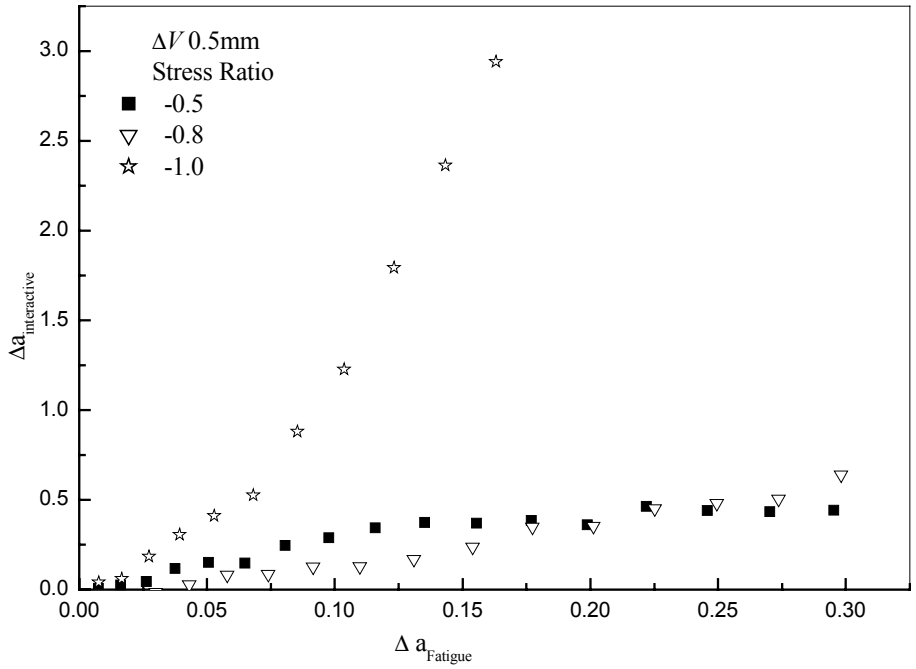

Fig.5.21 Variation of $\Delta a_{interactive}$ with $\Delta a_{fatigue}$ at ΔV=0.5mm

The effect of variation of cyclic $J_{0.2}$ for ΔV=0.15, 0.3, 0.5mm with the change in stress ratio has been given in Fig.5.15 for specimens having LC orientation. In this plot the data points lying between R = 0 and –1.2 were fitted to parabolic equations for all the three plastic displacement levels. For the three ΔV levels the obtained equations are as follows.

$$J_{0.2} = 371.1828+415.14998R+208.43993R^2 \qquad (5.4)$$

$$J_{0.2} = 438.37046+476.11117R+235.56541R^2 \qquad (5.5)$$

$$J_{0.2} = 416.56956+463.33397R+263.76488R^2 \qquad (5.6)$$

Eqn (5.4) to (5.6) are respectively for ΔV 0.15, 0.3 and 0.5mm respectively. Considering the equations to be of the form Y = A+Bx+Cx^2, it is noted that the magnitude of constants marginally increases with increase in ΔV and the magnitude of 'A' is marginally higher than $J_{0.2}$ monotonic. Some trial and calculations indicate that $J_{0.2}$ cyclic can be represented as function of $J_{0.2}$ monotonic in the following form equation and the curve obtained is shown in Fig.5.22

$$(J_{0.2})_R = (J_{0.2})_{monotonic} + \alpha_1\left(\frac{\sigma_f^2}{E}\right)B.R + \alpha_2\left(\frac{\sigma_f^2}{E}\right)B.R^2 \qquad (5.7)$$

where, $(J_{0.2})_R$ = 0.2mm vertical intercept fracture initiation toughness at stress ratio R
(the value of R lies between –0.5 to –1.0) and

$(J_{0.2})_{mono}$ = 0.2mm vertical intercept fracture toughness for monotonic loading are given in kJ/m^2.

σ_f = Engineering fracture stress and is in MPa.

E = the elastic modulus of the material and is in GPa.

B = thickness of the specimen and is given in mm.

α_1 = 1.77, α_2 = 0.897 and are constants

The equation developed has been employed to compute the values of cyclic $J_{0.2}$ at the stress ratio 0, -0.5, -0.8 and –1.0 along the crack plane CL orientation. The values are given in Table 5.4 along with the experimentally determined values. The predicted values of fracture initiation toughness for the stress ratio 0, –0.5, -0.8 and -1.0 are in good agreement with the experimentally determined values. A comparison of the two is given in the Fig.5.23.

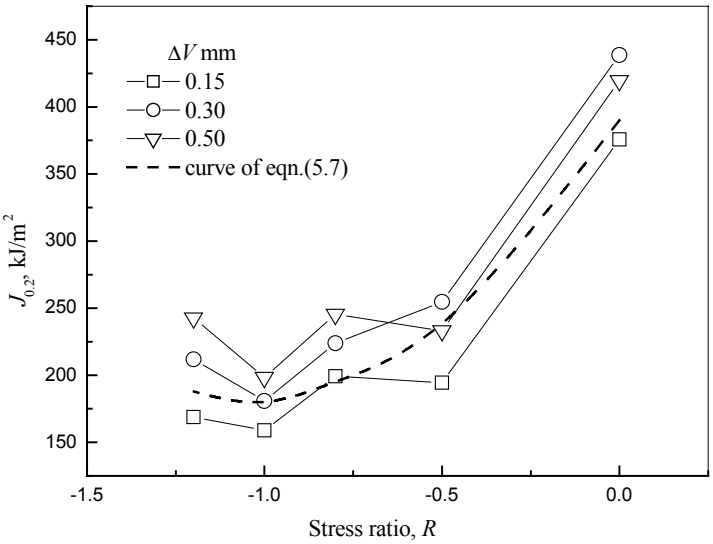

Fig.5.22 The parablic curve shown with the effect of stress ratio on magnitudes of $J_{0.2}$ for specimens with LC orientation

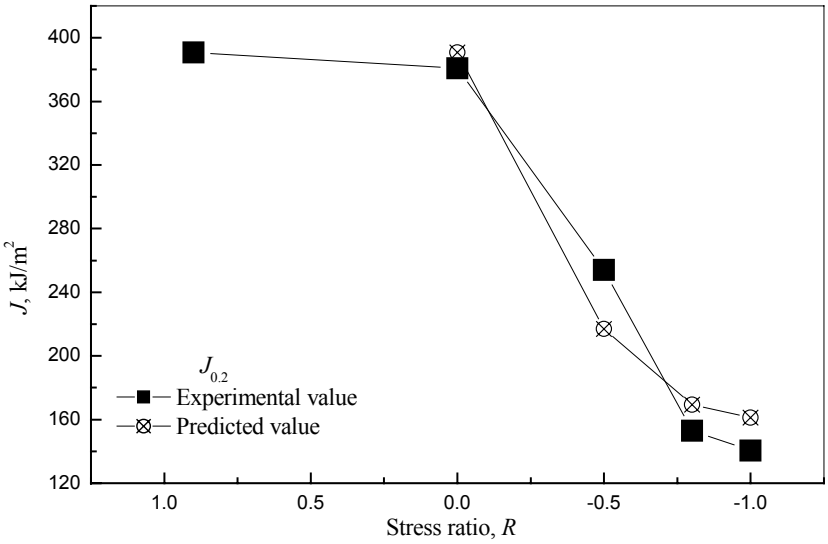

Fig.5.23 Comparision of experimental and predicted value of $J_{0.2}$ for various stress ratio R

Table5.4 The calculated and experimental $J_{0.2}$ values for various stress ratios along CL orientation

Stress Ratio	Predicted value ($J_{0.2}$) kJ/m^2	Experimental ($J_{0.2}$) kJ/m^2
0	390	380
-0.5	267.34	254
-0.8	188.5	153
-1.0	135.9	140.5

5.3.7. Additional analysis of cyclic *J* tests

Cyclic load *vs* LLD data can be used for determining fatigue crack growth rate of a material at higher *J* values. This can be done by two approaches one suggested by Dowling et al. [34] and the other by Mogami et al. [30]. Dowling's operational *J* is based on *J* integral concept of Rice. The operational *J* (termed here as ΔJ_D) has been evaluated in following Dowling et al [34] in the following steps:

(1) Load vs LLD plot was separated out for each cycle.

(2) The instantaneous crack length a_i was calculated as described in the section 5.3.1. The da/dN in each cycle was evaluated as (a_i-a_{i-1}).

(3) The closure load was identified by the change of slope in the compressive region of each loading cycle.

(4) The area under load *vs* LLD curve, above closure load was evaluated for each cycle. This area was converted to ΔJ_D using the equation:

$$\Delta J_D = \frac{\eta A}{(W-a_i)B_N} \tag{5.5}$$

where, A = area under the load displacement curve starting from the crack opening point

B_N = net thickness of the specimen

W = width of the specimen

a_i = instantaneous crack length

η = f(a/W) and is given by the expression given below

$$\eta = 2.0+0.522 \times \frac{(W-a_o)}{W} \tag{5.6}$$

The obtained values of da/dN were plotted against ΔJ_D (Fig.5.24) for the stress ratio –0.5 and –1.0 and ΔV = 0.5mm, along with fatigue crack growth rate (FCGR, Paris curve regime II) data. The data of regime III of the Paris curve (i.e. at P_{max} 32 kN load controlled test) has also been superimposed on the same graph. It is evident from the plot that ΔJ_D does not show any systematic trend with da/dN data. Similar observations were also made when ΔJ_D values estimated at ΔV =0.15 and 0.3mm were compared with FCGR data. Hence it can be concluded that ΔJ_D [34] approach does not explain the fatigue crack growth data of SA 333 steel.

Mogami et.al. [30] attempted to correlate J_{max} with da/dN. The J integral at the maximum load (J_{max}) was calculated using the equation proposed by Ando [101].

$$J^{n}_{max} = J_{max}^{\,n-1} \times \frac{(W-a_n)}{(W-a_{n-1})} + (J'-J'_{n-1}) \times \frac{(W-a_o)}{(W-a_{n-1})} \qquad (5.8)$$

where, J^{n}_{max} and $J^{n-1}_{max} = J_{max}$ at the nth and (n-1)th cycle respectively

a_o = initial crack length

a_n and a_{n-1} = instantaneous crack length at the nth and (n-1) cycle

J'_{max} and J'_{max} = J integral at the nth and (n-1)th cycle respectively, obtained from the area of the envelop of the cyclic load-displacement curve, which does not take into account the effect of crack growth and unloading.

The values of J_{max} for each cycle were calculated using the eqn. (5.8) for all the investigated stress ratios and plastic displacements. A plot of J_{max} *vs* da/dN has been given in Fig.5.25 for ΔV = 0.5mm. Similar trend has been observed for ΔV=0.15 and 0.3mm. The magnitudes of J_{max} do not fall on the extrapolated line of the best linear fit of the fatigue crack growth rate data of this material. It is evident from the figure that the crack growth is higher than what is predicted by da/dN *vs* ΔJ plot of this material. It can therefore be concluded that Dowling's operational J under-predicts the crack growth rate of the material where, as J_{max} concept of Mogami et al. over-predicts it.

5.3.8. Mechanism of crack propagation under cyclic loading

Some representative fractographs of ductile crack extension region of the (cyclic J) tested specimens for the stress ratios of 0.9, 0, -0.5, -0.8 and –1.0 are shown in Fig.5.26(a)-(e). These fractographic features of ductile crack extension region of specimens tested at R 0.9 and 0 are similar and exhibit prominent dimple fracture.

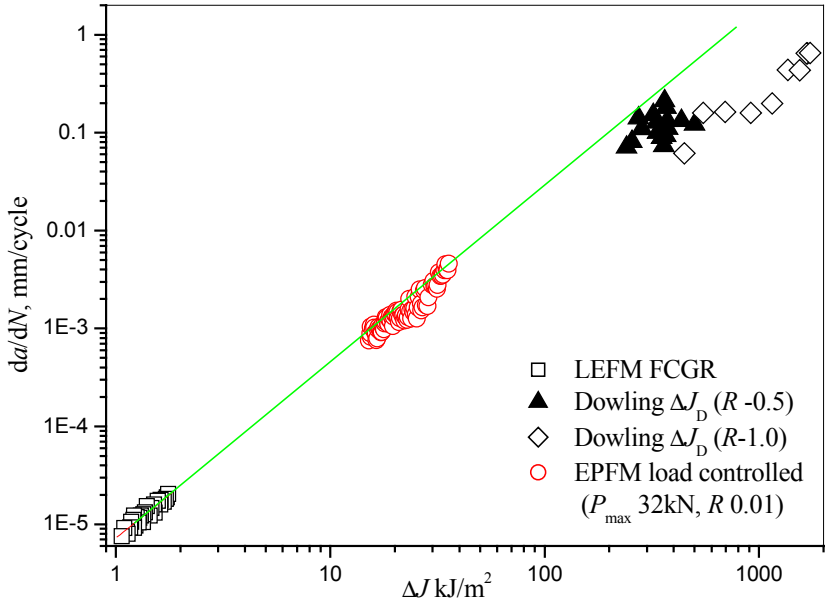

Fig.5.24 Dowlings ΔJ_D vs da/dN plot for the stress ratio -0.5, -0.8 and -1.0

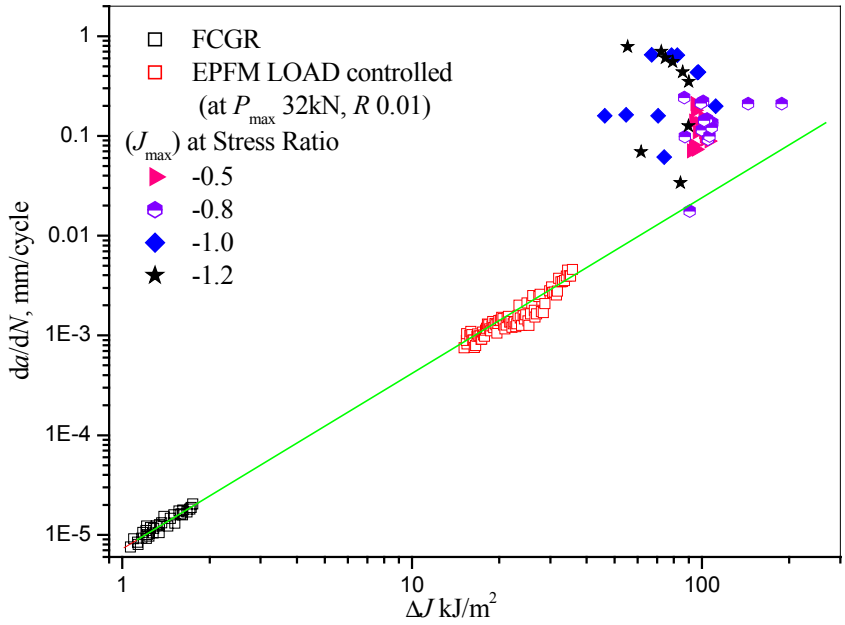

Fig.5.25 J_{max} vs da/dN plot for the stress ratio -0.5, -0.8 and -1.0 along LC specimen

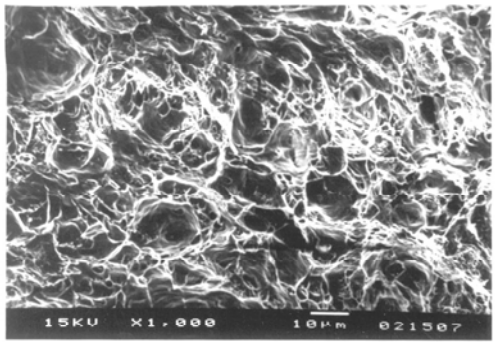

Fig.5.26(a) Typical fractograph of the ductile crack extension region of a specimen tested under monotonic loading condition i.e. R~ 0.9 and ΔV=0.3mm

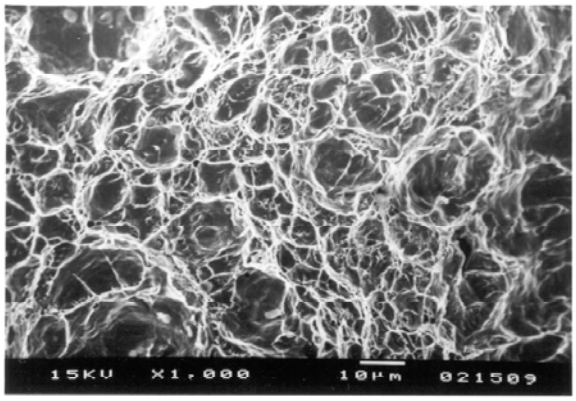

Fig.5.26(b) Typical fractograph of the ductile crack extension region of specimen tested at the stress ratio R= 0 and ΔV=0.3mm

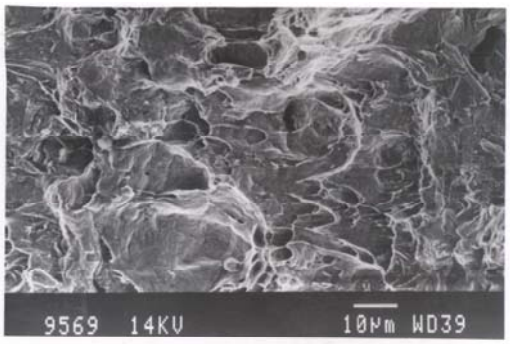

Fig.5.26(c) Typical fractograph of the ductile crack extension region of specimen tested at the stress ratio R= -0.5 and ΔV=0.3mm

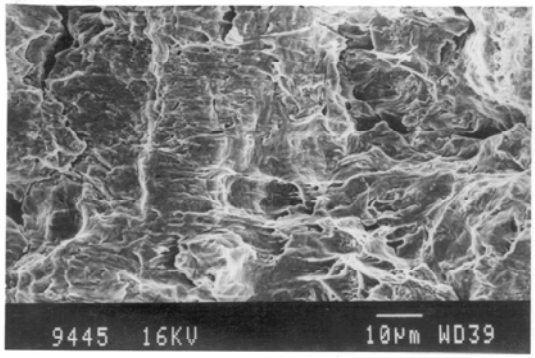

Fig.5.26(d) Typical fractograph of the ductile crack extension region of specimen tested at the stress ratio R= -0.8 and ΔV=0.3mm

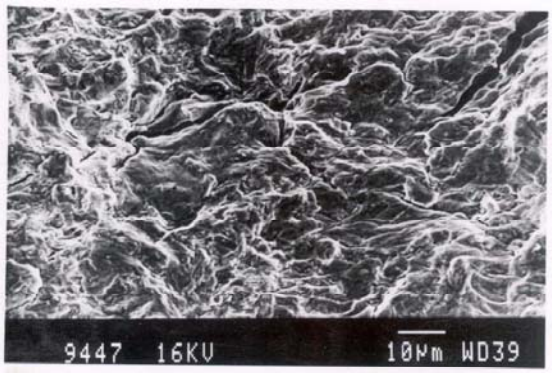

Fig.5.26(e) Typical fractograph of the ductile crack extension region of specimen tested at the stress ratio R= -1.0 and ΔV=0.3mm

But as the stress ratio becomes negative and higher in magnitude, the crack extension regions either show partial or no dimple regions, as evident in fractographs shown in Fig5.26(c)-(e). At the stress ratio R = –0.5, some dimples and or contours of these are observed, but at R = -0.8 and below no dimples could be detected. Additionally some fissure marks are noticed in the fracture surfaces of specimens tested at R = -0.8 and below.

The observations in fractographs shown in Fig.5.26(a) to (e) can be explained in the following manner. At positive R ratio dimples are initiated under tensile loading. At negative R ratio with lower magnitudes of R the compressive load cycles induce smearing and rubbing of the crack faces and thus gradually eliminate the dimple features. At still higher magnitude of negative R ratio, two possibilities exist: either dimples are completely smeared or rubbed or the formation/ growth of the dimples is inhibited during the compressive cycle. The existence of the fissure cracks on fracture surfaces of specimens at negative R ratio can be considered to be characteristics of compressive load cycles. Thus it can be inferred that the formation of dimples, their smearing and formation of fissure cracks govern the mechanism of crack propagation during cyclic J test. The smearing of dimples and the presence of fissure cracks are not observed on fractographic surfaces of specimens tested in monotonic loading {§ Fig.5.26(a)}. Hence it can be concluded that the mechanisms of crack propagation in cyclic and monotonic tests are different.

The interrupted test fractography of a few cyclic J test specimens were done at the three following conditions for examining the crack tip profiles: (a) monotonic J-test, stopped at tensile load, (b) cyclic J test at R = -1.0 and ΔV = 0.3mm, test stopped at the maximum tensile load; (c) cyclic J in above condition (b), test stopped at the minimum compressive load. The SEM photographs of the crack tip profiles of the above specimens are shown in Fig.5.27(a)-(c). The crack tip profile of monotonic J-tested specimen reveals blunted crack tip with a void present ahead of it as shown in Fig.5.27(a). The crack tip profile of the cyclic J specimen stopped after tensile loading is given in Fig.5.27(b). The crack profile in Fig.5.27(b) has less opening at the crack tip in comparison to monotonic J test. The crack tip appears more sharpened and the voids ahead of it seems to just opened up and joined with the main crack giving rise of crack extension.

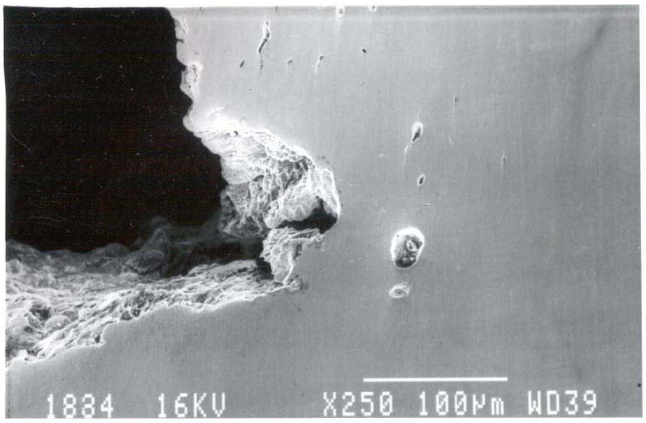

Fig.5.27(a) Crack tip profile of the specimen tested under monotonic loading condition R~0.9 and ΔV=0.3

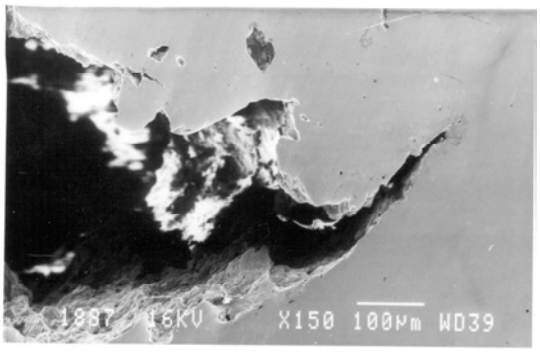

Fig.5.27(b) Crack tip profile of the specimen tested under cyclic loading condition (R= -1.0, ΔV=0.3) and interrupted immediately after tensile loading.

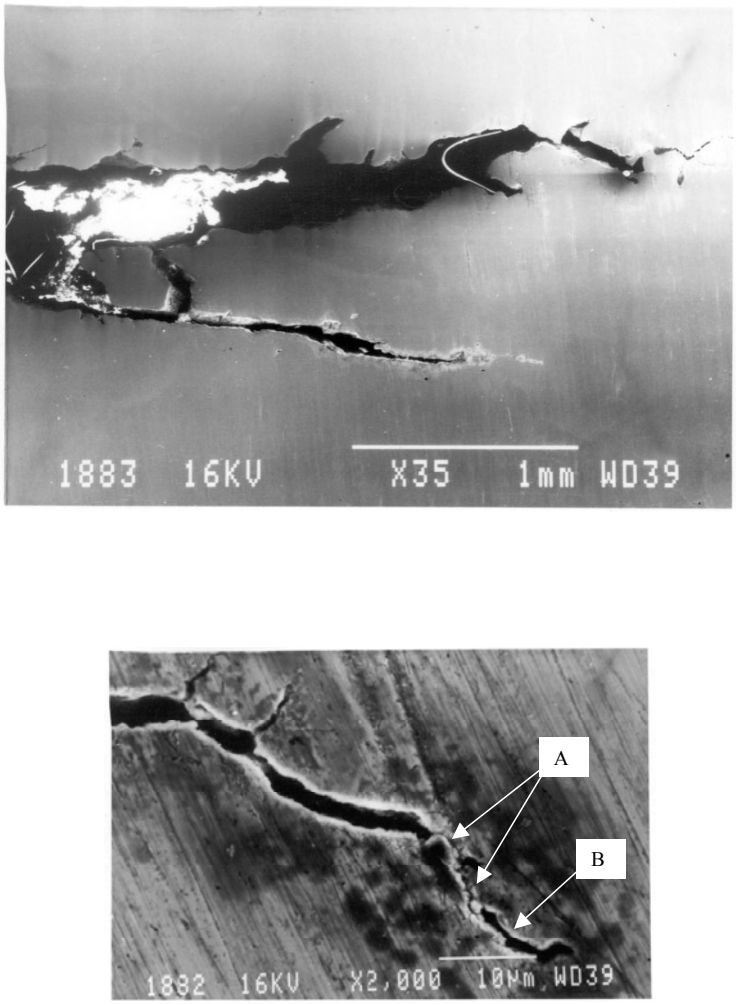

Fig.5.27(c) Top: Crack tip profile of the specimen tested under cyclic loading condition (R= -1.0; ΔV=0.3) and interrupted immediately after compressive loading.

Bottom: Enlarged view of the marked window in the top figure.

The crack profile of the cyclic *J* tested specimen, interrupted after compressive loading is given in Fig.5.27(c). The irregular shape of the crack profile exhibits propensity of the crack surface to branch out, leaving features of fissures on the fracture surface. The primary crack is found associated with several secondary cracks. A magnified view of the crack tip is also illustrated. Re-sharpened crack tip and voids are indicated by arrow marks at A and B positions respectively in Fig.5.27(c).

There is a large secondary crack originated from the primary crack in the case of cyclic *J* tests for negative *R* ratio. This grows parallel to the primary crack extension. Thus the total displacement observed during cyclic *J* test comes from both primary and secondary crack extensions The crack length calculations usually done from CCL relation as given by the equation (4.3) using total compliance will result in higher magnitude of primary crack extension than what actually is happening to the primary crack in the specimen. This higher magnitude of primary crack extension will result in lowering of the magnitudes of energy absorbed as the expression (4.11) for *J* calculation depends on crack length also. This is one of the contributing factors, in apparent lowering of the fracture resistance behaviour of the material during cyclic *J* test.

Another major point to be noted here is that the crack branching in the case of cyclic loading makes the crack estimation in cyclic *J* conditions complex. Up till now there is no method by which both primary and secondary cracks can be estimated correctly during a test and a perfect cyclic *J R* curve be developed. In absence of any such thing one is left with the conventional *J-R* curve approach, which can only considers primary crack extension. Only positive point of this method is that it will give lower bound value, hence it can be used in LBB analysis of the components reliably.

5.4. CONCLUSIONS

The conclusions derived from the results of investigations carried out in this chapter are summarized as:

1. The cyclic *J*-*R* curves of SA 333 steel are similar at $R \geq 0$ and these curves lie within a scatter band of monotonic *J*-*R* curves. But the decrease in stress ratio from 0 to –1.0 has deteriorating effect on cyclic crack growth resistance.

2. Lower plastic displacement (ΔV) results in inferior cyclic crack growth resistance curves for $R < 0$, whereas no such effect has been observed in the case of monotonic *J*-*R* curves and cyclic *J*-*R* curves at $R \geq 0$.

3. The fracture initiation toughness $J_{0.2}$ and the resistance to crack propagation (dJ/da) were found to decrease with the decrease in the stress ratio from 0 to –1.0 and with the decrease in the plastic displacement (ΔV).

4. The faster crack propagation at $R < 0$ is due to re-sharpening of the crack tip due to compressive load and their joining with the smeared voids.

5. The linear summation model [28] of the cyclic crack growth for $R \geq 0$ could not be validated for cyclic *J* tests at $R < 0$. The experimentally determined cyclic crack extension is more than the sum of monotonic and fatigue component of crack extension. The additional crack extension is due to interaction of tearing and fatigue phenomena, and this is termed here as $\Delta a_{\text{nteractive}}$. Its magnitude varies with the variation of R and ΔV.

6. An empirical expression has been suggested between cyclic and monotonic fracture initiation toughness.

6.0 CONCLUDING REMARKS AND FUTURE WORK

In this chapter the major conclusions drawn at the end of chapter 3 to chapter 5 are reviewed, implication of the experimental investigations and their analysis are discussed and suggestions are made for further research.

All critical engineering applications demand assessment of the structural integrity of components in the employed service conditions for their safe operation. The primary heat transport (PHT) pipings of pressurized heavy water reactors (PHWRs) is one such component in the nuclear power plants. This component is designed and operated on the basis of leak before break (LBB) concept. The LBB concept is based on the principles of fracture mechanics. This approach attempts to ensure that no catastrophic rupture would occur of an engineering component without prior indication of leakage. To ensure LBB concept, information and understanding of the fracture behaviour of the material used for fabrication of a component, are required. The PHT pipes of some nuclear power plants are often made of SA 333 Gr 6 steel, the material of interest in this investigation. A coolant D_2O enters into the PHT piping at 249^oC and exits it at 293^oC. In order to assess the structural integrity of this component understanding of the fracture resistance behaviour of SA 333 steel upto the temperature of 300^oC is required. This investigation has been directed to achieve such understanding.

The SA 333 steel is a plain carbon variety, which are usually susceptible to dynamic strain aging (DSA) phenomenon. Since the service temperature of this material can be upto 300^oC, it is essential to look forward for possible DSA in this material prior to fracture toughness studies, because DSA is known to degrade ductility and toughness of materials. A systematic investigation of DSA in this material has been carried out through tests at elevated temperatures and with variation of strain rates by two orders. Prior to these tests microstructural features and the relevant mechanical properties of the steel have been characterized to establish that the material belongs to ASME SA 333 Gr 6 /ASTM A 333 specifications. In the investigated test conditions at elevated temperature the occurrence of DSA in this steel has been established using evidences of serrations in the pre-necking regions of flow curves, increase in tensile strength and decrease in percentage elongation. A few strain rate change test have been carried out to confirm the occurrence of this phenomenon.

The fracture toughness studies carried out revealed that the material shows high fracture resistance behaviour at ambient temperature and the reason for this has been attributed to the high degree of cleanliness and finer sizes of inclusions. The characteristics of the stretch zone in the investigated steel, is of unconventional type and is intermixed with ductile tearing. The J_i estimated from the first expanse of stretch zone matches with the magnitude of fracture initiation toughness measured by DCPD technique [88] whereas J_i value obtained from the total expanse of stretch zone is close to J_{QC} values estimated in this study. The fracture initiation toughness and the resistance to crack propagation of the steel is inferior along CL plane in comparison to that of LC plane due to presence of elongated inclusions and the higher banding index in that plane. The magnitudes of fracture initiation toughness and the resistance to crack propagation are lower at elevated temperatures in comparison to ambient temperature along both LC and CL planes. These properties are lowest at 250^{o}C along CL plane. To ensure safe operation of PHT piping made of SA 333 steel, the obtained lowest value of fracture toughness at 250^{o}C should be taken for LBB analysis.

One of the current design considerations in nuclear power plants is to safe-guard all of its structural components against seismic loading. The seismic fluctuations introduce cyclic loading having large magnitudes of compressive load in a component. A few reports available in the literature indicate that the cyclic fracture toughness of a material can be inferior to its monotonic fracture toughness properties. The nuclear regulatory commission suggests that in the LBB analysis of the PHT pipings, cyclic fracture toughness properties should be taken into consideration. But there is no information available in the literature about the cyclic fracture toughness behaviour of SA 333 steel to the best knowledge of the author. Thus it is very much relevant to understand the cyclic fracture behaviour of the selected steel for the safe operation life of the components. Some systematic cyclic *J-R* curve data have been generated during this investigation at various stress ratios and for various plastic displacement levels. The results of these investigations indicates that cyclic *J-R* curves of the selected steel remain almost invariant for the stress ratio $R \geq 0$. But the cyclic crack propagation resistance was found to decrease with decrease in stress ratio from 0 to negative magnitudes or with the decrease in the extent of plastic displacement. It has been demonstrated that higher crack extension during cyclic *J* test at $R < 0$ is due to re-sharpening of the crack tip. One of the important achievements in this investigation is

the understanding of the crack propagation mechanism in compressive cyclic loading. The mechanism of crack propagation is different in the case of cyclic than that in the monotonic *J* tests.

An attempt is made here to search for a co-relation between monotonic and cyclic fracture initiation toughness of the material in order to get an approximate estimate of the latter from the former. An empirical equation has been developed correlating cyclic and monotonic fracture initiation toughness. Such kind of correlation would be of considerable use when cyclic *J-R* curves are unknown.

The studies carried out have helped in understanding the monotonic fracture behaviour of the steel under different test conditions, but the primary heat transport system consists of several weld joints. The fracture resistance of the weld joints would not be the same as that obtained using virgin steel. So future investigation should be directed to understand fracture behaviour of the welded joints of SA 333 steels in the temperature range 0 to 300^{o}C. In addition it would be of great academic interest to know whether the DSA phenomenon remains prevalent in the weld joints.

In the present investigation cyclic fracture toughness studies on the steel has been carried out only at ambient temperature. Since the material is subjected to elevated temperatures in its service life, future work should be directed to understand the cyclic *J–R* curve behaviour of the material at elevated temperatures. Similar work should also be done on the weld joints of SA 333 steel. The empirical equation developed for correlating cyclic and monotonic fracture toughness is having only stress ratio as a variable parameter, but it has been observed that this property is influenced by the variation of plastic displacement. So further work is required to achieve refined version of such equations.

References

1 B.J. Brindley, Act. Metall., vol 18, p325, Mar. 1970,

2 J.D. Baird, and A. Jamieson, J. Iron and Steel Inst, vol 204, p793, 1966.

3 I. S. Kim and S. S. Kang, Int J. of Press Vess. and Piping, vol 62, p123, 1995.

4 J.W. Kim and I.S. Kim, Nuclear Eng. Design, vol 172, p49, 1997.

5. P.K. Singh, J. Chattopadhaya, H.S. Kushwaha, S. Tarafder and V.R. Ranganath Int. J of Pres. Ves & Piping, vol 75, p271 1998.

6. C. W. Marschall, M. P. Landow, G. M. Wilkowski and A. R. Rosenfield., Int. J.of Press. Vess and Piping, vol 62, p49, 1995.

7. S. T. Mahmood, K. M. Al-Otaibi, Y. H. Jung, and K. Linga Murty, J of Testing and Eval., vol 18, No.5, p 332 Sept.1990.

8. J.D. Landes and D.E.McCabe , Elastic-Plastic Fracture: Second Symposium, vol II-Fracture Resistance Curves and Engineering Applications, ASTM STP 803, C.F.Shih and J.P.Gudas Eds, American Society for Testing and Materials pII-723, 1983.

9. J.D. Landes and P.K. Liaw, Conf. Effect of Load and Thermal Histories on Mechanical Behaviour of Materials, Denver Colorado P.K.Liaw and T.Nicholas Eds p241, 1987.

10. Chang-Sung Seok and K.Linga Murthy, Int J. of Press Vess and Piping, vol 77, p303, 2000.

11. D.L.Rudland, E.Brust, and G.M.Wilkowski," The Effect of Cyclic and Dynamic Loading on the Fracture Resistance of Nuclear Piping Steels" Technical Report, Oct 1992-96. NUREG/CR-6440, BMI-2190, U.S. Nuclear Regulatry Commission, Dec 1996.

12 Irwin G.R., Trans ASME, J. Applied Mech., 24, p361, 1957

13 Wells, A. A. Unstable crack propagation in metals cleavage and fast fracture, Proc., Crack propagation Symposium Cranefield, p210, 1961.

14 Wells, A. A, British Welding Research Ass. Rep M13, 1963

15 Dugdale, D.S., J. Mech. of Phys. Solids, 8, p100, 1960.

16 Rice, J. R., J. Applied Mech. Trans ASME, 35, p379, June 1968.

17. Begley, J. A and Landes J. D., ASTM, STP 514, American Society for Testing and Materials, Philadelphia, p24, 1972.

18 E1820-99a Standard test method for Measurement of Fracture Toughness, Annual Book of ASTM Standards, Vol.03.01, p.1-34, ASTM, Philadelphia, PA, 2000,

19. Kraft, J.M., Sullivan, A.M. and Boyle, R.W., Proc. Crack Propagation Symp., Cranfield, 1, p8, 1961.

20. E-561-94, Standard Practice for R - Curve Determination , Annual Book of ASTM Standards 1994, vol 03.01, p489, ASTM, Philadelphia PA.

21. Paris, P.C. Tada, H., Zahoor, A. and Ernst, H., The Theory of Instability of the Tearing Mode of Elastic Plastic Crack Growth, ASTM STP 668, p5, 1970.

22. Hutchinson J.W. and Paris P.C., ASTM STP 668, p37, 1979.

23 BS 7448-1:1991, Fracture mechanics toughness tests. Method for determination of KIC critical CTOD and critical J values of metallic materials. 1991.

24. P.C. Paris and F. Erdogan, J of Basic Engineering p528, Sept 1963.

25 Miura, N ; Fujioka, T ; Kashima, K ; Kanno, S ; Hayashi, M ; Ishiwata, M ; Gotoh, N, "Low cycle fatigue and ductile fracture for Japanese carbon steel piping under dynamic loadings" NUCL. ENG. DES. Vol 153, No 1, 57-69 Dec. 1994.

26 G.A.Clarke, W.R. Andrews, P.C. Paris and D.W. Schmidt, Mechanics of Crack Growth ASTM STP 590, American Society for Testing of Materials, p22-42. 1976

27 J.A. Joyce," Development of a Criterion for the effect on the J-R curve of Elastic Unloadings," Fracture Mechanics: Eighteenth Symposium ASTM STP 945, D.T.Reed and R.D.Reed, Eds, American Society for Testing and Materials Philadelphia pp647-662. 1988

28 S. Kaiser ," On The Relation Between Stable Crack Growth and Fatigue," Fatigue of Engg. Matirials and Structures Vol 6, No1, pp33-49, 1983.

29 H. Kobayashi, T. Kusumoto and H. Nakazawa," The Cyclic J-R Curve and Upper Limit Characteristic of Fatigue-Crack Growth in 2.5Cr-1Mo Steel," Int. J.Press Vess and Piping vol 52 pp337-356 1992.

30 K. Mogami, K. Hayashi, K.Ando and N. Ogura," Elastic Plastic Fatigue Crack Growth and Tearing Instability behaviour under Cyclic Loads," Int. J.of Press. Vess and Piping, Vol 44, pp85-97 1990.

31 James A.Joyce," Characterization of the effects of Large Unloading Cycles on the Ductile Tearing Toughness of HSLA Steel," J of Testing and Evaluation, JTEVA, vol 18, No6, Nov 1990, pp 373-384.

32 James A. Joyce and Vuk Culafic," Characterization of Interaction Effects Between Ductile Tearing and Intense Fatigue Cycling," Int.J.Fract. Vol 36, pp89-100, 1988.

33 Chang-Sung Seok, Byoung-Gon Yoon and K.Linga Murty, " A Study on the Decrease Phenomenon of Fracture Resistance Value under Reversed Cyclic Loading" in Trans of the 15th Int. Conf on Structural Mechanics in Reactor Technology (SmiRT-15) Seoul Korea, Aug 15-20 1999 p V487-494. 1999.

34 N.E. Dowling and J.A. Begley ," Fatigue Crack Growth during Gross Plasticity and the J-Integral," Mechanics of Crack Growth, ASTM STP 590, American Society for Testing and Materials, pp 82-103. 1976

35 R.W.Hertzberge, Deformation and Fracture Mechanics of Engineering Materials, 3rd Edn, John Wiley and Sons, Singapore, 1989.

36 G. E. Dieter, "Mechanical Metallurgy" McGraw-Hill Book Company. P198. 1998.

37 Y.J Kim, et al, Nuclear Eng. Design vol.158, p241, 1995.

38 Blue Brittleness, In Metal Handbook, Desk Edition, ASM, Metals Park, Ohio, pp. 481, 1985,

39 P.Rodriguez, Bull. Mater. Sc. vol 6, No.4, p653, Sept 1984

40 J.W Kim and I.S. Kim, Nuclear Eng. Design vol.174, p59, 1997.

41. J. K. Chakaravartty, S. L. Wadekar, T. K. Sinha and M. K. Asundi, J. Nucl. Mater., vol 119, p51-58, 1983.

42. B.Mukherji, Nucl.Engg. and Design vol 111, p63-65, 1989.

43 K. G. Samuel, O. Gossman and H. Huthmann, Int. J. Press Vessel and Piping, vol 41 p59-74. 1990.

44. J. D. Atkinson, Z. J. Zhao and J. Yu in ASTM STP 1298, Effects of environment on the initiation of crack growth, ASTM WA, p199-215, 1997.

45 K. L. Murthy, J. Nucl. Mater., vol 270, p115-128, 1999.

46. A. A. Marengo and J. E. Perez Iprina, Nucl. Engg. and Design, vol 167, p215-222. 1996.

47. M. Srinivas, G. Malkondaiah P. Rama Rao and K. Linga Murthy, Scripta Metall. Mater, vol 25, p2585-2588, 1991.

48. M. Srinivas, G. Malkondaiah and P. Rama Rao, Acta Metall.Mater., vol 41, p1301-1312, 1993

49 C.S.Seok and K.L.Murthy, Int.J.Press Vessel and Piping, vol 76 p945-953. 1999.

50 S. S. Kang and I. S. Kim, Nucl. Technology, Vol 97, p336-343, 1992.

51 ASME Code Section II A Ferrous Material 1986 edition July 1, 1986.

52 A333/A333M-94, Standard Specification for Seamless and Weld Steel Pipe for Low-temperature Service. Vol 01.01, p193, 1999.

53 K. R. Narendrnath, H. Margolin, Y. H. Jung, P. S. Godavarti, Engg. Fracture Mech. Vol. 30, pp349-359, 1988.

54 Y. Asada, K. Takumi, N. Gotoh, T. Umemoto, K. Kashima, Int J. of Press Vess and Piping, Vol 43, p379-397, 1990

55 E 399-90, Test method for Plane-Strain Fracture Toughness of Metallic Materials, Annual Book of ASTM Standards, 1994, Vol.03.01, pp.407-437, ASTM, Philadelphia, PA

56 E562 Annual Book of ASTM Standards, Vol.03.01, p.1-34, ASTM, Philadelphia, PA, 1995

57 E 112-88, Test Methods for Determining Average Grain Size, Annual Book of ASTM Standards, 1994, Vol.03.01, pp.227-252, ASTM, Philadelphia, PA

58 E-1268-99 Standard Practice forAssessing the Degree of Banding or Orientation Microstructures Annual Book of ASTM Standards, Vol.03.01, p.1-29, ASTM, Philadelphia, PA, 2000,

59 E 8M-94a, Test Methods for Tension Testing of Metallic Materials (Metric), Annual Book of ASTM Standards, Vol.03.01, p.81-100, ASTM, Philadelphia, PA, 1994

60 E 23-94a, Test Methods for Notched Bar Impact Testing of Metallic Materials, Annual Book of ASTM Standards, 1994, Vol.03.01, pp.140-160, ASTM, Philadelphia, PA

61 E45 Standard Test Methods for Determining the Inclusion Content of Steel1 Annual Book of ASTM Standards, Vol.03.01, p.1-15, ASTM, Philadelphia, PA, 2000.

62 B. Russel Philos. Mag., vol 8, 615, 1963.

63 A.J.R.Solar-Gomez and W.J.McG.Tegart Philos.Mag. 20, 507, 1969.

64 L.J.Cuddy and W.C.Leslie, Acta Metall., 20, 1157, 1972.

65 E.Pink and A.Grinberg, Mater.Sci.Eng. 51, 1, 1981.

66 A.WijlerJ.Schade Van Westrum and A.Van den Beukel, Acta Metall. 20, 355, 1972

67 Metals Hand book, 9, 9th Edn ASM Metal Park, Ohio, 218, 1973.

68 S.A.Meguid, Engineering Fracture Mechanics, Elservier Applied Science, 1989.

69 J.T.Michalak, Metals Hand book, 8,ASM Metal Park, Ohio, 218, 1973.

70 A.F.Rowcliff, D.t.Hoelzer, S.J.Zinlde, ORNL Report- June 1999.

71 M.S.Wechsler, K.L.Murthy, Metall.Trans. A, 20A, No.12, p2637-2649, Dec. 1989.

72 J.D.Baird, The In homogeneities of Plastic Deformation, American Society for Metals, Metals Park, OH, 191, 1973.

73 G.F.Bolling and R.H.Richman, Acta Metall, No13, 709, 723, 745, 1965.

74 S.L.Mannan and P.Rodriguez, Philos. Mag. 25, 673, 1972.

75 S.L.Mannan K.G.Samuel and P.Rodriguez,Trans. Indian Inst. Metals, 36, 313,1983.

76 V.Seetharaman, Bull.Mater.Sci., 6, 1984.

77 B.K.Chaudhry, S.K.Ray, B.S.Rao, S.L.Mannan, Int.J. of Pressure Vess and Piping, 58, p 151, 1994.

78 P.G.McCormic Acta Metall.20, 351, 1972.

79 D.Broek, Elementry Engineering Fracture Mechanics, third ed., Martinus Nijh of Publishers, Netherlands,

80 E 647-93, Standard Test Method for Measurement of Fatigue Crack Growth Rates, Annual Book of ASTM Standards, 1994, Vol.03.01, pp.569-596, ASTM, Philadelphia, PA

81 E 813-89, Standard Test method for J_{IC}, A measure of Fracture Toughness, Annual Book of ASTM Standards, 1994, Vol.03.01, pp.732-746, ASTM, Philadelphia, PA.

82 S.J.Hudak, Jr and A.Saxena, Int. J. of Fracture, 14, pp453-468, Oct. 1978.

83 D.M.O'Brien and W.G.Fergusion, Int.J. of Fracture, 20, ppR39-43, 1082.

84 M.Srinivas, S.V.Kamat and P.Rama Rao, J. of testing and Evaluation. 22, No4, pp 302-308, July 1994.

85 J.Heevens, K-H.Scwalbe and A.Cornec, Fracture Mechanics: Eighteenth Symposium, ASTM STP 945, D.T.Read andR.P.Read eds American Society for Testing and Materials Phieladephia pp374-389, 1998.

86 V.R.Ranganath, Studies on Elastic-Plastic Fracture Criteria using J-integral and CTOD Methods, PhD Thesis, Indian Institute of Technology, Delhi 1987.

87 J.C.Newman,Jr., B.C.Booth and K.N.Shivakumar, Fracture Mechanics: Eighteenth Symposium, ASTM STP 945, D.T.Read and R.P.Reed, Eds, American Society for testing and Materials, Philadelphia, 1988, pp665-685.

88 C.W. Marschall and M.P.Landaw, Elastic – plastic fracture test methods : user's experience, vol 2, Pheladelphia PA: ASTM, STM 1114, p-238, 1991.

89 K.F.Amouzouvi and M.N.Bassim, Mat. Sc and Engg, 55, pp257-262, 1982.

90 Wei-Di Cao and Xiao-Ping Lu, Int.J of Fractur, 25, pp33-52, 1984

91 G.T.Hahn, A.R.Rosenfield, STP 432, ASTM, Philadelphia, 1968, p5.

92 R.O.Ritchie, J.F.Knott and J.R.Rice, J.Mech.Phys.Solids, 1973, vol 21, pp395-410.

93 D.A.Curry, Met.Sci., 1980, vol 14,p319.

94 R.O.Ritchie, W.L.Server and R.A.Wullaert, Metall, Trans., A, 1979, vol 10A, pp, 1557-70

95 R.O.Ritchie and A.W.Thompson, Met Trans A, vol 16A, 1985, 233-248

96 F.A.McClintock, J Applied Mech., Trans, ASTM Series E, 1968, 35, pp363-71.

97 S.Sivaprasad, S.Tarafder, V.R.Ranganath and K.K.Ray Mat.Sc. ang Engg., A284, 200, pp195-201

98 C.W. Marschall, and G.M. Wilkowski, .," Effect of Cyclic Loads on Ductile Fracture Resistance," ASME PVP vol 166,pp1-14, July 1989.

99 ESIS P2-92," ESIS Procedure for Determining the Fracture Behaviour of Materials", European Structural Integrity Society – ESIS, January 1992.

100 E 647-93, Standard Test Method for Measurement of Fatigue Crack Growth Rates, Annual Book of ASTM Standards, 1994, Vol.03.01, pp.569-596, ASTM, Philadelphia, PA

101 K.Ando and N.Ogura, J.Soc.Material Science, 27 767-72, 1978.